AD-A122 742 ACTA AERONAUTICA ET ASTRONAUTICA SINICA(U) FOREIGN TECHNOLOGY DIV WRIGHT-PATTERSON AFB OH S WANG ET AL. 14 OCT 82 FTD-ID(RS)T-1035-82 1/2

UNCLASSIFIED F/G 20/4 NL

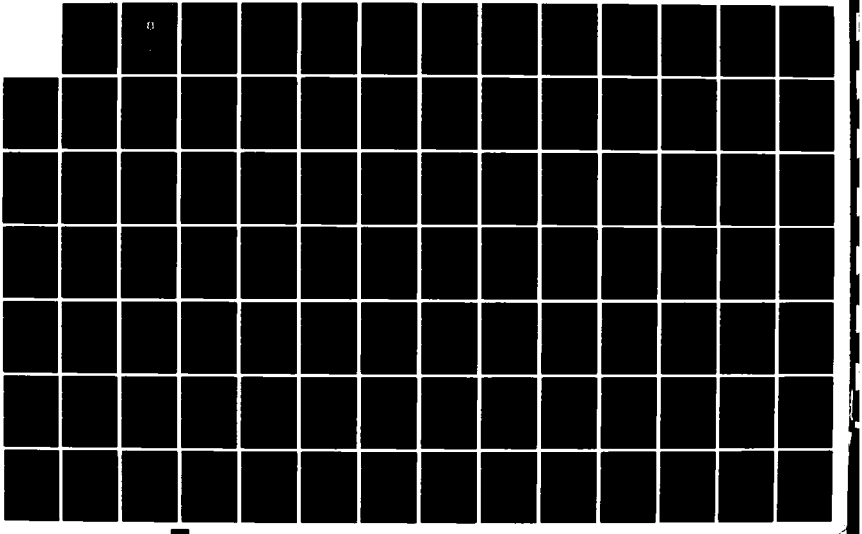

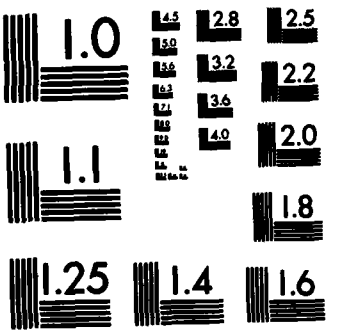

FTD-ID(RS)T-1035-82

AD A122742

# FOREIGN TECHNOLOGY DIVISION


ACTA AERONAUTICA ET ASTRONAUTICA SINICA

Vol. 3, Nr. 2, June 1982

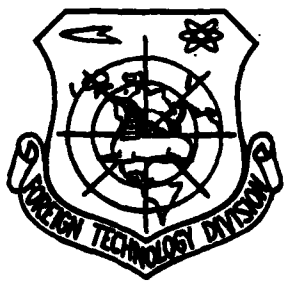




Approved for public release;
distribution unlimited.



82 12 28 142

# EDITED TRANSLATION

FTD-ID(RS)T-1035-82 14 October 1982

MICROFICHE NR: FTD-82-C-001324

ACTA AERONAUTICA ET ASTRONAUTICA SINICA

English pages: 152

Source: Hangkong Xuebao, Vol. 3, Nr. 2, June 1982, pp. 1-112

Country of origin: China
Translated by: SCITRAN
F33657-81-D-0263
Requester: FTD/TQTA




PREPARED BY:

TRANSLATION DIVISION
FOREIGN TECHNOLOGY DIVISION
WP-AFB, OHIO.

## GRAPHICS DISCLAIMER

All figures, graphics, tables, equations, etc. merged into this translation were extracted from the best quality copy available.

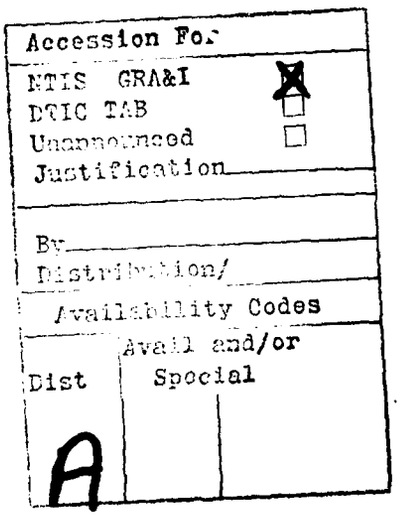


TABLE OF CONTENTS

ACTA AERONAUTICA Volume 3 No. 2 1982

CHINA AERONAUTICS SOCIETY *

# A simplified method for predicting rotor blade airloads

Wang Shicun and Xu Zhi (Nanjing Aeronautical Institute)

At present, a simplified method to predict the airloads of rotor blades is urgently needed for engineering applications. In this paper, on the basis of classical generalized vortex theory of the rotor, through the simplification process of the contribution of the circulations to the induced velocities, the second order distribution of the induced velocities of the rotor is obtained. Then, based on the blade element theory, a closed form of equations for circulation is established. By taking the flapping condition into account, simplified formulae for predicting rotor blade airloads are obtained. In particular, in the expressions of flapping coefficients, the variation of the induced velocity is taken into consideration by directly relating to blade parameters and flight parameters. Finally, the example given indicated that these equations are suitable for aerodynamic analysis and preliminary design of helicopters.

SYMBOLS

$\Omega$--rotor rotation velocity

R--rotor radius

$v$--induced velocity

$\bar{v}=v/\Omega R$--dimensionless $v$

$\Gamma$--circulation

$\bar{\Gamma}=\Gamma/\Omega R^2$--dimensionless $\Gamma$

$(r, \psi)$ or $(\rho, \theta)$--polar coordinate on the plane of the rotor blade

$\bar{r} = r/R$--dimensionless r

$\bar{\rho} = \rho/R$--dimensionless $\rho$

$\rho_H$--density of air

k--number of blade

* This paper was presented at the 7th European Rotor Flight Vehicle and Power Lift Flight Vehicle Conference in September 1981. Recd. Nov. 1981.

$V_o$--forward velocity of the rotor

$\bar{V}_o = V_o/\Omega R$--dimensionless $V_o$

$V_1$--combined air flow velocity, a constant with respect to the blade plane

$\bar{V}_1 = V_1/\Omega R$--dimensionless $V_1$

$\alpha_o$--attack angle of rotor with respect to $V_o$

$\alpha_1$--attack angle of rotor with respect to $V_1$

b-- arc length of the blade

$\bar{b} = b/R$--dimensionless b

$c_y$--lift coefficient in the cross-section of the blade

$a_\infty$--slope of two dimensional lift curve

$T_1$--pulling force of a blade

$T = kT_1$--pulling force of the rotor

$\vartheta_s$--installation angle of the blade cross section

$\vartheta_r$--installation angle of the cross section of the blade root

$\Delta\vartheta$--twist of the blade

$\vartheta_1$--cosine term of the periodic variation of blade displacement

$\vartheta_2$--sine term of the periodic variation of blade displacement

U--relative flow velocity of the blade cross section

$\bar{U} = U/\Omega R$--dimensionless U

$U_x$--velocity component of U in the plane of blades

$U_y$--velocity component of U in the direction perpendicular to the blades

$\mu = V_o \cos\alpha_o/\Omega R$--advance ratio

$\lambda_o = V_o \sin\alpha_o/\Omega R$--flowing-in ratio

K--flapping adjustment coefficient

$\beta_e$--flapping angle with respect to the horizontal hinge

$\beta$--flapping angle with respect to the rotation center

$a_o$--coning angle

$a_n$--cosine term of blade flapping

$b_n$--sine term of blade flapping

e--outward displacement of the horizontal hinge

$\bar{e} = e/R$--dimensionless e

$m_1$--mass of the blade

$\bar{m}_1 = m_1/\rho_H R^3$--dimensionless $m_1$

$C_T = T/\frac{1}{2}\rho_H \pi R^2 \Omega^2 R^2$--coefficient of pulling force

$J_e$--moment of inertia of a blade around the horizontal hinge

$S_e$--moment of mass of a blade around the horizontal hinge

$(M_A)_e$--torque of pulling force of a blade around the horizontal hinge

$(M_G)_e$--gravity torque of blade pulling force around horizontal hinge

g--gravitational acceleration

x--integrated loss coefficient of the root and the tip of the blades

## I. INTRODUCTION

The estimation of airloads of rotor blades in the flapping plane is one of the basic topics in the aerodynamics and helicopter aerodynamics. This is because: the flight quality, pilot control quality of the helicopter and the fatigue life of the rotor and the destabilization of the aerodynamic elasticity are entirely determined by the airloads of the rotor. It is particularly important with regard to its strain load.

Since the 1960's, scholars in all the countries have made significant progress in this area through hard work. AGARD held a meeting on "Methods for Estimation of Helicopter Rotor Loads" in Italy in 1973 [1] and demonstrated the various analytical methods adopted by various manufacturers. However, just as what is described in some comments and papers published later [2,3], due to the complexity of the working condition of the rotor, even with a high speed large scale numerical computer, no significant progress has been made in recent years. Therefore, it is more attractive to develop a simplified method to estimate rotor airloads for use by design engineers.

This paper began with the generalized vortex theory of the rotor to obtain the relations between first two orders of harmonic wave of the induced velocity and the lower and same order harmonic of the circulations. Then, based on the blade element theory, a closed form equation for circulations are established. Finally, by taking flapping

conditions into account, the simplified equation for the estimation of the airload of the rotor is derived.

## II. INDUCED VELOCITIES

Based on the generalized vortex theory of rotor with fixed vortex [4], the induced velocity at any point on the plane of the blades $(\bar{r}, \psi)$ is a function of the adhered circulation $\bar{\Gamma}$ $(\bar{\rho}, \theta)$:

$$\bar{v} = \bar{v}(\bar{\Gamma}) \tag{2-1}$$

If the circulation $\bar{\Gamma}$ is expanded into a Fourier series:

$$\bar{\Gamma} = \bar{\Gamma}_0(\bar{\rho}) + \sum_{m=1} [\bar{\Gamma}_{mc}(\bar{\rho})\cos m\theta + \bar{\Gamma}_{ms}(\bar{\rho})\sin m\theta] \tag{2-2}$$

Then, the induced velocities $\bar{v}$ can also be written as a Fourier series:

$$\bar{v} = \bar{v}_0(\bar{r}) + \sum_{n=1} [\bar{v}_{nc}(\bar{r})\cos n\psi + \bar{v}_{ns}(\bar{r})\sin n\psi] \tag{2-3}$$

Here the different harmonic wave components of the induced velocity in general are caused by the various orders of harmonic components of the circulations. In this paper, for simplification, only the major contributing lower order and same order terms of the circulations are considered with regard to induced velocities, i.e.

$$\left.\begin{aligned}
\bar{v}_0 &= \bar{v}_0^0 \\
\bar{v}_{1c} &= \bar{v}_{1c}^0 + \bar{v}_{1c}^{1c} \\
\bar{v}_{1s} &= \bar{v}_{1s}^0 + \bar{v}_{1s}^{1s} \\
\bar{v}_{2c} &= \bar{v}_{2c}^0 + \bar{v}_{2c}^{1c} + \bar{v}_{2c}^{1s} + \bar{v}_{2c}^{2c} \\
\bar{v}_{2s} &= \bar{v}_{2s}^0 + \bar{v}_{2s}^{1c} + \bar{v}_{2s}^{1s} + \bar{v}_{2s}^{2s} \\
&\cdots\cdots\cdots\cdots\cdots\cdots
\end{aligned}\right\} \tag{2-4}$$

where the superscripts represent the order of harmonic of the circulations.

According to Wang Shicun's vortex theory 1 by limiting to second order harmonics, we get (the downward induced velocity is positive) [5]:

$$\bar{v}_0 = -\frac{k}{4\pi\bar{V}_1}(-\bar{\Gamma}_0)$$

$$\bar{v}_{1c} = -\frac{k}{4\pi\bar{V}_1}\left\{(c+c)\left[\int_0^{\bar{r}} \frac{d\bar{\Gamma}_0}{d\bar{\rho}} \frac{\bar{\rho}^2}{\bar{r}^2} \frac{1}{2} F\left(\frac{3}{2}, \frac{1}{2}, 2, \frac{\bar{\rho}^2}{\bar{r}^2}\right) d\bar{\rho} + \int_{\bar{r}}^1 \frac{d\bar{\Gamma}_0}{d\bar{\rho}} \frac{\bar{r}}{\bar{\rho}} \frac{1}{2} F\left(\frac{3}{2}, \frac{1}{2}, 2, \frac{\bar{r}^2}{\bar{\rho}^2}\right) d\bar{\rho}\right] + (1-c^2)(-\bar{\Gamma}_{1c})\right\}$$

$$\bar{v}_{1s} = -\frac{k}{4\pi\bar{V}_1}\left\{(c+c)\left(\frac{-\bar{V}_1}{\bar{r}}\right)\bar{\Gamma}_0 + (1+c^2)(-\bar{\Gamma}_{1s})\right\}$$

$$\bar{v}_{2c} = -\frac{k}{4\pi\bar{V}_1}\left\{(c^2+c^2)\int_0^{\bar{r}} \frac{d\bar{\Gamma}_0}{d\bar{\rho}} \frac{\bar{\rho}^2}{\bar{r}^2} d\bar{\rho} + (c^2-c) \times \left[\int_0^{\bar{r}} -\frac{d\bar{\Gamma}_{1c}}{d\bar{\rho}} \frac{\bar{\rho}^2}{\bar{r}^2} \frac{1}{2} F\left(\frac{3}{2}, \frac{1}{2}, 2, \frac{\bar{\rho}^2}{\bar{r}^2}\right) d\bar{\rho} - \int_{\bar{r}}^1 \frac{d\bar{\Gamma}_{1c}}{d\bar{\rho}} \frac{1}{2} F\left(\frac{3}{2}, \frac{1}{2}, 2, \frac{\bar{r}^2}{\bar{\rho}^2}\right) d\bar{\rho}\right] + (c^3+c)\left(\frac{\bar{V}_1}{\bar{r}}\right)\int_0^{\bar{r}} \frac{d\bar{\Gamma}_{1s}}{d\bar{\rho}} \frac{\bar{\rho}}{\bar{r}} d\bar{\rho} + (1+c^4)(-\bar{\Gamma}_{2c})\right\}$$

$$\bar{v}_{2s} = -\frac{k}{4\pi\bar{V}_1}\left\{(c^2+c^2)\left(-\frac{\bar{V}_1}{\bar{r}}\right)\left[\int_0^{\bar{r}} \frac{d\bar{\Gamma}_0}{d\bar{\rho}} F\left(\frac{3}{2}, -\frac{1}{2}, 1, \frac{\bar{\rho}^2}{\bar{r}^2}\right) d\bar{\rho} - \int_{\bar{r}}^1 \frac{d\bar{\Gamma}_0}{d\bar{\rho}} \frac{\bar{r}^3}{\bar{\rho}^3} \frac{1}{8} F\left(\frac{3}{2}, \frac{3}{2}, 3, \frac{\bar{r}^2}{\bar{\rho}^2}\right) d\bar{\rho}\right] + (c^3-c)\left(\frac{\bar{V}_1}{\bar{r}}\right)\int_0^{\bar{r}} \frac{d\bar{\Gamma}_{1c}}{d\bar{\rho}} \frac{\bar{\rho}}{\bar{r}} d\bar{\rho} + (c^3+c)\left[\int_0^{\bar{r}} \frac{d\bar{\Gamma}_{1c}}{d\bar{\rho}} \frac{\bar{\rho}^2}{\bar{r}^3} \frac{1}{2} F\left(\frac{3}{2}, \frac{1}{2}, 2, \frac{\bar{\rho}^2}{\bar{r}^2}\right) d\bar{\rho} + \int_{\bar{r}}^1 \frac{d\bar{\Gamma}_{1c}}{d\bar{\rho}} \frac{1}{2} F\left(\frac{3}{2}, -\frac{1}{2}, 2, \frac{\bar{r}^2}{\bar{\rho}^2}\right) d\bar{\rho}\right] + (1-c^4)(-\bar{\Gamma}_{2s})\right\} \qquad (2\text{-}5)$$

where the super-geometric function is defined as:

$$F(a, b, d, z) = 1 + \sum_{k=1} \frac{(a)_k (b)_k}{(d)_k k!} z^k$$

where $|z| < 1$

$$(a)_k = a(a+1)(a+2)\cdots(a+k-1)$$

$$d \neq -1, -2, \cdots$$

and the symbol c is

$$c = \frac{1-|\sin\alpha_1|}{\cos\alpha_1} = \frac{\cos\alpha_1}{1+|\sin\alpha_1|} < 1$$

The above expressions for the harmonic components of the induced velocities are the key to the solution in this paper. The super-geometric function used, based on [8], can take only the first few terms.

## III. CIRCULATION EQUATION

Based on the blade element theory and the famous Zukovski equation, the airload of the rotor blade can be expressed as [6]:

$$\frac{dT_1}{dr}=\rho_H U\Gamma=\frac{1}{2}\rho_H U^2 bc_y \qquad (3\text{-}1)$$

Here we adopted the regular assumption that:

$$U\approx U_e$$

$$c_y\approx a_\infty\left(\vartheta_e-\frac{U_z}{U_e}\right)$$

Therefore, the circulation equation (dimensionless) is:

$$\bar{\Gamma}=\frac{1}{2}a_\infty\bar{b}(\bar{U}_e\vartheta_e-\bar{U}_y) \qquad (3\text{-}2)$$

For hinge type rotors, we assumed that the blades are rigid, its flapping adjustment coefficient is K and the outward displacement is e. For hingeless rotors, it can be assumed that the blades are elastic and it is treated as equivalent quantities. Thus

$$\vartheta_e=\vartheta_0+\bar{r}\Delta\vartheta+\vartheta_1\cos\psi+\vartheta_2\sin\psi-K\beta_e$$

$$\bar{U}_e=\bar{r}+\mu\sin\psi$$

$$U_y=-\lambda_0+\bar{v}+\mu\cos\psi\cdot\beta_e+(\bar{r}-\bar{e})\frac{d\beta_e}{d\psi} \qquad (3\text{-}3)$$

and

$$\beta_e=\frac{\beta}{1-\bar{e}}=\frac{1}{1-\bar{e}}\left[a_0-\sum_{n=1}(a_n\cos n\psi+b_n\sin n\psi)\right] \qquad (3\text{-}4)$$

If the following quantities are introduced:

$$\left.\begin{aligned}
&\lambda_0^*=\lambda_0+\vartheta_2^*\mu && b_1^*=b_1+\vartheta_1^*\\
&a_1^*=a_1-\vartheta_2^* && \\
&\vartheta_0^*=\vartheta_0-K\frac{a_0}{1-\bar{e}} && \\
&\vartheta_1^*=\vartheta_1+K\frac{a_1}{1-\bar{e}} && \vartheta_2^*=\vartheta_2+K\frac{b_1}{1-\bar{e}}
\end{aligned}\right\} \qquad (3\text{-}5)$$

and neglect the smaller terms containing $\frac{\bar{e}}{1-\bar{e}}$ and higher than second order flapping coefficients, such as $a_3$, $b_3\ldots$, we get

$$\left.\begin{aligned}
\bar{\Gamma}_0&=\frac{1}{2}a_\infty\bar{b}\left[\vartheta_0^*\bar{r}+\Delta\vartheta\bar{r}^2-\bar{v}_0+\lambda_0^*+\frac{1}{2}\mu a_1^*\right]\\
\bar{\Gamma}_{1c}&=\frac{1}{2}a_\infty\bar{b}\left[-\bar{v}_{1c}-\mu a_0+b_1^*\bar{r}+\frac{1}{2}\mu a_2+\frac{1}{2}\mu Kb_2\right]\\
\bar{\Gamma}_{1s}&=\frac{1}{2}a_\infty\bar{b}\left[\vartheta_0^*\mu+\Delta\vartheta\mu\bar{r}-\bar{v}_{1s}-a_1^*\bar{r}-\frac{1}{2}\mu Ka_2+\frac{1}{2}\mu b_2\right]\\
\bar{\Gamma}_{2c}&=\frac{1}{2}a_\infty\bar{b}\left[-\bar{v}_{2c}+\frac{1}{2}\mu a_1^*+Ka_2\bar{r}+2b_2\bar{r}\right]\\
\bar{\Gamma}_{2s}&=\frac{1}{2}a_\infty\bar{b}\left[-\bar{v}_{2s}+\frac{1}{2}\mu b_1^*-2a_2\bar{r}+Kb_2\bar{r}\right]
\end{aligned}\right\} \qquad (3\text{-}6)$$

It is worthwhile noting that under the simplified method described above (that is, only considering the induced velocities caused by lower order and same order terms of circulations), the derived relation between induced velocities and circulation has a closed form.

By solving (2-5) and (3-6) simultaneously, the various orders of harmonics of the induced velocity can be obtained:

$$\bar{v}_0 = \frac{A_0^0}{1+A_0^0}\left[\vartheta_0^*\bar{r} + \Delta\vartheta\bar{r}^2 + \lambda_0^* + \frac{1}{2}\mu a_1^*\right]$$

$$\bar{v}_{1c} = \frac{A_{1c}^{1c}}{1+A_{1c}^{1c}}\left[-\mu a_0 + b_1^*\bar{r} + \frac{1}{2}\mu a_2 + \frac{1}{2}\mu K b_2\right] + \frac{1}{1+A_{1c}^{1c}}\Delta\bar{v}_{1c}$$

$$\Delta\bar{v}_{1c} = \frac{A_{1c}^0}{1+A_0^0}\left[\left(\lambda_0^* + \frac{1}{2}\mu a_1^*\right)\left(\frac{1}{2}\bar{r} + \frac{1}{3}\bar{r}^3\right) + \vartheta_0^*\left(-\frac{8}{9}\bar{r} + \frac{10}{7}\bar{r}^2 + \frac{1}{10}\bar{r}^3\right)\right.$$
$$\left. + \Delta\vartheta\left(-\frac{1}{2}\bar{r} - \frac{1}{7}\bar{r}^2 + \frac{8}{7}\bar{r}^3\right)\right]$$

$$\bar{v}_{1s} = \frac{A_{1s}^{1s}}{1+A_{1s}^{1s}}\left[\vartheta_0^*\mu + \Delta\vartheta\mu\bar{r} - a_1^*\bar{r} - \frac{1}{2}\mu K a_2 + \frac{1}{2}\mu b_2\right] + \frac{1}{1+A_{1s}^{1s}}\Delta v_{1s}$$

$$\Delta\bar{v}_{1s} = \frac{A_{1s}^0}{1+A_{1s}^{1s}}\bar{V}_1\left[\vartheta_0^* + \Delta\vartheta\bar{r} + \frac{1}{\bar{r}}\left(\lambda_0^* + \frac{1}{2}\mu a_1^*\right)\right]$$

$$\bar{v}_{2c} = \frac{A_{2c}^{2c}}{1+A_{2c}^{2c}}\left[\frac{1}{2}\mu a_1^* + K a_2\bar{r} + 2b_2\bar{r}\right] + \frac{1}{1+A_{2c}^{2c}}\Delta\bar{v}_{2c}$$

$$\Delta\bar{v}_{2c} = \frac{A_{2c}^0}{1+A_0^0}\left[-\frac{1}{3}\vartheta_0^*\bar{r} - \frac{1}{2}\Delta\vartheta\bar{r}^2\right] + \frac{A_{2c}^{1c}}{1+A_{2c}^{2c}}\left\{\frac{A_{1c}^0}{1+A_0^0}\left[\left(\lambda_0^* + \frac{1}{2}\mu a_1^*\right)\right.\right.$$
$$\times\left(-\frac{1}{15}\bar{r} - \frac{1}{10}\bar{r}^3 - \frac{7}{20}\bar{r}^5\right) + \vartheta_0^*\left(\frac{3}{10}\bar{r} - \frac{2}{9}\bar{r}^3 - \frac{1}{3}\bar{r}^5\right)$$
$$\left.\left. + \Delta\vartheta\left(\frac{2}{15}\bar{r} + \frac{16}{39}\bar{r}^3 - \frac{11}{16}\bar{r}^5\right)\right] + \mu a_2\left(-\frac{1}{2} - \frac{1}{3}\bar{r}^2\right)\right. \qquad (3\text{-}7)$$
$$\left. + b_1^*\left(\frac{1}{16}\bar{r} + \frac{3}{8}\bar{r}^2 + \frac{1}{4}\bar{r}^4\right)\right\} + \frac{A_{2c}^{1s}}{1+A_{1s}^{1s}}\bar{V}_1\left[-\frac{1}{2}\left(1 - \frac{A_{1s}^0/\cos\alpha_1}{1+A_0^0}\right)\mu\Delta\vartheta\right.$$
$$\left. + \frac{1}{2}a_1^* - \frac{A_{1s}^0/\cos\alpha_1}{1+A_0^0}\mu\left(\lambda_0^* + \frac{1}{2}\mu a_1^*\right)\frac{1}{\bar{r}^2}(1+\ln\bar{r})\right]$$

$$\bar{v}_{2s} = \frac{A_{2s}^{2s}}{1+A_{2s}^{2s}}\left[\frac{1}{2}\mu b_1^* - 2a_2\bar{r} + K b_2\bar{r}\right] + \frac{1}{1+A_{2s}^{2s}}\Delta\bar{v}_{2s}$$

$$\Delta\bar{v}_{2s} = \frac{A_{2s}^0}{1+A_0^0}\bar{V}_1\left[\left(\lambda_0^* + \frac{1}{2}\mu a_1^*\right)\left(\frac{1}{\bar{r}} + \frac{1}{8}\bar{r}^2 + \frac{1}{5}\bar{r}^4\right)\right.$$
$$\left. + \vartheta_0^*\left(\frac{4}{7} + \frac{5}{32}\bar{r}^2 + \frac{2}{7}\bar{r}^4\right) + \Delta\vartheta\left(\frac{1}{8}\bar{r} + \frac{3}{8}\bar{r}^2 + \frac{1}{3}\bar{r}^4\right)\right]$$
$$+ \frac{A_{2s}^{1c}}{1+A_{1c}^{1c}}\bar{V}_1\left\{\frac{A_{1c}^0}{1+A_0^0}\left[\left(\lambda_0^* + \frac{1}{2}\mu a_1^*\right)\left(-\frac{1}{4} - \frac{1}{9}\bar{r}^2 - \frac{1}{5}\bar{r}^4\right)\right.\right.$$
$$\left.\left. + \vartheta_0^*\left(-\frac{4}{21} - \frac{2}{9}\bar{r}^2 - \frac{9}{50}\bar{r}^4 - \frac{1}{4}\ln\bar{r}\right)\right.\right.$$

$$+\Delta\vartheta\left(\frac{1}{4}-\frac{1}{10}\bar{r}-\frac{2}{5}\bar{r}^2-\frac{2}{7}\bar{r}^4\right)\Big]+\frac{1}{2}b_1^*\Big\}$$
$$+\frac{A_{2s}^{1s}}{1+A_{1s}^{1s}}\Big[\left(\lambda_0^*+\frac{1}{2}\mu a_1^*\right)\frac{A_{1s}^0/\cos\alpha_1}{1+A_0^0}\mu\left(-\frac{37}{40}\cdot\frac{1}{\bar{r}}-\frac{1}{15}\bar{r}^2-\frac{3}{10}\bar{r}^4\right)$$
$$+\vartheta_0^*\left(1-\frac{A_{1s}^0/\cos\alpha_1}{1+A_0^0}\right)\mu\left(\frac{1}{2}+\frac{1}{3}\bar{r}^2\right)$$
$$+\Delta\vartheta\left(1-\frac{A_{1s}^0/\cos\alpha_1}{1+A_0^0}\right)\mu\left(\frac{1}{16}\bar{r}+\frac{3}{8}\bar{r}^2+\frac{1}{4}\bar{r}^4\right)$$
$$+a_1^*\left(-\frac{1}{16}\bar{r}-\frac{3}{8}\bar{r}^2-\frac{1}{4}\bar{r}^4\right)\Big] \qquad (3\text{-}7)$$

where $A_0^0$, $A_{1s}^0$, $A_{1c}^{1c}$ ...are defined as follows:

$$A_0^0=\frac{a_\infty\bar{b}}{2}\cdot\frac{k}{4\pi\bar{V}_1}$$

$$A_{1c}^{1c}=A_0^0\frac{2\sin\alpha_1}{1+\sin\alpha_1} \qquad A_{1s}^{1s}=A_0^0\frac{2}{1+\sin\alpha_1}$$

$$A_{2c}^{2c}=A_0^0\frac{2+2\sin^2\alpha_1}{(1+\sin\alpha_1)^2} \qquad A_{2s}^{2s}=A_0^0\frac{4\sin\alpha_1}{(1+\sin\alpha_1)^2}$$

$$A_{1s}^0=A_0^0\frac{2\cos\alpha_1}{1+\sin\alpha_1} \qquad A_{1s}^0=A_{1s}^0$$

$$A_{2s}^0=A_0^0\frac{2-2\sin\alpha_1}{1+\sin\alpha_1} \qquad A_{2s}^0=A_{2s}^0$$

$$A_{2c}^{1c}=A_0^0\frac{2\cos\alpha_1\sin\alpha_1}{(1+\sin\alpha_1)^2} \qquad A_{2s}^{1c}=A_{2c}^{1c}$$

$$A_{2c}^{1s}=A_0^0\frac{2\cos\alpha_1}{(1+\sin\alpha_1)^2} \qquad A_{2s}^{1s}=A_{2c}^{1s}$$

We must explain here that in the deviation of induced velocity by integration, if infinity appears, then it is necessary to replace the lower limit by $\bar{r}_o$ instead of 0. $\bar{r}_o$ is the relative radius of the blade root at which the wing cross section begins to show.

Since the circulation $\bar{\Gamma}$ can be expanded into a Fourier series, the airloads can also be written in the form of a Fourier series:

$$\frac{dC_{T1}}{d\bar{r}}=\frac{2}{\pi}\bar{U}\bar{\Gamma}=\left(\frac{dC_{T1}}{d\bar{r}}\right)_0+\sum_{m=1}\left[\left(\frac{dC_{T1}}{d\bar{r}}\right)_{mc}\cos m\psi+\left(\frac{dC_{T1}}{d\bar{r}}\right)_{ms}\sin m\psi\right] \qquad (3\text{-}8)$$

From equations (2-2), (3-1) and (3-3), we get

$$\left(\frac{dC_{T1}}{d\bar{r}}\right)_0 = \frac{2}{\pi}\left(\bar{\Gamma}_0\bar{r} + \frac{1}{2}\mu\bar{\Gamma}_{1s}\right)$$
$$\left(\frac{dC_{T1}}{d\bar{r}}\right)_{1c} = \frac{2}{\pi}\left(\bar{\Gamma}_{1c}\bar{r} + \frac{1}{2}\mu\bar{\Gamma}_{2s}\right)$$
$$\left(\frac{dC_{T1}}{d\bar{r}}\right)_{1s} = \frac{2}{\pi}\left(\bar{\Gamma}_{1s}\bar{r} + \mu\bar{\Gamma}_0 - \frac{1}{2}\mu\bar{\Gamma}_{2c}\right)$$
$$\left(\frac{dC_{T1}}{d\bar{r}}\right)_{2c} = \frac{2}{\pi}\left(\bar{\Gamma}_{2c}\bar{r} - \frac{1}{2}\mu\bar{\Gamma}_{1s} + \frac{1}{2}\mu\bar{\Gamma}_{3s}\right)$$
$$\left(\frac{dC_{T1}}{d\bar{r}}\right)_{2s} = \frac{2}{\pi}\left(\bar{\Gamma}_{2s}\bar{r} + \frac{1}{2}\mu\bar{\Gamma}_{1c} - \frac{1}{2}\mu\bar{\Gamma}_{3c}\right) \qquad (3\text{-}9)$$

Therefore, the relations between the various harmonics of the airload of the blade and the various harmonics of the circulation are established.

As for the strain coefficient of the entire rotor, it is easy to find out:

$$C_T = k\int_{\bar{r}_0}^{\bar{r}_1}\left(\frac{dC_{T1}}{d\bar{r}}\right)_0 d\bar{r} = \chi k\int_0^1\left(\frac{dC_{T1}}{d\bar{r}}\right)_0 d\bar{r} \qquad (3\text{-}10)$$

where $\bar{r}_0$ is the relative radius of the blade root at which the wing cross section begins to take shape; $\bar{r}_1$ is the loss factor of the blade tip if it is necessary to be considered.

## IV. FLAPPING CONDITION

Because flapping coefficients are included in the expressions of circulations and induced velocities, it is necessary to study the flapping motion.

For hinge type rotors, according to [6], the flapping motion of the blades is described by the following equation:

$$\frac{d^2\beta_0}{dt^2}J_0 + \beta_0\Omega^2(J_0 + eS_0) = (M_A)_0 - (M_G)_0 \qquad (4\text{-}1)$$

where

$J_0 = \int_e^R (r-e)^2 dm_1$ moment of inertia of a single blade around the horizontal hinge

$S_0 = \int_e^R (r-e)dm_1$ moment of mass of a single blade around the horizontal hinge

$(M_A)_e = \int_{r_0}^{r_1} (r - e)\,dT_1$ strain torque of a single blade around the horizontal hinge

$(M_G)_e = gS_e$ gravity torque of a single blade around the horizontal hinge

Written in a dimensionless form:

$$\frac{d^2\beta_e}{d\psi^2}\bar{J}_e + \beta_e \bar{v}^2 \bar{J}_e = (\bar{M}_A)_e - (M_G)_e$$

It can be further written as

$$\frac{d^2\beta}{d\psi^2}\bar{J} + \beta\bar{v}^2\bar{J} = \bar{M}_A - \bar{M}_G \qquad (4\text{-}2)$$

where

$$\bar{J}_e = J_e/m_1R^2 \qquad \bar{J} = \bar{J}_e/(1-\bar{e})^2$$

$$\bar{v}^2 = 1 + \frac{\bar{e}\bar{S}_e}{\bar{J}_e} = 1 + \frac{\bar{e}\bar{S}}{(1-\bar{e})\bar{J}}$$

$$\bar{S}_e = S_e/m_1R \qquad \bar{S} = \bar{S}_e/(1-\bar{e})$$

$$(\bar{M}_A)_e = (M_A)_e/m_1\Omega^2R^2 \qquad \bar{M}_A = (\bar{M}_A)_e/(1-\bar{e})$$

$$(\bar{M}_G)_e = (M_G)_e/m_1\Omega^2R^2 \qquad \bar{M}_G = \bar{g}\bar{S}$$

$$\bar{g} = g/\Omega^2R$$

If we expand $\bar{M}_A$ into a Fourier series

$$\bar{M}_A = (\bar{M}_A)_0 + \sum_{n=1}^{\infty}[(\bar{M}_A)_{ne}\cos n\psi + (\bar{M}_A)_{no}\sin n\psi] \qquad (4\text{-}3)$$

then we get:

$$\begin{aligned} a_0\bar{v}^2\bar{J} &= (\bar{M}_A)_0 - \bar{g}\bar{S} \\ &\cdots\cdots\cdots\cdots \\ a_n(n^2-\bar{v}^2)\bar{J} &= (\bar{M}_A)_{ne} \\ b_n(n^2-\bar{v}^2)\bar{J} &= (\bar{M}_A)_{no} \end{aligned} \qquad (4\text{-}4)$$

and

$$\begin{aligned} (\bar{M}_A)_0 &= \frac{\rho_H R^3}{m_1}\int_{\bar{r}_0}^{\bar{r}_1} \frac{\bar{r}-\bar{e}}{1-\bar{e}}\,\frac{\pi}{2}\left(\frac{dC_{T_1}}{d\bar{r}}\right)_0 d\bar{r} \\ &\cdots\cdots\cdots \\ (\bar{M}_A)_{ne} &= \frac{\rho_H R^3}{m_1}\int_{\bar{r}_0}^{\bar{r}_1} \frac{\bar{r}-\bar{e}}{1-\bar{e}}\,\frac{\pi}{2}\left(\frac{dC_{T_1}}{d\bar{r}}\right)_{ne} d\bar{r} \\ (\bar{M}_A)_{no} &= \frac{\rho_H R^3}{m_1}\int_{\bar{r}_0}^{\bar{r}_1} \frac{\bar{r}-\bar{e}}{1-\bar{e}}\,\frac{\pi}{2}\left(\frac{dC_{T_1}}{d\bar{r}}\right)_{no} d\bar{r} \end{aligned} \qquad (4\text{-}5)$$

Therefore, in order to calculate the flapping coefficients $a_0 \ldots a_n$, $b_n$, we must first solve $(\bar{M}_A)_o$---, $(\bar{M}_A)_{no}$, $(\bar{M}_A)_{nso}$. These are tedious integrations. In a simplified situation, let us assume $\bar{b}$ is a constant, $\bar{e} = 0$, $\bar{v}^2 = 1$ and note

$$\gamma = \frac{\rho_H R^3}{m_1} \frac{a_\infty \bar{b}}{2} \Big/ \bar{J}$$

we get

$$\begin{aligned}
a_0 &= \chi\gamma\left[\vartheta_0^*\left(\frac{1}{4}+\frac{1}{4}\mu^2\right)+\Delta\vartheta\left(\frac{1}{5}+\frac{1}{6}\mu^2\right)+\frac{1}{3}\lambda_0^*\right. \\
&\quad \left.-\int_0^1 \bar{v}_0\bar{r}^2 d\bar{r}-\int_0^1 \frac{1}{2}\mu\bar{v}_{1s}\bar{r}\,d\bar{r}\right]-\frac{\bar{g}\bar{S}}{\bar{J}} \\
a_1^* &= \left[\frac{2}{3}\vartheta_0^*\mu+\frac{1}{2}\Delta\vartheta\mu+\frac{1}{2}\lambda_0^*\mu-\int_0^1 \bar{v}_{1c}\bar{r}^2 d\bar{r}-\int_0^1 \mu\bar{v}_0\bar{r}\,d\bar{r}\right. \\
&\quad \left.+\int_0^1 \frac{1}{2}\mu\bar{v}_{2c}\bar{r}\,d\bar{r}\right]\Big/\left(\frac{1}{4}-\frac{1}{8}\mu^2\right) \\
b_1^* &= \left[\int_0^1 \bar{v}_{1s}\bar{r}^2 d\bar{r}+\int_0^1 \frac{1}{2}\mu\bar{v}_{2s}\bar{r}\,d\bar{r}+\frac{1}{3}a_0\mu\right]\Big/\left(\frac{1}{4}+\frac{1}{8}\mu^2\right) \\
a_2 &= (q_1 p_1 + q_2 p_2)/(q_1^2+q_2^2) \\
b_2 &= (q_1 p_2 - q_2 p_1)/(q_1^2+q_2^2)
\end{aligned} \tag{4-6}$$

where

$$\begin{aligned}
p_1 &= -\frac{1}{4}\vartheta_0^*\mu^2-\frac{1}{6}\Delta\vartheta\mu^2+\int_0^1 \frac{1}{2}\mu\bar{v}_{1s}\bar{r}\,d\bar{r}-\int_0^1 \bar{v}_{2c}\bar{r}^2 d\bar{r}+\frac{1}{3}\mu a_1^* \\
p_2 &= -\int \frac{1}{2}\mu\bar{v}_{1c}\bar{r}\,d\bar{r}-\int_0^1 \bar{v}_{2s}\bar{r}^2 d\bar{r}-\frac{1}{4}\mu^2 a_0+\frac{1}{3}\mu b_1^* \\
q_1 &= \frac{3}{\chi\gamma}-K\left(\frac{1}{4}+\frac{1}{8}\mu^2\right) \\
q_2 &= \frac{1}{2}-\frac{1}{8}\mu^2
\end{aligned}$$

Here, we noticed that amplitudes of the higher order harmonics of the flapping coefficients are smaller than those of lower order harmonics. In determining $a_n$ and $b_n$, only $a_{n-2}$, $b_{n-2}$, $a_{n-1}$, $b_{n-1}$ are taken into account and $a_{n+1}$, $b_{n+1}$, $a_{n+2}$, $b_{n+2}$

In addition, we get

$$\begin{aligned}
C_T &= \chi\frac{k}{\pi}a_\infty\bar{b}\left[\vartheta_0^*\left(\frac{1}{3}+\frac{1}{2}\mu^2\right)+\Delta\vartheta\left(\frac{1}{4}+\frac{1}{4}\mu^2\right)\right. \\
&\quad \left.+\frac{1}{2}\lambda_0^*-\int_0^1 \bar{v}_0\bar{r}\,d\bar{r}-\int_0^1 \frac{1}{2}\mu\bar{v}_{1s}d\bar{r}\right]
\end{aligned} \tag{4-7}$$

In the equations of the flapping coefficients $a_0$, $a_1^*$, $b_1^*\cdots$ and strain coefficient $C_T$, when compared with the classical equations, the

difference is that terms regarding the induced velocity integrals are added. Using equation (3-7), we carried out the integration and further obtained:

$$C_T = \chi \frac{k}{\pi} a_\infty \bar{b}\left[\vartheta_0^*\left(\frac{1}{3(1+A_0^0)} + \frac{1}{2(1+A_{1s}^{1s})}\mu^2 - \frac{A_{1s}^0/\cos\alpha_1}{2(1+A_0^0)(1+A_{1s}^{1s})}\mu^2\right)\right.$$
$$+\Delta\vartheta\left(\frac{1}{4(1+A_0^0)} + \frac{1}{4(1+A_{1s}^{1s})}\mu^2 - \frac{A_{1s}^0/\cos\alpha_1}{4(1+A_0^0)(1+A_{1s}^{1s})}\mu^2\right)$$
$$\left.+\lambda_0^*\left(\frac{1}{2(1+A_0^0)} - \frac{A_{1s}^0/\cos\alpha_1}{(1+A_0^0)(1+A_{1s}^{1s})}\mu^2\right)\right] \qquad (4\text{-}8)$$

$$a_0 = \chi\gamma\left[\vartheta_0^*\left(\frac{1}{4(1+A_0^0)} + \frac{1}{4(1+A_{1s}^{1s})}\mu^2 - \frac{A_{1s}^0/\cos\alpha_1}{4(1+A_0^0)(1+A_{1s}^{1s})}\mu^2\right)\right.$$
$$+\Delta\vartheta\left(\frac{1}{5(1+A_0^0)} + \frac{1}{6(1+A_{1s}^{1s})}\mu^2 - \frac{A_{1s}^0/\cos\alpha_1}{6(1+A_0^0)(1+A_{1s}^{1s})}\mu^2\right)$$
$$\left.+\lambda_0^*\left(\frac{1}{3(1+A_0^0)} - \frac{A_{1s}^0/\cos\alpha_1}{2(1+A_0^0)(1+A_{1s}^{1s})}\mu^2\right)\right] - \frac{\bar{g}\bar{S}}{\bar{J}} \qquad (4\text{-}9)$$

$$a_1^* = \left[\vartheta_0^*\mu\left(\frac{1}{3(1+A_0^0)} + \frac{1}{3(1+A_{1s}^{1s})} - \frac{A_{1s}^0/\cos\alpha_1}{3(1+A_0^0)(1+A_{1s}^{1s})}\right)\right.$$
$$+\Delta\vartheta\mu\left(\frac{1}{4(1+A_0^0)} + \frac{1}{4(1+A_{1s}^{1s})} - \frac{A_{1s}^0/\cos\alpha_1}{4(1+A_0^0)(1+A_{1s}^{1s})}\right)$$
$$\left.+\lambda_0^*\mu\left(\frac{1}{2(1+A_0^0)} - \frac{A_{1s}^0/\cos\alpha_1}{2(1+A_0^0)(1+A_{1s}^{1s})}\right)\right]$$
$$\left[\frac{1}{4(1+A_{1s}^{1s})} + \frac{A_{1s}^0/\cos\alpha_1}{4(1+A_0^0)(1+A_{1s}^{1s})}\mu^2 - \frac{1}{4(1+A_0^0)}\mu^2 + \frac{1}{3}\mu^2\right] \qquad (4\text{-}10)$$

$$b_1^* = \left[\frac{1}{3(1+A_{1c}^{1c})}\mu a_0 + \frac{A_{1c}^0}{(1+A_0^0)(1+A_{1c}^{1c})}\left(0.08\vartheta_0^* + 0.04\Delta\vartheta\right.\right.$$
$$\left.\left.+0.2\left(\lambda_0^* + \frac{1}{2}\mu a_1^*\right)\right)\right] \Big/ \left[\frac{1}{4(1+A_{1c}^{1c})} + \frac{\mu^2}{8}\right] \qquad (4\text{-}11)$$

where $\bar{v}_{2s}$ and $\bar{v}_{2c}$ were omitted.

It can be observed from equations (4-8), (4-9) and (4-11) that under the same flight conditions $(\lambda_0^*, \mu, \vartheta_0^*)$ the calculated values of $C_T$ and $a_0$ are smaller when the induced velocity variation distribution is considered as compared to those obtained with a constant distribution of induced velocity. However, by the same token $b_1^*$ will be much larger. Just as discussed in [7] and [9], the longitudinal distribution of the induced velocity has a significant effect on the size term $b_1^*$ of the flapping coefficient. This is very important for lateral control. This paper for the first time introduced the analytical

expressions of $C_T$ and flapping coefficients which are only dependent on the flight parameters but has taken induced velocity variation distribution into account.

In addition, we have:

$$a_2=(q_{22}p_{11}+q_{12}p_{22})/(q_{11}q_{22}+q_{12}q_{21})$$
$$b_2=(q_{11}p_{22}-q_{21}p_{11})/(q_{11}q_{22}+q_{12}q_{21}) \qquad (4\text{-}12)$$

where the definitions of $p_{11}$, $p_{22}$, $q_{11}$, $q_{12}$, $q_{21}$, $q_{22}$ are shown in [10].

## V. AIRLOADS

Substituting the expression of harmonics of the induced velocity (3-7) into that of the circulations (3-6), we can get the following matrix form circulation equation:

$$\begin{Bmatrix} \bar{\Gamma}_0 \\ \bar{\Gamma}_{1c} \\ \bar{\Gamma}_{1s} \\ \bar{\Gamma}_{2c} \\ \bar{\Gamma}_{2s} \end{Bmatrix} = \frac{a_\infty \bar{b}}{2}[Q] \begin{Bmatrix} \theta_0^* \\ \Delta\theta \\ \lambda_0^* \\ a_0 \\ a_1^* \\ b_1^* \\ a_2 \\ b_2 \end{Bmatrix} \qquad (5\text{-}1)$$

where the elements of the matrix [Q] are shown in Appendix 1 in [10].

Then substituting circulation equation (5-1) into the airload equation (3-9) for blades, we finally get

$$\begin{Bmatrix} \left(\frac{dC_{T1}}{d\bar{r}}\right)_0 \\ \left(\frac{dC_{T1}}{d\bar{r}}\right)_{1c} \\ \left(\frac{dC_{T1}}{d\bar{r}}\right)_{1s} \\ \left(\frac{dC_{T1}}{d\bar{r}}\right)_{2c} \\ \left(\frac{dC_{T1}}{d\bar{r}}\right)_{2s} \end{Bmatrix} = \frac{a_\infty \bar{b}}{\pi}[P] \begin{Bmatrix} \theta_0^* \\ \Delta\theta \\ \lambda_0^* \\ a_0 \\ a_1^* \\ b_1^* \\ a_2 \\ b_2 \end{Bmatrix} \qquad (5\text{-}2)$$

where the matrix [P] is:

$$[P]=\begin{bmatrix} \bar{r} & 0 & \frac{\mu}{2} & 0 & 0 \\ 0 & \bar{r} & 0 & 0 & \frac{\mu}{2} \\ \mu & 0 & \bar{r} & -\frac{\mu}{2} & 0 \\ 0 & 0 & -\frac{\mu}{2} & \bar{r} & 0 \\ 0 & \frac{\mu}{2} & 0 & 0 & \bar{r} \end{bmatrix} [Q]$$

## VI. EXAMPLE

In order to explain this method, we used the Yen-2 helicopter rotor blade as an example to calculate the flapping coefficients under the seven flight conditions of $\mu = 0.05,\ 0.075,\ 0.10,\ 0.125,\ 0.15,\ 0.20,\ 0.24$ and the airload where $\mu = 0.20$.

$R = 5$ m
$\Delta\vartheta = -0.1396$ rad
$K = 0.3$
$m_1 = 2.755$ kg·sec²/m
$\rho_H = 0.108$ kg·sec²/m⁴
$\bar{b} = 0.0486$
$\bar{e} = 0.014$
$k = 3$
$\Omega = 37.48$ rad/sec
$a_\infty = 5.73$

The flight parameters were obtained from the balance calculation of the craft. Using $\mu = 0.20$ as an example

$\bar{V}_i = 0.2053$
$\vartheta_0^* = 0.2409$ rad
$\cos\alpha_1 = 0.9741$
$\lambda_0^* = -0.02494$

Based on equations (4-9), (4-10), (4-11), (4-12) and (4-13) to calculate the flapping coefficients, we obtained the curves showing the relations between $a_0$, $a_1^*$, $b_1^*$, $a_2$, $b_2$ and the advance ratio $\mu$ as Figures 1, 2, 3, 4 and 5 respectively.

For comparison purposes, the flapping coefficients obtained with constant induced velocities are also shown in these figures. We can see that, as we described before, the $a_0$ curve with induced velocity variation distribution is lower than that with constant induced velocity.

The $a_1^*$ curves for both types of distribution are almost identical. However, the $b_1^*$ curves of both distributions are quite different. The former is greater than the latter especially exhibiting peak values in the low velocity region. This phenomenon has been observed many times in experiments. $a_2$ and $(-b_2)$ curves are similar to those of $b_1^*$ but they are less than 1/10th of that of $b_1^*$. From these observations, it is reasonable to neglect higher order flapping coefficients in the calculation of lower order flapping coefficients.

Finally, based on the equations of induced velocities and various orders of harmonics of blade airloads (3-7) and (5-2), the distributions of $\bar{v}_0$, $\bar{v}_{1c}$, $\bar{v}_{1s}$, $\bar{v}_{2c}$, $\bar{v}_{2s}$ and $\left(\frac{dT_1}{dr}\right)_0$, $\left(\frac{dT_1}{dr}\right)_{1c}$, $\left(\frac{dT_1}{dr}\right)_{1s}$, $\left(\frac{dT_1}{dr}\right)_{2c}$, $\left(\frac{dT_1}{dr}\right)_{2s}$ along the radius under the condition $\mu = 0.2$ were calculated. The results are as shown in Figures 6-10 and 11-15. In order to verify the validity of this simplified method in this paper, the varous harmonics of airloads of rotor blade obtained using numerical integration [11] are also shown in Figures 11-15. It is clear that the results of airloads obtained using two different methods are the same. In addition, Figure 16 shows the curve of variation of airload along the azimuth angle at different radial distances. The trend of these curves is also very similar to that discussed in [1]

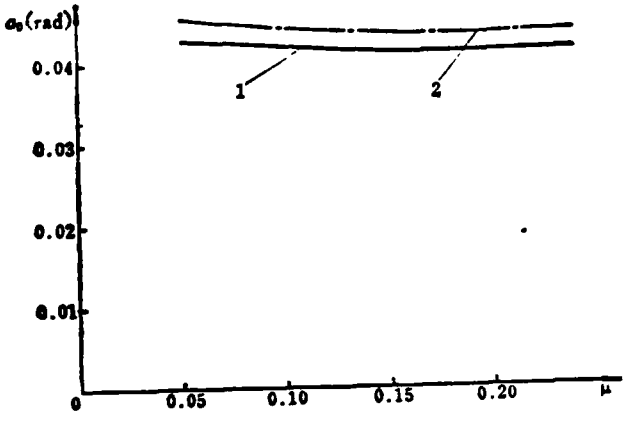


Fig.1 Coning angle $a_0$ vs. advance ratio $\mu$
1—equation in this paper
2—classical equations

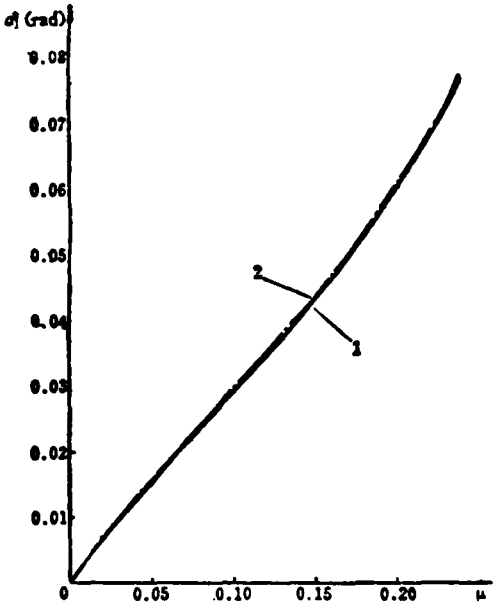


Fig.2 Flapping coefficient $a_1^*$ vs. advance ratio $\mu$
1—equations in this paper
2—classical equations

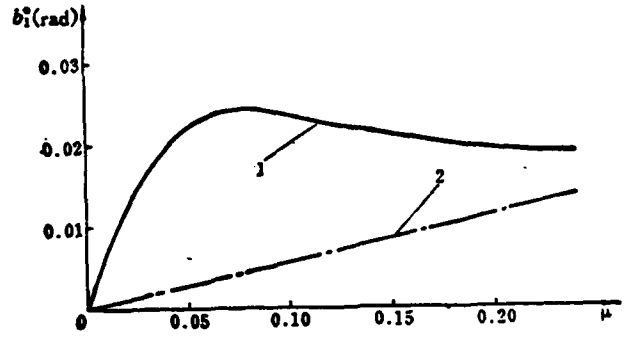


Fig.3 Flapping coefficient $b_1^c$ vs. advance ratio $\mu$
1—equations in this paper; 2—classical equations

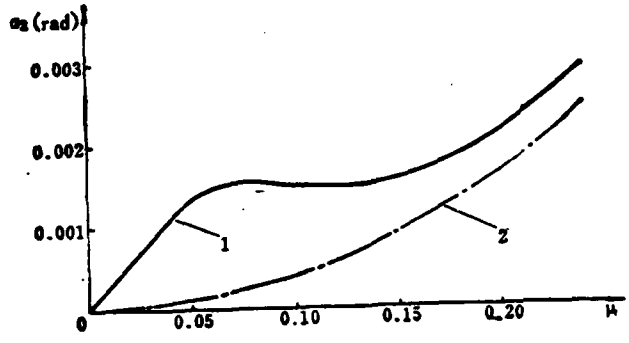


Fig.4 Flapping coefficient $a_2$ vs. advance ratio $\mu$
1—equations in this paper
2—classical equations

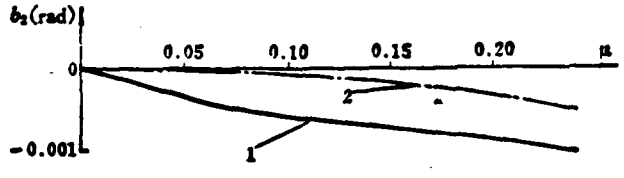


Fig.5 Flapping coefficient $b_2$ vs. advance ratio $\mu$
1—equations in this paper; 2—classical equations

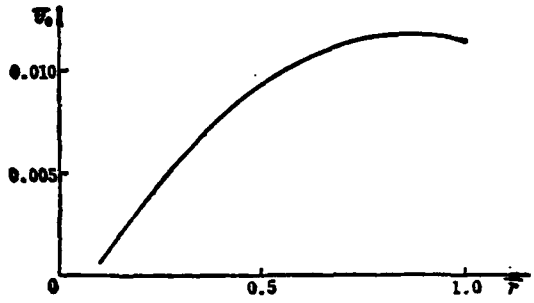


Fig. 6 Distribution of the induced velocity $\bar{v}_0$ along radius for $\mu = 0.20$

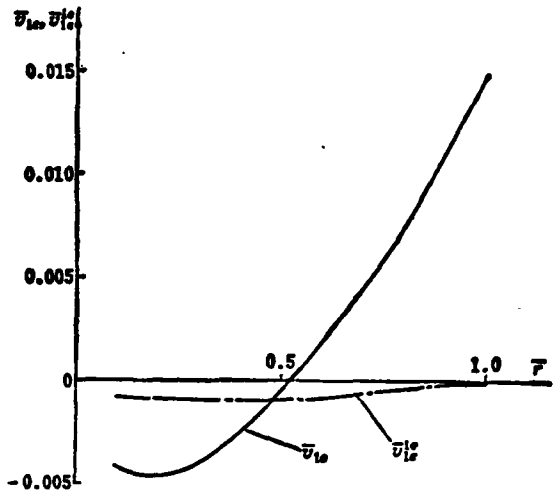


Fig. 7 Distribution of the induced velocity $\bar{v}_{1c}$ along radius for $\mu = 0.20$

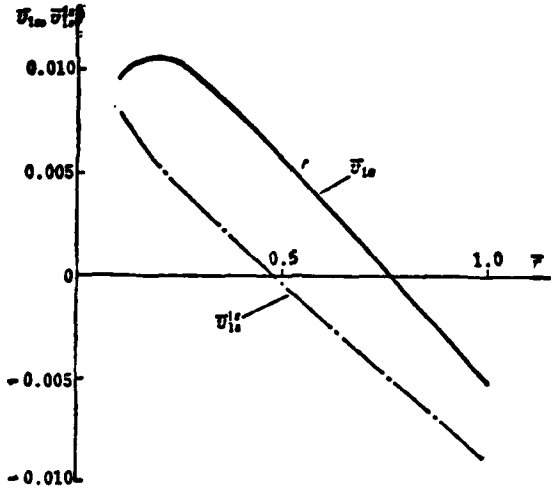


Fig. 8 Distribution of the induced velocity $\bar{v}_{1s}$ along radius for $\mu = 0.20$

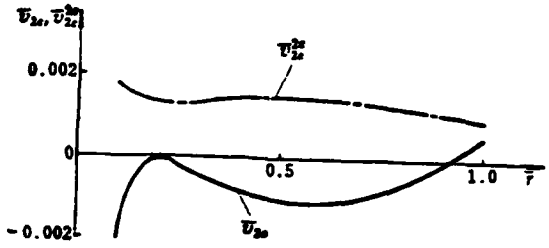


Fig.9 Distribution of the induced velocity $\bar{v}_{2s}$ along radius for $\mu = 0.20$

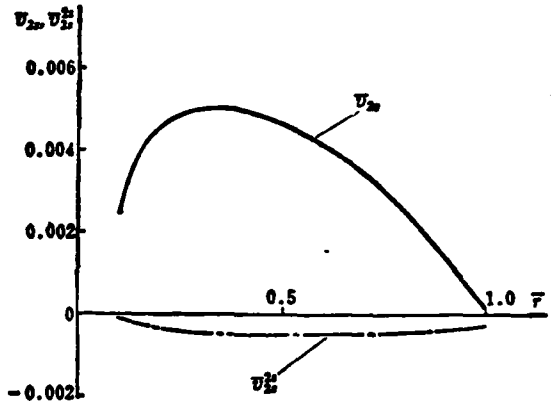


Fig.10 Distribution of the induced velocity $\bar{v}_{2s}$ along radius for $\mu = 0.20$

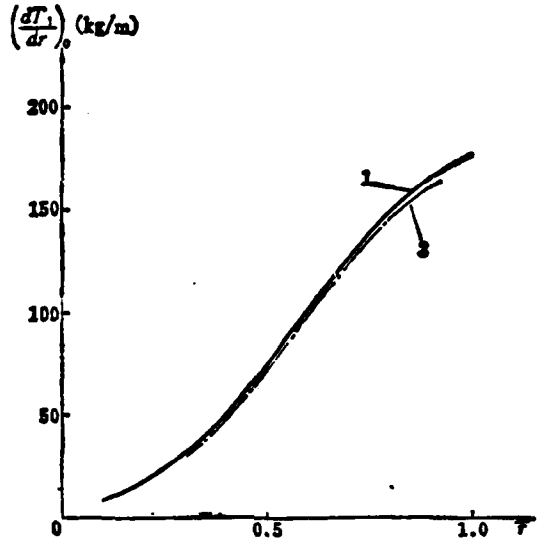


Fig.11 Distribution of the blade airload $\left(\frac{dT_1}{d}\right)_0$ along radius for $\mu = 0.20$

1--equations in this paper; 2--numerical solutions

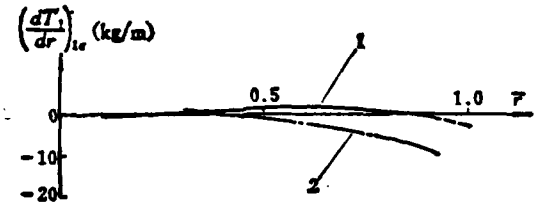


Fig.12 Distribution of the blade airload $\left(\frac{dT_1}{dr}\right)_{1\sigma}$ along radius for $\mu = 0.20$
1—equations in this paper; 2—numerical solutions

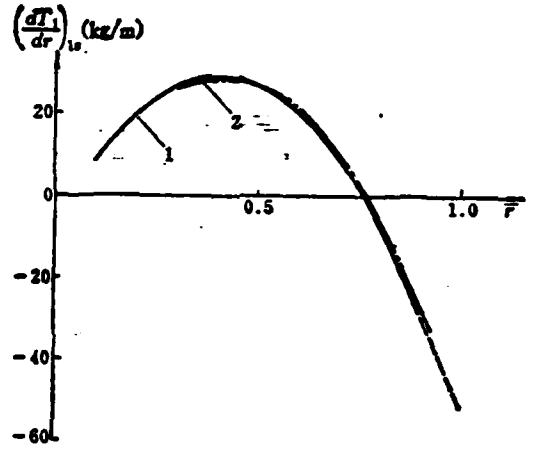


Fig.13 Distribution of the blade airload $\left(\frac{dT_1}{dr}\right)_{1\sigma}$ along radius for $\mu = 0.20$
1—equations in this paper; 2—numerical solutions

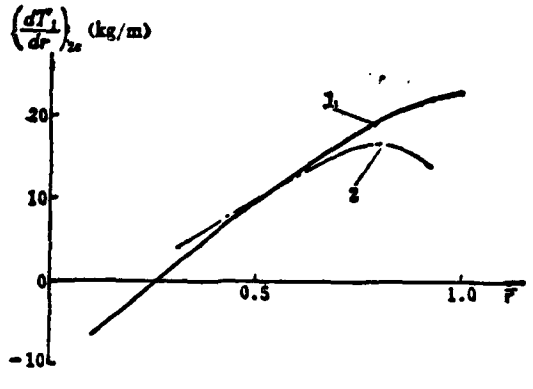


Fig.14 Distribution of the blade airload $\left(\frac{dT_1}{dr}\right)_{2\sigma}$ along radius for $\mu = 0.2$
1—equations in this paper; 2—numerical solutions

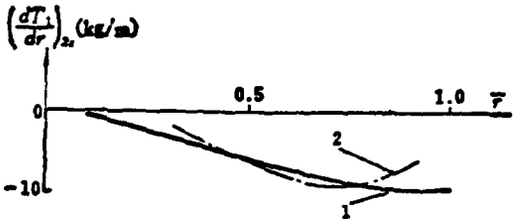


Fig.15 Distribution of the blade airload $\left(\frac{dT_1}{dr}\right)_{2s}$ along radius for $\mu = 0.20$
1—equations in this paper; 2—numerical solutions

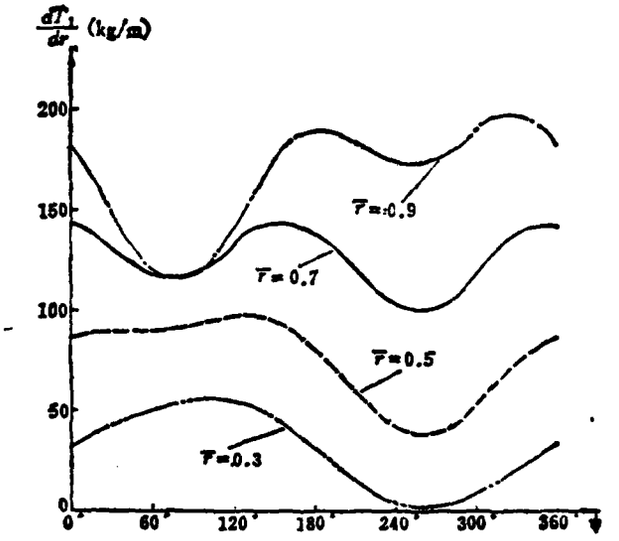


Fig.16 Variation of the blade airloads $\frac{dT_1}{dr}$ along azimuth for different radial distances

## VII CONCLUSIONS

The major conclusions of this work are summarized in the following:

(1) Based on the classical vortex theory of rotor and the blade element theory, a closed form relation between induced velocity and circulation has been established.

(2) For the first time analytical expressions for the flapping coefficient and blade airload which not only take effect of the variation distribution of the induced velocity into account but also only depend on blade parameters and flight parameters.

(3) The method to estimate rotor airload introduced in this paper is simple and suitable for engineering applications.

## REFERENCES


[1] Specialists Meeting on Helicopter Rotor Loads Prediction Methods AGARD-CP-122 (1973).

[2] (U.S.) Army Aviation RDT&E Plan. AD-AO35334 (1976).

[3] A. J. Landgrebe, et al. Aerodynamic Technology for Advanced Rotorcraft-Part 2. J. of A. H. S. (1977) 22 (3).

[4] Wang Shicun. "Generalized vortex theory of the lift blade of helicopters", Research Information at Northwest Industrial University (1962).

[5] "Airload of rotor in the flapping plane", Nanjing Aeronautic Institute Research Information, First part in Induced Velocity, serial no. 065 (1975).

[6] "Airload of rotor in the flapping plane", Nanjing Aeronautic Institute Research Information, Second part in Circulation Equation 5, serial no. 087 (1976).

[7] Meli et al. "Calculation and design of helicopters", vol. 1 in Aerodynamics, Published by Defense Publication Agency (1977).

[8] Wang Shicun. "Induced velocity distribution of lift blade", Acta Mechanica 7, 3 (1964).

[9] F. D. Harris Articulated Rotor Blade Flapping Motion at Low Adance Ratio. J. of A. H. S. (1972) 17 (1).

[10] Wang Shicun and Xu Zhi. A simplified method for predicting rotor blade airloads. Seventh European Rotorcraft and Powered Lift Aircraft Forum paper no. 6 (1981) (9).

[11] Chu Shuchen, Lee Nanhwi. "Calculation and Analysis of Helicopter Rotor Airloads", Nanjing Aeronautic Institute Journal, (3), (1979).

# A SIMPLIFIED METHOD FOR PREDICTING ROTOR BLADE AIRLOADS

*Wang Shicun and Xu Zhi*
(*Nanjing Aeronautical Institute*)

**Abstract**

At present, a simplified approach to the prediction of rotor blade airloads is urged to be developed in the engineering application.

In this paper, firstly, relations of first two harmonic induced velocities to the lower and same-order harmonic circulations are obtained from the generalized classical vortex theory of the rotor. Then, based on the blade element theory, a closed form of equations for circulation is established and, by taking the flapping condition into account, simplified formulae for predicting rotor blade airloads are set up. In particular, expressions of flapping coefficients are derived, including the effect of variable induced velocity distribution but in terms of blade parameters and flight parameters only.

Finally, a calculation of a typical example is made and comparisions of airloads with those from the more accurate numerical solution are shown that the present method is fairly suitable for aerodynamic analysis and preliminary design of helicopters.

# STUDY ON PRESSURE DISTRIBUTION ON ROTOR BLADES WITH THREE-DIMENSIONAL NON-STEADY THEORY OF COMPRESSED FLUID

Jiangxi Aeronautical Society, Li Zenhao and Ruan Ticusen

ABSTRACT

A solution to the pressure distribution on rotor blades three-dimensional nonsteady theory of compressible fluid is presented in this paper in the case of continuous wake-surface and instant speed forward motion of a helicopter. In order to satisfy the wake conditions, it is assumed that the pressure doublets move along the wake surface instead of along the actual tracks of blades. By adding the moving pressure doublets, an integral equation of the three-dimensional nonsteady compressible fluid with superior singularity is obtained when the blades are in complex motion. A method to treat this superior singularity was obtained to make it a continuous integral equation with super extreme values. Furthermore, the numerical solution of this equation was also obtained. The accuracy of the method and the equation has been proven based on simple examples using a small computer.

## I. THE PROBLEM

Up until now, the calculation of helicopter rotor loads by tradition adopts a vortex line simulated wake of irregular or non-singular shape and uses the nonsteady incompressible fluid Pierre-Savor equation to obtain the induced velocity at the blades and determines the lateral distribution based on classical blade element theory. The calculated results usually show a lower total lift at higher speeds or a non-zero load at the root and tip of the blade. Even in some cases, it is necessary to manually shift the wake position to approach the experimental results. The error for higher order load is also large. Higher order load is the source of helicopter vibration. Therefore, it is important. The reasons for the above discrepancies lay, of course, in

the assumptions made. It is not uncommon to see the use of acceleration potential to solve nonsteady aerodynamic problems for fixed wing aircraft but it is rarely used in treating rotors. With regard to [1], we will make some comments in the following. As for [2], it only carried out some exploratory discussion. This paper intends to overcome the inadequacy in the area and to develop a new rigorous acceleration potential method with nonsteady theory of compressible fluid taken into account to calculate the airloads of rotors.

Fixed coordinate systems on the ground o-x, y, z and o-r, θ, z are chosen with z-axis positive in the upward direction. At time t = 0, the center of the blade shell coincides with the original. The blade on which the load is calculated is located downwind ($\phi = 0$). x-axis is in the opposite direction to $U_\infty$. $U_\infty$ is the constant forward speed of the helicopter. Assuming that no shock wave and no separation exists in the flow field, the blade only undergoes a flapping elastic motion as shown in Figure 1.

Because the attack angle curvature and thickness are not large when the blades are working, the disturbance generated due to the motion of the blades is very minute. At this time the acceleration position $\phi = -\frac{p - p_\infty}{\rho_\infty}$ exists, and the following equation is satisfied

$$\frac{\partial^2 \phi}{\partial x^2} + \frac{\partial^2 \phi}{\partial y^2} + \frac{\partial^2 \phi}{\partial z^2} - \frac{1}{a_\infty^2} \frac{\partial^2 \phi}{\partial t^2} = 0 \qquad (1)$$

The following is to determine the relation between the acceleration potential and velocity potential $\bar{\phi}$. According to nonsteady Bernoulli equation, the acceleration potential at reposity is zero.

---

received in May 1981

$$\frac{\partial \bar{\phi}}{\partial t} + \frac{v^2}{2} = \phi$$



but because:

$$\frac{d\bar{\phi}}{dt} = \frac{\partial \bar{\phi}}{\partial t} + v_x \frac{\partial \bar{\phi}}{\partial x} + v_y \frac{\partial \bar{\phi}}{\partial y} + v_z \frac{\partial \bar{\phi}}{\partial z} = \frac{\partial \bar{\phi}}{\partial t} + v^2$$

therefore

$$\phi = \frac{\partial \bar{\phi}}{\partial t} + \frac{v^2}{2} = \frac{d\bar{\phi}}{dt} - \frac{v^2}{2} = -\frac{p - p_\infty}{\rho_\infty}$$

When a helicopter is suspending, the axial induced velocity is the largest. Based on the momentum principle, $v_0=(T/2\pi\rho R^2)^{1/2}$, where T is the weight of the flying object. Therefore, $\frac{v^2}{2}\approx\frac{v_z^2}{2}\approx T/(4\rho\pi R^2)\approx \frac{T}{(\rho S)}\cdot\frac{S}{(4\pi R^2)}\approx\frac{\Delta p}{\rho}\cdot\frac{S}{(4\pi R^2)}$ but $S/(4\pi R^2)$ in reality is between 0.07-0.1. Therefore, $v^2/2$ is far less than $(p-p_\infty)/\rho_\infty$ So, under small disturbance conditions:

$$\phi=-\frac{\partial\bar{\phi}}{\partial t}=\frac{d\bar{\phi}}{dt}$$

or

$$\bar{\phi}=\int_{-\infty}^{t}\phi dt \qquad (2)$$

only t is a variable in the integration, x, y and z do not vary.

It is clear from the above discussion that $\phi=\frac{d\bar{\phi}}{dt}$ and $\text{grad}\,\phi=\frac{d\vec{v}}{dt}$ are not identical when $v^2/2$ cannot be neglected.

When an acceleration potential method is used, it must satisfy

(1) at infinity, the pressure is $p_\infty$, and $\phi = 0$

(2) the acceleration potential $\phi$ satisfies the wave equation (1)

(3) the velocity potential satisfies equation (2)

(4) the wake created by the motion of the rotor produces a wake-surface in the flow field. The wake-surface is dragging out of the rear fringe of the blade. At any instance across the wake-surface, the velocity potential $\bar{\phi}$ is non-continuous with a sudden jump in quantity

(5) on the surface of a moving blade, boundary conditions are satisfied. This means that the normal component of the flow velocity at any point on the surface at any instance is equal to the instantaneous velocity component at this point.

## II. MOVING DOUBLET ACCELERATION POTENTIAL INTEGRAL EQUATION

Doublets are distributed in the flow filled to satisfy the five conditions mentioned before. Doublets are expressed as $(\xi,\eta,\zeta)$ and the calculation points in the flow filled are (x,y,z). In order to satisfy condition (4), doubtlets move along the wake-surface. Let us assume at time $t_1$, the doublet is located at $R_1$ and at $t_2$ it moves to $R_2$, then $\phi$ has a discontinuity across the surface from $R_1$ at $t_1$ to $R_2$ at $t_2$. However, $\phi$ does not jump at $R_1$ when time is $t_2$. As for $\bar{\phi}$,

from equation (2), it is clear that $\bar{\phi}$ is continuous because $\phi$ is continuous at any point outside the wake-surface. When crossing the wake surface, $\bar{\phi}$ also leaps. This leap occurs at between $t_1$ and $t_2$. Therefore, moving the doublet along the wake surface will make the motion satisfy condition (4).

The moving doublet acceleration potential is

$$\phi(x, y, z, t) = -\frac{1}{4\pi} \frac{\partial}{\partial n_0} \frac{f(\tau)a_\infty}{a_\infty \alpha + Q_\infty} \qquad (3)$$

$n_o$ is the axial direction of the doublet, from junction pointing toward the source. In this paper, the junction is placed on the wake surface or under the blade. Partial derivatives are made with respect to ($\xi$,$\eta$, $\zeta$). $f(\tau)$--doublet strength function; $a_\infty$--undisturbed sonic velocity.

$$\tau = t - \frac{\alpha}{a_\infty} \qquad (4)$$

$\alpha$--distance between doublet point and flow field point

$$\alpha = \sqrt{[x-\xi(\tau)]^2+[y-\eta(\tau)]^2+[z-\zeta(\tau)]^2} \qquad (5)$$

$$Q_\infty = -(x-\xi)\xi'(\tau)-(y-\eta)\eta'(\tau)-(z-\zeta)\zeta'(\tau) \qquad (6)$$

After substituting (3) into the wave equation and repeatedly carrying out mathematical operations, it is possible to prove that (3) satisfies the wave equation $\xi,\eta,\zeta$ are the coordinates of the doublet when it is moving along an arbitrary curve. From (3)-(6), it is demonstrated that the parameter $a_\infty$ which represents the effect of compressibility is incorporated into the pressure verturbation in a complicated form. It does not follow a correction such as $\sqrt{1-M_{\infty}^2}$ as used in Planto's correction.

Let the number of blades be MM. The potential difference between the mth blade and the blade on which the load is calculated is $\bar{\psi}m$, $\bar{\psi}m = (m-1)\ 2\pi/MM$. Then introduce the blade coordinates, $\rho$, $\theta_o$; r, $\psi_o$ as shown in Figure 1. $\theta_o$, ($\psi_o$) is positive when pointing toward the front fringe. The doublet is moving on the surface of the blade when traveling from the corresponding position on the blade surface to the rear fringe. For simplification, let us assume that it moves on the z = 0 plane. Beyond the rear fringe, the motion of the doublet is affected by the perpendicularly downward wash velocity w and it is

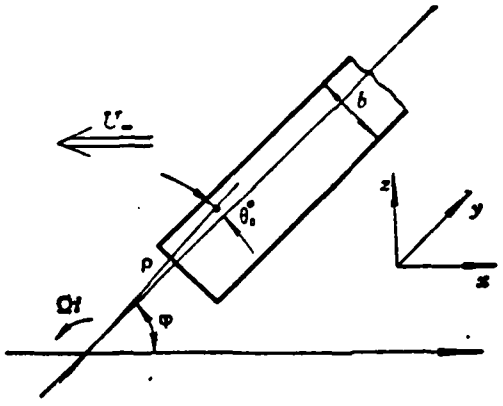


Fig.1 Blade and coordinate

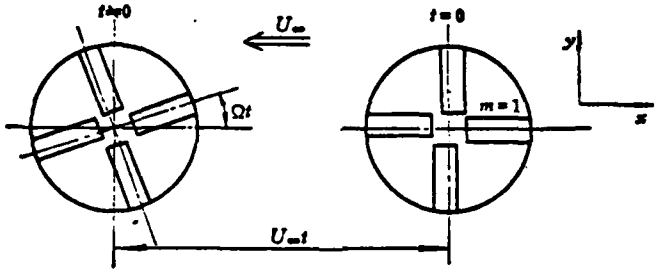


Fig.2 Blades positions at different moment

dragged downward. Assuming w is a constant, it corresponds to a non-irregular wake.

Let the time for the doublet to move from the doublet point to the rear fringe be $t_{01}$,

$$t_{01}=(\rho\sin\theta_0+0.75\,b)/[\rho\Omega+U_\infty\sin(\varphi+\bar{\psi}_\infty)] \tag{7}$$

According to Figures 1 and 2, we get

$$x=-U_\infty\frac{\varphi}{\Omega}+r\cos(\varphi+\psi_0),\quad y=r\sin(\varphi+\psi_0),\quad z=0 \tag{8}$$

$$\xi=-U_\infty\tau+\rho\cos(\Omega\tau+\bar{\psi}_\infty+\theta_0),\quad \eta=\rho\sin(\Omega\tau+\bar{\psi}_\infty+\theta_0),\quad \zeta=w\left[\tau-\left(\frac{\varphi}{\Omega}-t_{01}\right)\right] \tag{9}$$

$$w=\begin{cases}0 & \dfrac{\varphi}{\Omega}\geqslant\tau\geqslant\dfrac{\varphi}{\Omega}-t_{01}\\ \text{constant} & \dfrac{\varphi}{\Omega}-t_{01}\geqslant\tau\geqslant-\infty\end{cases} \tag{10}$$

$$\alpha=\left\{\left[r\cos(\varphi+\psi_0)-\rho\cos(\Omega\tau+\bar{\psi}_\infty+\theta_0)+U_\infty\left(\tau-\frac{\varphi}{\Omega}\right)\right]^2\right.$$
$$\left.+\left[r\sin(\varphi+\psi_0)-\rho\sin(\Omega\tau+\bar{\psi}_\infty+\theta_0)\right]^2+\left(z-w\left[\tau-\left(\frac{\varphi}{\Omega}-t_{01}\right)\right]\right)^2\right\}^{1/2} \tag{11}$$

$$Q_\infty=-\left[r\cos(\varphi+\psi_0)-\rho\cos(\Omega\tau+\bar{\psi}_\infty+\theta_0)+U_\infty\left(\tau-\frac{\varphi}{\Omega}\right)\right]\left[-U_\infty-\rho\Omega\sin(\Omega\tau+\bar{\psi}_\infty+\theta_0)\right]-\left[r\sin(\varphi+\psi_0)-\rho\sin(\Omega\tau+\bar{\psi}_\infty+\theta_0)\right]\rho\Omega\cos(\Omega\tau+\bar{\psi}_\infty+\theta_0)$$
$$-\left\{z-w\left[\tau-\left(\frac{\varphi}{\Omega}-t_{01}\right)\right]\right\}w \tag{12}$$

In order to find the partial derivatives $\frac{\partial}{\partial n_0}$, in the normal direction, it is necessary to obtain the normal directional number of the slanted helicoidal surface forward by the trajectory of the doublet. Solving (9) simultaneously, we get

$$\xi=-U_\infty\left(\frac{\zeta}{w}+\frac{\varphi}{\Omega}-t_{01}\right)+\eta\ \mathrm{ctg}\left[\Omega\left(\frac{\zeta}{w}+\frac{\varphi}{\Omega}-t_{01}\right)+\bar{\psi}_\infty+\theta_0\right] \tag{13}$$

Taking partial derivatives of (13) with respect to $\xi$, $\eta$ and $\zeta$, we get the normal directional numbers

$$w\sin(\Omega\tau+\bar{\psi}_\infty+\theta_0),\ -w\cos(\Omega\tau+\bar{\psi}_\infty+\theta_0),\ \rho\Omega+U_\infty\sin(\Omega\tau+\bar{\psi}_\infty+\theta_0) \tag{14}$$

After that, we must use $\lim_{z\to 0}\frac{\partial}{\partial z}\ \frac{\partial}{\partial n_0}\ \frac{f(\tau)a_\infty}{a_\infty\alpha+Q_\infty}$, and carry out complicated operations to get the following:

$$\lim_{z\to 0}\frac{\partial}{\partial z}\ \frac{\partial}{\partial n_0}\ \frac{f(\tau)a_\infty}{a_\infty\alpha+Q_\infty}=f(\tau)\frac{be+(QA\cdot bc)/(bd\cdot\alpha)}{\alpha^3\cdot bd\cdot\sqrt{w^2+be^2}}$$
$$+\frac{f'(\tau)}{a_\infty}\ \frac{QA\cdot bf+be\cdot\alpha\sqrt{bd}}{\alpha^3 bd\ \sqrt{w^2+be^2}}+\frac{f''(\tau)}{a_\infty^2}\ \frac{QA\cdot\zeta}{\alpha^3\sqrt{bd}\sqrt{w^2+be^2}} \tag{15}$$

where
$$be=\rho\Omega+U_\infty\sin(\Omega\tau+\bar{\psi}_\infty+\theta_0)$$
$$QA=(x-\xi)w\sin(\Omega\tau+\bar{\psi}_\infty+\theta_0)+(y-\eta)(-w)\cos(\Omega\tau+\bar{\psi}_\infty+\theta_0)-\zeta\cdot be$$
$$bc=\frac{\zeta}{\alpha}\left[3+\frac{Q_\infty}{a_\infty\alpha}\left(4+\frac{Q_\infty}{a_\infty\alpha}\right)\right]+\frac{2w}{a_\infty}\left(1+\frac{Q_\infty}{a_\infty\alpha}\right)$$
$$bd=\left(1+\frac{Q_\infty}{a_\infty\alpha}\right)^2$$
$$bf=\frac{\zeta}{\alpha}\cdot\left(3+\frac{Q_\infty}{a_\infty\alpha}\right)+\frac{w}{a_\infty} \tag{16}$$

$\alpha$, $Q_\infty$ are equations (11) and (12) where z = 0.

When the doublet is moving arbitrarily, the relation between the pressure differential and the acceleration potential strength is

$$\frac{p_\tau-p_\perp}{\rho_\infty}=-f(\tau) \tag{17}$$

when the helicopter is flying forward at a constant speed $U_\infty$, $p_{down}-p_{up}=\Delta p$ can be written as: ($\bar{\xi}_1$, $\bar{\eta}_1$ are the dimensionless orthogonal coordinates of the blades).

$$\Delta p=\sum_{n=0}^{\infty}\Delta p_n(\bar{\xi}_1,\ \bar{\eta}_1)e^{in(\Omega\tau+\bar{\psi}_\infty)} \tag{18}$$

Therefore, the velocity potential generated by the doublet is

$$\bar{\phi}=\frac{1}{4\pi\rho_\infty}\int_{-\infty}^{\varphi/\Omega}\sum_{n=0}^{\infty}\Delta p_n(\bar{\xi}_1,\ \bar{\eta}_1)\frac{\partial}{\partial n_0}\ \frac{e^{in(\Omega\tau+\bar{\psi}_m)}}{\alpha+Q_m/a_\infty}dt$$

The above equation is for a corresponding infinitestimal area. For the entire rotor, doublets are distributed on all the blade surfaces. Therefore, we have to integrate with respect to the surface of the blade and to add the number of blades to it. We get

$$\bar{\phi}=\frac{S}{4}\ \frac{1}{4\pi\rho_\infty}\int_{-1}^{1}\int_{-1}^{1}d\bar{\xi}_1 d\bar{\eta}_1\sum_{n=0}^{\infty}\Delta p_n(\bar{\xi}_1,\ \bar{\eta}_1)$$
$$\times\sum_{m=1}^{MM}\int_{-\infty}^{\varphi/\Omega}\frac{\partial}{\partial n_0}\ \frac{\exp[in(\Omega\tau+\bar{\psi}_m)]}{\alpha+Q_m/a_\infty}dt \qquad (19)$$

where S is the area of a single blade.

By taking the partial derivative on both sides of equation (19) with respect to z and using condition (5) together with assuming that the normal velocity of the arc surface on the blade is $V_z$, we get

$$\lim_{z\to\text{某量}}\frac{\partial\bar{\phi}}{\partial z}\approx\lim_{z\to 0}\frac{\partial\bar{\phi}}{\partial z}=V_n(r,\ \psi_0,\ \varphi)=\frac{S}{4}\ \frac{1}{4\pi\rho_\infty}\lim_{z\to 0}\frac{\partial}{\partial z}\int_{-1}^{1}\int_{-1}^{1}d\bar{\xi}_1 d\bar{\eta}_1$$
$$\times\sum_{n=0}^{\infty}\Delta p_n(\bar{\xi}_1,\ \bar{\eta}_1)\sum_{m=1}^{MM}\int_{-\infty}^{\varphi/\Omega}\frac{\partial}{\partial n_0}\ \frac{\exp[in(\Omega\tau+\bar{\psi}_m)]}{\alpha+Q_m/a_\infty}dt \qquad (20)$$

When the integration is carried out, the relation between $\bar{\xi}_1$, $\bar{\eta}_1$ and $\rho$, $\theta_0$ must be used. Based on Figure 3, we get

$$\left.\begin{aligned}&\bar{\xi}_1=\frac{-2\rho\sin\theta_0}{b}-0.5,\ \ \bar{\eta}_1=\frac{2\rho\cos\theta_0}{L}-1-\frac{2RS}{L}\\&\rho_0=0.5\sqrt{L^2\left(\bar{\eta}_1+1+\frac{2RS}{L}\right)^2+b^2(\bar{\xi}_1+0.5)^2},\ \ \theta_0=\mathrm{tg}^{-1}\ \frac{-b(\bar{\xi}+0.5)}{L\left(\bar{\eta}_1+1+\frac{2RS}{L}\right)}\end{aligned}\right\} \qquad (21)$$

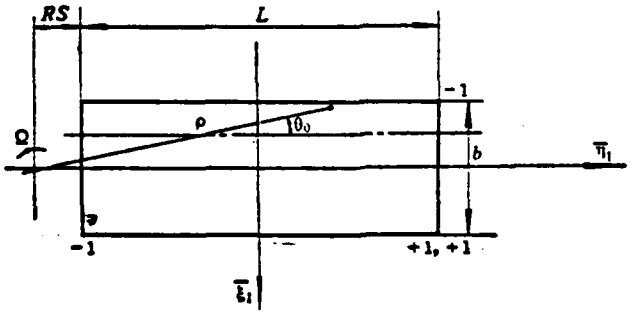


Fig.3 Coordinate $\bar{\xi}_1$, $\bar{\eta}_1$

## III. THE TREATMENT OF ADDITIVE SINGULARITIES OF WAKES

Equation (20) is a singularity integral equation of rotor load under nonsteady compressible conditions. Its core is an integral which has not yet been solved to date. The double integral on the outside and the partial derivatives for finding out the extremes are also very difficult. In addition, pressure differential between the front and rear fringe and boundary conditions at the tips and roots of the blades must be satisfied. In order to find a solution for (20), we have to study the experience of earlier work in the research of aircraft wings.

In [1], the method used to solve the similarity equation s is to use $z \to z_o$ to substitute $z \to 0$. $z_o$ is not equal to zero and it is a small quantity. Based on the calculated results in that paper, it is 0.035 times the arc length. Thus, a continuous integral equation is obtained. That paper still used a numerical method to find the derivatives by choosing a step length of 0.005 times the arc length. It appeared to be quite reasonable significally because the difference in normal direction velocity $V_z$ at $z = 0$ and $z = 0.035$ arc length is not too large. However, this arrangement in practice has a significant amount of artificial arbitrariness. Using the simplest example of the incompressible zero order wing load problem (in the analysis of this method, there is no practical difference between wings and rotors), because of the singularity of the integral, it is not necessary to numerically find the derivatives. It is possible to move the calculation of limits and partial derivatives into the integral. Thus, the kernel becomes $\frac{1}{r}$. After the calculation, it becomes $\frac{1-3z_o^2/r^2}{r^3}$, where r is the distance. When the coordinates x and y of the flow field point and the doublet are identical, which means that we are looking for the point-to-point effect, $r = z_o$. For the kernel of the integral, it becomes $-2/z_{oo}^3$. Therefore, the main diagonal elements of the matrix completely depends on $z_o$. When $z_o$ changes from a small number to a large number, the airload can change from very large to very small. Thus, for different rotor and flight conditions, it is necessary to obtain the load data before $z_o$ can be decided. The meaning of solving the unsteady compressible rotor load problems is completely lost.

In the nonsteady compressible wing problems, the $\lim_{z\to 0}\frac{\partial}{\partial z}$ can be moved into the double integral and the kernal function becomes

$$\lim_{z\to 0}\frac{\partial^2}{\partial z^2}\int_{-\infty}^{x_0}\frac{\exp[i\omega(\lambda-M\sqrt{\lambda^2+\beta^2y^2+\beta^2z^2})]}{\sqrt{\lambda^2+\beta^2y^2+\beta^2z^2}}d\lambda$$

After integrating this equation and isolating the singular point, then it is possible to find the Hadamard principal value of the double integral. If we can separate (20) into two parts, one with singularity and one without it and make the part with singularity to have the same form as the one for wings, then we can use the results of wings to make the rotor loads as the wing loads plus some corrections. This is the method used in this paper.

The following is a derivation of the solution to this equation. Considering that, among the contributions of all the blades, the effect of other blades on the one being calculated is much smaller due to the distance. It can be assumed taht the wakes of other blades fall off from the doublets which correspond to $m \neq 1$ at $t_{01} = 0$. Equation (20) can be written as

$$V_z(r,\ \psi_0,\ \varphi)=\frac{S}{4}\frac{1}{4\pi\rho_\infty}\lim_{z\to 0}\frac{\partial}{\partial z}\int_{-1}^{1}\int_{-1}^{1}d\bar{\xi}_1 d\bar{\eta}_1\sum_{n=0}^{\infty}\Delta p_n(\bar{\xi}_1,\ \bar{\eta}_1)$$
$$\times\left\{\sum_{m=2}^{MM}\int_{-\infty}^{\varphi/\Omega}\frac{\partial}{\partial n_0}\frac{e^{in(\Omega\tau+\hat{\varphi}_m)}}{\alpha+Q_m/a_\infty}dt+\int_{-\infty,(M=1)}^{\varphi/\Omega-t_{01}}\frac{\partial}{\partial n_0}\frac{e^{in\Omega\tau}}{\alpha+Q_m/a_\infty}dt\right. \qquad (22)$$
$$\left.+\int_{\varphi/\Omega-t_{01},(m=1)}^{\varphi/\Omega}\frac{\partial}{\partial n_0}\frac{e^{in\Omega\tau}}{\alpha+Q_m/a_\infty}dt\right\}=V_z^{(1)}+V_z^{(2)}+V_z^{(3)}$$

$V_z^{(1)}$, $V_z^{(2)}$ are continuous and without singularity. Let us move $\lim_{z\to 0}\frac{\partial}{\partial z}$ into the inner integral. $V_Z^{(3)}$ contained all the singularities and transform $\frac{\partial}{\partial n_0}=\frac{\partial}{\partial\zeta}$

$$\frac{\varphi}{\Omega}-t=-t',\quad \frac{\varphi}{\Omega}-\tau=-\tau'$$

$$V_z^{(3)}=\frac{S}{4}\frac{1}{4\pi\rho_\infty}\lim_{z\to 0}\frac{\partial}{\partial z}\int_{-1}^{1}\int_{-1}^{1}d\bar{\xi}_1 d\bar{\eta}_1\sum_{n=0}^{\infty}\Delta p_n(\bar{\xi}_1,\ \bar{\eta}_1) \qquad (23)$$
$$\times\int_{-t_{01}}^{0}\frac{\partial}{\partial\zeta}\frac{\exp[in(\varphi+\Omega\tau)]}{\alpha+Q_m/a_\infty}dt$$

Let us transform r, $\psi_o$; $\rho$, $\theta_o$ into the blade coordinates $x_1$, $y_1$, $\xi_1$, $\eta_1$, according to equation (21)

$$\left.\begin{aligned} \rho\sin\theta_0 &= -\xi_1 - \frac{b}{4}, \quad r\sin\psi_0 = -x_1 - \frac{b}{4} \\ \rho\cos\theta_0 &= \eta_1 + \frac{L}{2} + RS, \quad r\cos\psi_0 = y_1 + \frac{L}{2} + RS \end{aligned}\right\} \tag{24}$$

Furthermore, because in the $-t_{o1}$ to 0 integration limits the minimum value of $\Omega t$ is around 0.04 (the blade has a high span to arc ratio; usually it can reach 16), thus it is possible to let $\cos\Omega\tau = 1 - \frac{\Omega^2\tau^2}{2}$, $\sin\Omega\tau = \Omega\tau$. It is also possible to omit $U_\infty\cos\Phi$ and all the higher terms than $\tau^2$ to obtain

$$a = \sqrt{(x_1 - \xi_1 + U_1\tau)^2 + (y_1 - \eta_1)^2 + (z - \zeta)^2} \tag{25}$$

$$Q_\infty = U_1(x_1 - \xi_1 + U_1\tau) \tag{26}$$

$$U_1 = \rho\Omega + U_\infty\sin\Phi \tag{27}$$

Under these assumptions, it is possible to express $\tau$ explicitly with t. Its method is similar to that of the wing. Finally, we get

$$V_s^{(2)} = -\frac{S}{4}\,\frac{1}{4\pi\rho_\infty}\,\oint\!\!\!\!\!\!\ast\int_{-1}^{1}\oint\!\!\!\!\!\!\ast\int_{-1}^{1} d\bar{\xi}_1 d\bar{\eta}_1 \sum_{n=0}^{\infty}\Delta p_n(\bar{\xi}_1, \bar{\eta}_1)e^{in\omega}\lim_{z\to 0}\frac{\partial^2}{\partial z^2} \tag{28}$$

$$\times\int_{-t_{01}}^{0}\exp\left\{i\,\frac{n\Omega}{\beta^2}\left[t + \frac{(x_1 - \xi_1)U_1}{a_\infty^2} - \frac{R}{a_\infty}\right]\right\}\frac{dt}{R}$$

where $\beta^2 = 1 - M^2$, $M = U_1/a_\infty$

$$R = \sqrt{(x_1 - \xi_1 + U_1 t)^2 + \beta^2(y_1 - \eta_1)^2 + \beta^2(z - \zeta)^2} \tag{29}$$

The symbol $\oint\!\!\!\!\!\!\ast\int$ represents the need to obtain the Hadamard principal value of the double integral because the operations of calculating the derivatives and limits are moved inside the double integral sign. Let us write the inner integral as J and make $x_1 - \xi_1 + U_1 t = \lambda$,

$$J = \frac{\exp\left[-\frac{in\Omega(x_1 - \xi_1)}{U_1}\right]}{U_1}\lim_{z\to 0}\frac{\partial^2}{\partial z^2} \tag{30}$$

$$\times\int_{x_1 - \xi_1 - U_1 t_{01}}^{x_1 - \xi_1}\frac{\exp\left\{\frac{in\Omega}{\beta^2 U_1}\left[\lambda - M\sqrt{\lambda^2 + \beta^2(y_1 - \eta_1)^2 + \beta^2 z^2}\right]\right\}}{\sqrt{\lambda^2 + \beta^2(y_1 - \eta_1)^2 + \beta^2 z^2}}d\lambda$$

The form of integral s in (30) has been solved in [4]. The integration limits are from $-\infty$ to $x_o$. Using equation (D8) in that paper and making

$$\int_{x_1 - \xi_1 - U_1 t_{01}}^{x_1 - \xi_1} f(\lambda)d\lambda = \int_{-\infty}^{x_1 - \xi_1} f(\lambda)d\lambda - \int_{-\infty}^{x_1 - \xi_1 - U_1 t_{01}} f(\lambda)d\lambda \tag{31}$$

this corresponds to the tangential motion along the blade added or subtracted by a term which is the wake from $-\infty$ to the rear fringe of the blade. In addition, by noticing that the terms irrelevant to the upper limit of the integral in (D8) are cancelled in the subtraction we get

$$V_z^{(m)}(r,\ \psi_0,\ \varphi)=\frac{S}{4}\ \frac{1}{4\pi\rho_\infty}\ \oint_{-1}^{1}\oint_{-1}^{1}d\bar{\xi}_1 d\bar{\eta}_1$$

$$\times\sum_{n=0}^{\infty}\Delta p_n(\bar{\xi}_1,\ \bar{\eta}_1)\ \frac{\exp\{in[\varphi-\Omega(x_1-\xi_1)/U_1]\}}{U_1(y_1-\eta_1)^2}$$

$$\times\left\{\frac{x_0\exp\left[\frac{in\Omega}{\beta^2U_1}(x_0-M\sqrt{x_0^2+\beta^2(y_1-\eta_1)^2})\right]}{\sqrt{x_0^2+\beta^2(y_1-\eta_1)^2}}-iz_1\right.\qquad(32)$$

$$\left.\times\int_0^{\frac{x_0-M\sqrt{x_0^2+\beta^2(y_1-\eta_1)^2}}{\beta^2|y_1-\eta_1|}}\frac{\lambda}{\sqrt{1+\lambda^2}}e^{in\varphi_1\lambda}d\lambda\right\}\Bigg|_{x_0=x_1-\xi_1-U_1t_{01}}^{x_0=x_1-\xi_1}$$

Therefore,

$$V_n(r,\ \psi_0,\ \varphi)=\frac{S}{4}\cdot\frac{1}{4\pi\rho_\infty}\int_{-1}^{1}\int_{-1}^{1}d\bar{\xi}_1 d\bar{\eta}_1\sum_{n=0}^{\infty}\Delta p_n(\bar{\xi}_1,\ \bar{\eta}_1)$$

$$\times\left(\sum_{m=2}^{MM}e^{in\varphi_m}\int_{-\infty}^{\varphi/\Omega}AGUdt+\int_{-\infty,\,(m=1)}^{\frac{\varphi}{\Omega}-t_{01}}AGUdt\right)+\frac{S}{4}\ \frac{1}{4\pi\rho_\infty}\ \oint_{-1}^{1}\oint_{-1}^{1}d\bar{\xi}_1 d\bar{\eta}_1$$

$$\times\sum_{n=0}^{\infty}\Delta p_n(\bar{\xi}_1,\ \bar{\eta}_1)\ \frac{\exp\{in[\varphi-\Omega(x_1-\xi_1)/U_1]\}}{U_1(y_1-\eta_1)^2}$$

$$\times\left\{\frac{x_0\exp\left[\frac{in\Omega}{U_1\beta^2}(x_0-M\sqrt{x_0^2+\beta^2(y_1-\eta_1)^2})\right]}{\sqrt{x_0^2+\beta^2(y_1-\eta_1)^2}}-iz_1\right.\qquad(33)$$

$$\left.\times\int_0^{\frac{x_0-M\sqrt{x_0^2+\beta^2(y_1-\eta_1)^2}}{\beta^2|y_1-\eta_1|}}\frac{\lambda}{\sqrt{1+\lambda^2}}e^{in\varphi_1\lambda}d\lambda\right\}\Bigg|_{x_0=x_1-\xi_1-U_1t_{01}}^{x_0=x_1-\xi_1}$$

where

$$AGU=\frac{e^{i\pi\sigma'}}{\alpha^3(w^2+be^2)^{1/2}}\left[\frac{be+QA\cdot bc/(bd\cdot\alpha)}{bd}+\frac{QA\cdot bf+be\cdot\alpha\sqrt{bd}}{bd}\right.$$
$$\left.\times\frac{\pi\Omega}{a_\infty}+\frac{QA\cdot\zeta}{\sqrt{bd}}\left(\frac{\pi\Omega}{a_\infty}\right)^2\right] \qquad (34)$$
$$z_1=\pi\Omega|y_1-\eta_1|/U_1$$

## IV. METHOD OF CALCULATION

Due to the simplicity of the blade surface, a series method can be used which has a lower demand on the memory of the computer. Let

$$\Delta p_n(\bar{\xi}_1,\ \bar{\eta}_1)=\sqrt{\frac{1-\bar{\xi}_1}{1+\bar{\xi}_1}}\sqrt{1-\bar{\eta}_1^2}\sum_{p=1}^{\infty}\sum_{q=1}^{\infty}a_{n,p,q}\bar{\eta}_1^{q-1}gA_p(\bar{\xi}_1) \qquad (35)$$

where $$gA_1=1,\quad gA_2=\sqrt{1+\bar{\xi}_1^2},\quad gA_3=-\frac{1}{2}\bar{\xi}_1\sqrt{1+\bar{\xi}_1^2}\ \cdots \qquad (36)$$

After the substitution of (33) and undergoing a dimensionless process, a set of linear algebraic eauations regarding $a_{n,p,q}$ is obtained. In the coefficient matrix, the part containing the singularity is obtained using the method described in [4]. The finite integral in that equation can be approximated by (21) in [4]. But the calculation involves complex numbers. In this case the complex expression of a Fourier series to replace (18)

$$\Delta p=\sum_{n=0}^{\infty}\frac{1}{2}\left[(\Delta p_{n,1}-i\Delta p_{n,2})e^{in(\Omega' t+\hat{\varphi}_{m'})}+(\Delta p_{n,1}+i\Delta p_{n,2})e^{-in(\Omega' t+\hat{\varphi}_{m'})}\right] \qquad (37)$$

The calculation has to be carried out only with respect to the term corresponding to $e^{in(\Omega' t+\hat{\varphi}_{m'})}$. This is because the $V_z^{(3)}$ value obtained from the calculation of the other term must be a complex conjugate. Thus, if a certain order is discussed, then we get

$$V_n=(a+ib)\frac{1}{2}(\Delta p_{n,1}-i\Delta p_{n,2})+(a-ib)\frac{1}{2}(\Delta p_{n,1}+i\Delta p_{n,2})$$
$$=a\,\Delta p_{n,1}+b\Delta p_{n,2} \qquad (38)$$

where a and b represent the real and imaginary parts of the singularity portion respectively. Therefore, only by using the $e^{in(\Omega' t+\hat{\varphi}_{m'})}$ term, the real part calculated corresponds to the cosine component and the imagnary part corresponds to the sine component.

Equation (34) is a non-singular portion which is a continuous function. However, its calculation is very difficult because:

Firstly, since for the factors containing $e^{in\Omega\tau}$ $\Omega$ reaches about 20, therefore, the inner integral is a large parameter oscillating type of integral. When n increase, the value of $n\Omega$ increases rapidly which makes the number of integral knot point to increase quickly. The number of integrals also increases rapidly which makes it impossible to calculate higher order load in practice. In order to solve this problem, a simple function is used as an extrapolated function for the function to be integrated at n = 0 to obtain the extrapolation coefficient. Finally, in the extrapolation region the integral is preciously obtained by using the factor which is the product of three sample functions times $e^{in\Omega\tau}$ . This method makes it relevant between the calculation of the function value and load order n. It is then possible to obtain the highest order of load without increasing the computer time.

Secondly, the function to be integrated has very strong peak values at $m = 1$, $y = \eta$, $t = t_{01}$ When $m \neq 1$ it also has a strong peak but the position is hard to determine. In order to ensure that the calculated value is not covered by errors, we divided into subregions between [-1, 1] for the integral in the span and used $y = \eta$ as one end of an interval. Then, Gauss-LeChardin model is used to get the solution.

In compiling the program, it is necessary to minimize the work amount. If the 8th order load on the lift surface of a four blade system is to be determined, the number of integrals can reach over 100,000. In reality, it is possible to eliminate the number of arc and span series from the number of integrals and to eliminate the load order number based on the extrapolation method mentioned above, the number of single intergrals can be reduced to about 5000.

This method can also be solved using a grid method.

The azimuth angle $\phi$ is to provide convenience for Fourier analysis. After performing Fourier analysis on both the matrix and $V_z$, we can get

$$[V_z]_{m,y,z} = [K]_{m,y,z,n,p,q}[a]_{n,p,q} \qquad (39)$$

Here the elastic flapping motion of the blade is taken into consideration. $V_z$ must be solved from the differential equation in the dynamics of the elastic flapping of the blade. Thus, (39) and this equation are coupled as frequency-state for a solution.

## V. SIMPLE EXAMPLE

The original data of this example is taken from [5] Table 15 which represents the flight test of the American H-34 helicopter. Because of the inability to obtain the necessary funding, only the Planto-Glowatt corrections for incompressible working conditions are computed. The number of calculation point was also minimized. It is carried out on the slowest model 121 computer available in the country. Only four azimuth angles were taken (therefore, only first order harmonic analysis was made on the load). As for the lift line theory, in order to reduce the work load for the computer, we increased the length of the portion of blade without any wing shape. Thus, the load at the root of the blade has a higher error. The results are shown in Figure 4.

Based on the comparison between theory and experiment, the zeroth order total lift and distribution coincide very well with experimental results. Under the conditions that the number of azimuth angles is few and the calculation points are coarse, the first order load obtained agrees very well with the experimental results.

The major problers in this paper were guided by Professor Low Shichuin of Northwest Industrial University.

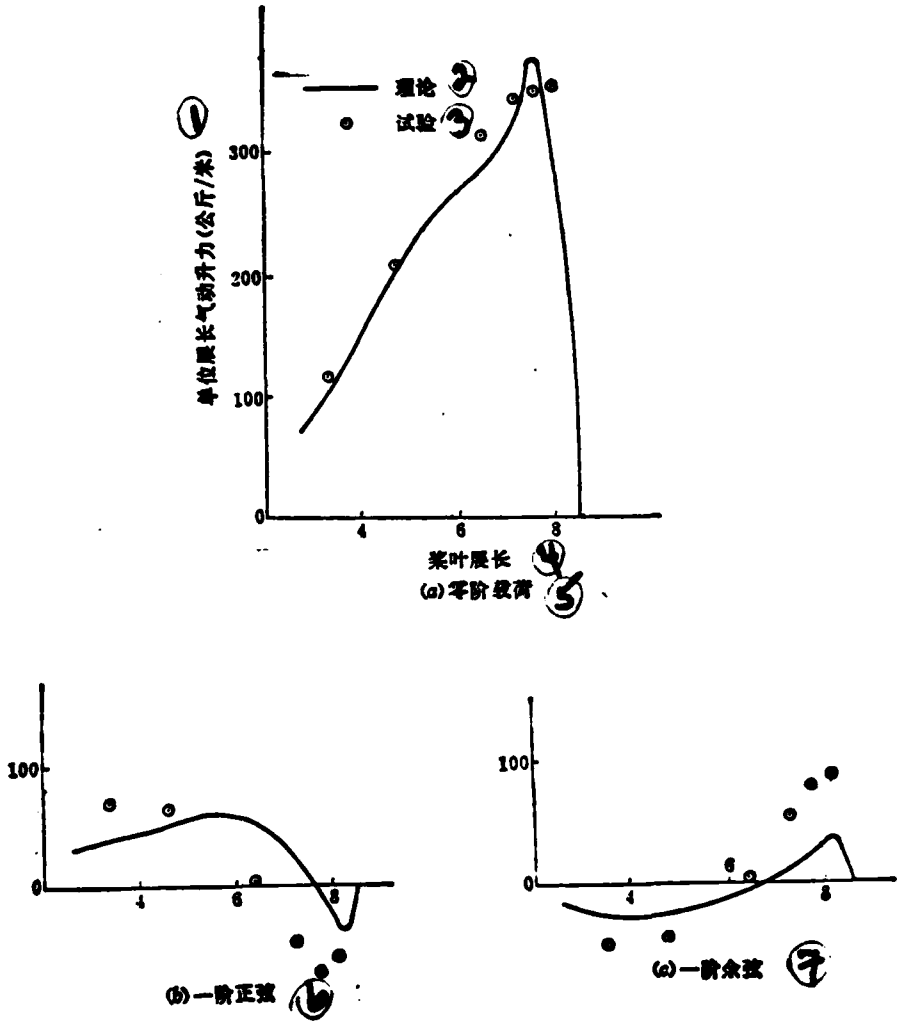


Figure 4. The comparison of theory result with measured in flight

1--aerodynamic lift per unit span (kg/m); 2--theory; 3--experimental; 4--blade span; 5--(a) zeroth order load; 6--(b) first order sine; 7--first order cosine

REFERENCES


[1] J. J. Costes., Calcul des Forces Aérodynamiques Instationnaires sur les Pales d'un Rotor d'hélicoptére. La Recherche Aérospatiale 1972. 91-106.

[2] Th. Van Holten., The Computation of Aerodynamic Loads on Helicopter Blades in Forward Flight, Using the Method of the Acceleration Potencial. Technische Hogeschool Deleft. Rapport VTH-189.

[3] Watkins, C. E., Runyan. H. H., and Woolstan. D. S., On the Kernel Function of Integral Equation Relating the Lift and Downwash Distribution of Oscillatings Finite Wings in Subsonic Flow. NACA Rep. 1234. 1955.

[4] Watkins. C. E., Runyan. H. L., and Cuningham. H. J., A Systematic Kernel Fuation Procedure for Determing Aerodynamic Forces on Oscillating or Steady Finite Wings at Subsonic Speeds. NASA. R-48. 1959.

[5] Scheiman. J., A Tabulation of Helicopter Rotor-Blade Differential Pressures, Stresses and Motions as Measured in Flight. NASA TM X-952. 1964.


# STUDY ON PRESSURE DISTRIBUTION ON ROTOR BLADES WITH THREE-DIMENSIONAL NONSTEADY THEORY OF COMPRESSIBLE FLUID


*Li Zhenhao and Ruan Tianen*

*(Jiangxi Aeronautical Society)*



## Abstract

A calculation of pressure distribution on rotor blades with three-dimensional nonsteady theory of compressible fluid is presented in the case of continuous wake-surface and forward motion of a helicopter at a constant speed. An acceleration potential equation is derived. A fundamental solution of the pressure doublet in an arbitrary motion is given. In order to satisfy the wake condition it is assumed that the pressure doublets move along the wake surface instead of along the actual tracks of blades. By adding the moving pressure doublets, an integral equation of the three-dimensional nonsteady compressible fluid with superior singularity is obtained when the blades are in complex motion. The significant effect of compressibility on the higher harmonic pressures is shown in this equation. The kernel function for the integral equation is divided into two parts, one with superior singularity and a continuous function with a strong peak. For the former the Hadamard principal value can be determined as for a wing. With the aid of a proper spline function procedure the function $e^{ia\sigma'}$ is separated from the function, hence it becomes possible to calculate the higher harmonic pressures. A simple typical example is completed on a small computer to justify the equation and the method.

# APPLICATION OF KALMAN FILTERING TECHNIQUE TO AERODYNAMIC DERIVATIVES FOR A HELICOPTER

(Flight Test Research Institute) Yang Songshan

ABSTRACT

The major object of this paper is to introduce a method to obtain aerodynamic derivatives of helicopters using low pass filtering, Kalman filtering and least square techniques. The characteristics of this method are the effect of high frequency component of the rotor is minimized by low pass filtering, the simultaneous acquisiton of the measuring noise and duration noise during data acquisition followed by Kalman filtering to reduce the helicopter noise level in the experimental data, and finally the aerodynamic derivatives of the helicopter are obtained using the least square method. In order to increase the accuracy of Kalman filtering, the least square method is used to obtain aerodynamic derivatives of the helicopter from experimental data to be used as the initial derivatives in Kalman filtering. The calculated results indicate that this method can significantly reduce the noise contained in the experimental data which cuts 70% of the error. The computation work load is far less than taht of maximum similarity method.

SYMBOLS

$V_x, V_y, V_z$--velocity components along x,y,z axis, respectively.
$\omega_x, \omega_y, \omega_z$--angular velocity components along x,y,z axis, respectively.
$a_o, a_1, b_1$--coning angle, reverse angle and incline angle of the rotor respectively
$\phi_7$--total distance of the rotor
$\phi_{wj}$--blade distance of the rear rotor
$\chi$--longitudinal incline angle of automatic incliner
$\eta$--transverse incline angle of automatic incliner
$\theta$--angle of elevat-on and depression
$\gamma$--angle of inclination

F, D--represent stability derivative matrix and control derivative matrix, respectively

w, v--represent duration noise and measurement noise, respectively.

$\Delta t$--sampling interval

E[X]--mathematical expectation of X

$X^T$--transformation matrix of X

$X^{-1}$--inverse matrix of X

$\hat{x}$ --estimated value of X

I--unit matrix

---

received in May 1981

## 1. INTRODUCTION

Any object has its special characteristics. Similar to other flying vehicles, a helicopter has its own characteristics and a range of conditions for best performance. A helicopter may have one or two rotors and very high degrees of freedom in motion. The experimental data also contain higher levels of noise. Under ordinary conditions, the longitudinal long period is basically unstable. These problems brought a certain degree of difficulty in the processing of experimental data. Some of the methods are applicable to fixed wing aircraft but cannot be used for helicopters. Since 1970, the Kalman filter technique and the maximum similarity method have been used to process helicopter data in other countries.

In this paper, through low pass filtering and Kalman filtering, the noise contained in the data is minimized. Finally, the aerodynamic derivatives of the helicopter are extracted accurately using the least square method. In order to achieve the highest degree of accuracy possible, the initial derivatives during Kalman filtering were obtained by directly applying the least square method to the original experimental data. The calculated results show that accuracy has been significantly increased and the errors of main parameters were reduced by 70%. As compared to the method involving the use of least square method based on data obtained from Kalman filtering reported in [1], a low pass filtering loop was added. The initial

derivatives of Kalman filtering were obtained from direct application of least square to the experimental data instead of engineering projections. Therefore, the accuracy is higher than those of the least square method and the least square method using data based on Kalman filtering as described in [1]. This method requires far less work load in computation as compared to the maximum similarity method and has all the advantages of the above methods. The high accuracy in calculation and the simplicity in computation allows the automatic processing of data as well as manual computation.

## II. EQUATION OF MOTIONS OF THE HELICOPTER

In order to describe the motion of a helicopter, at least six degrees of freedom are required. For a single rotor helicopter, it can be described based on a nine degree of freedom model.

The following is to establish the nine degree of freedom equations for a single rotor helicopter. For ease of derivation, let us assume:

(1) the body of the helicopter is an absolute rigid body which has six degrees of freedom;

(2) the rotor of the helicopter has three degrees of freedom, $a_o$, $a_1$, $b_1$;

(3) the helicopter has a plane of symmetry, i.e., longitudinal plane.

Using the body axis as the reference coordinate system, the origin of the coordinate system is located at the center of gravity. The x-axis points forward, y-axis upward and z-axis toward the right. Based on the force and torque balancing principles, the following increment function can oe written

$$\Delta \dot{V}_x = \frac{\partial X}{\partial V_x}\Delta V_x + \frac{\partial X}{\partial V_y}\Delta V_y + \frac{\partial X}{\partial V_z}\Delta V_z + \frac{\partial X}{\partial \omega_x}\Delta \omega_x + \frac{\partial X}{\partial \omega_y}\Delta \omega_y + \frac{\partial X}{\partial \omega_z}\Delta \omega_z + \frac{\partial X}{\partial \vartheta}\Delta \vartheta$$
$$+ \frac{\partial X}{\partial Y}\Delta Y + \frac{\partial X}{\partial a_0}\Delta a_0 + \frac{\partial X}{\partial \dot{a}_0}\Delta \dot{a}_0 + \frac{\partial X}{\partial a_1}\Delta a_1 + \frac{\partial X}{\partial \dot{a}_1}\Delta \dot{a}_1 + \frac{\partial X}{\partial b_1}\Delta b_1$$
$$+ \frac{\partial X}{\partial \dot{b}_1}\Delta \dot{b}_1 + \frac{\partial X}{\partial \phi_7}\Delta \phi_7 + \frac{\partial X}{\partial \phi_{m1}}\Delta \phi_{m1} + \frac{\partial X}{\partial X}\Delta X + \frac{\partial X}{\partial \eta}\Delta \eta + \frac{\partial X}{\partial \psi}\Delta \psi + w_x$$

$$\Delta\dot{V}_y = \frac{\partial Y}{\partial V_x}\Delta V_x + \frac{\partial Y}{\partial V_y}\Delta V_y + \cdots + w_{\dot{V}_y}$$

$$\Delta\dot{V}_z = \frac{\partial Z}{\partial V_x}\Delta V_x + \frac{\partial Z}{\partial V_y}\Delta V_y + \cdots + w_{\dot{V}_z}$$

$$\Delta\dot{\omega}_x = \frac{\partial M_x}{\partial V_x}\Delta V_x + \frac{\partial M_x}{\partial V_y}\Delta V_y + \cdots + w_{\dot{\omega}_x}$$

$$\Delta\dot{\omega}_y = \frac{\partial M_y}{\partial V_x}\Delta V_x + \frac{\partial M_y}{\partial V_y}\Delta V_y + \cdots + w_{\dot{\omega}_y}$$

$$\Delta\dot{\omega}_z = \frac{\partial M_z}{\partial V_x}\Delta V_x + \frac{\partial M_z}{\partial V_y}\Delta V_y + \cdots + w_{\dot{\omega}_z}$$

$$\dot{a}_0 = \frac{\partial \dot{a}_0}{\partial V_x}\Delta V_x + \frac{\partial \dot{a}_0}{\partial V_y}\Delta V_y + \cdots + w_{\dot{a}_0}$$

$$\dot{a}_1 = \frac{\partial \dot{a}_1}{\partial V_x}\Delta V_x + \frac{\partial \dot{a}_1}{\partial V_y}\Delta V_y + \cdots + w_{\dot{a}_1}$$

$$\dot{b}_1 = \frac{\partial \dot{b}_1}{\partial V_x}\Delta V_x + \frac{\partial \dot{b}_1}{\partial V_y}\Delta V_y + \cdots + w_{\dot{b}_1}$$

$$\Delta\dot{\vartheta} = \Delta\omega_y \sin\gamma + \Delta\omega_z \cos\gamma$$

$$\Delta\dot{\gamma} = \Delta\omega_x \cos\vartheta - \Delta\omega_y \sin\vartheta \cos\gamma + \Delta\omega_z \sin\vartheta \sin\gamma$$

$$\Delta\dot{\psi} = \Delta\omega_x \sin\vartheta + \Delta\omega_y \cos\vartheta \cos\gamma - \Delta\omega_z \cos\vartheta \sin\gamma$$

Rewriting the system in a matrix form, using X to represent the change in status and U as the control input, then we get

$$\Delta\dot{X} = F\cdot\Delta X + D\cdot\Delta U + w$$

The measurement equation can be expressed as

$$Z = H\cdot\Delta X + v$$

If all the parameters can be measured directly, then the measurement function is changed to

$$Z = \Delta X + v$$

## III. NOISE TREATMENT AND DERIVATIVE IDENTIFICATION IN THE EXPERIMENTAL DATA OF HELICOPTERS

The experimental data of a helicopter contain the following types of noise:

(1) measurement noise; including the instrumentation error on board and system error

(2) duration noise; all the factors influencing the equations of motion will cause duration noise. For example, gust disturbance, error in the simulation of the degree of freedom of the rotor, error

of nonlinear simulation and system error on board

(3) coordination error and other errors.

In order to improve the accuracy of the experimental results, the pilot was requested to operate precisely to minimize coordination error. If possible, the test was carried out under stable airflow conditions. In order to eliminate the effect of the high frequency portion of the rotor, a low pass filtering method was first used on the experimental data. Then it was followed by the Kalman fitting technique to minimize the onboard noise contained in the data. Finally, the aerodynamic deviatives were extracted from the data using the least square method. The processing procedures are as shown in Figure 1.

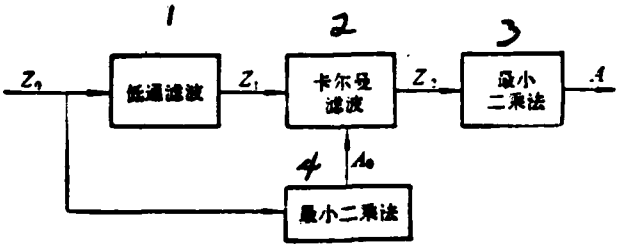


Figure 1. Functional diagram
1--low pass filtering; 2--Kalman filtering; 3--least square method; 4--least square method

In order to prevent the loss of meaningful effective signals during low pass filtering, the cutoff frequency of the low pass filter should be higher than the frequency of the effective signal. In addition, the choice of the cutoff frequency of the low pass filter should satisfy the sampling theory, i.e.,

$$f_c \leq \frac{1}{2\Delta t}$$

Let us assume that $Z_k$ is the input of the low pass filter and $X_k$ is the output, then the first order low pass filtering equation is

$$X_k = (1 - 2\pi f_c \Delta t) X_{k-1} + 2\pi f_c \Delta t Z_k$$

Assuming that the measurement noise and duration noise are both white noise, then the average square value of the measurement data should be the sum of the average square values of the effective signal and the noise signal. For a state variable X

$$\sigma_z^2=\sigma_v^2+\sigma_s^2=\frac{1}{n}\sum_{i=1}^{n}X^2$$

where $\sigma_v^2$--noise average square value

$\sigma_s^2$--effective signal average square value

In addition

$$\sigma_v^2=f_c R_A$$

$R_A$--intensity of noise

If the same signal passed through two filters of different cutoff frequencies, then the above equation can be written as

$$\sigma_{z_1}^2=f_1 R_A+\sigma_s^2$$

$$\sigma_{z_2}^2=f_2 R_A+\sigma_s^2$$

thus

$$R_A=\frac{\sigma_{z_2}^2-\sigma_{z_1}^2}{f_2-f_1}$$

The measurement noise contained in the experimental data after passing through a filter with a cutoff frequency $f_c$ is

$$R=R_A\cdot f_c=\frac{\sigma_{z_2}^2-\sigma_{z_1}^2}{f_2-f_1}f_c$$

Similarly, for duration noise, its intensity is

$$Q_A=\frac{\sigma_{z_2}^2-\sigma_{z_1}^2}{f_2-f_1}$$

the duration noise contained in the data is

$$Q=Q_A f_c=\frac{\sigma_{z_2}^2-\sigma_{z_1}^2}{f_2-f_1}f_c$$

where

$$\sigma_s^2=\frac{1}{n}\sum_{i=1}^{n}\dot{x}^2$$

Passing the filtered data from a filter with a cutoff frequency of $f_c$ into the Kalman filter, then the onboard noise contained in the data is reduced to a minimum.

Since we assumed that $\bar{v}$、$w$ are white noise and $v$、$w$ are independent, then for discrete condition

$$E[v \cdot w] = 0$$

$$E[w_k] = 0$$

$$E[w_k \cdot w_j^T] = Q_k \cdot \delta_{kj}, \quad \delta_{kj} = \begin{cases} 0 & k \neq j \\ 1 & k = j \end{cases}$$

$$E[v_k] = 0$$

$$E[v_k \cdot v_j^T] = R_k \delta_{kj}, \quad \delta_{kj} = \begin{cases} 0 & k \neq j \\ 1 & k = j \end{cases}$$

$$X_{k+1} = \phi_{k+1 \cdot k} X_k + \Gamma_{k+1 \cdot k} U_k + w_k$$

The initial state estimate and the coordination difference matrices are $\hat{X}_0$, $P_0$ respectively:

$$P_0 = E[(\hat{X}_0 - X_0)(\hat{X}_0 - X_0)^T]$$

The observation model is assumed to be

$$Z_k = H_k X_k + v_k$$

Based on the nonpartial minimum square difference estimation theory, we can derive

$$\hat{X}_{k+1/k} = \phi_{k+1 \cdot k} \hat{X}_{k/k} + \Gamma_{k+1 \cdot k} U_k$$

$$\phi_{k+1 \cdot k} = I + F \cdot \Delta t$$

$$\Gamma_{k+1 \cdot k} = D \cdot \Delta t$$

$$P_{k+1/k} = \phi_{k+1 \cdot k} P_{k/k} \phi_{k+1 \cdot k}^T + Q_k$$

$$K_{k+1} = P_{k+1/k} H_{k+1}^T [H_{k+1} P_{k+1/k} H_{k+1}^T + R_{k+1}]^{-1}$$

$$\hat{X}_{k+1/k+1} = \hat{X}_{k+1/k} + K_{k+1}[Z_{k+1} - H_{k+1} \hat{X}_{k+1/k}]$$

$$P_{k+1/k+1} = [I - K_{k+1} H_{k+1}] P_{k+1/k}$$

In order to prevent divergent phenomenon in the Kalman iteration operation, the initial derivatives of the model are obtained based on least square method using experimental data.

Because of passing through the low pass filter and Kalman filter, the noise contained in the data is reduced to a minimum. Then, the derivatives are obtained using the least square method which brings about more accurate results.

Based on the least square theory

$$\Sigma(\dot{x}-X)^2 = \text{minimum}$$

For a measurement equation of the following form

$$X_m A = \dot{x}_m$$

let us multiply both sides of the equal sign by the transformation matrix of $X_m$ to get

$$X_m^T X_m A = X_m^T \dot{x}_m$$

so

$$A = (X_m^T X_m)^{-1} X_m^T \dot{x}_m$$

## IV. USING KALMAN FILTERING METHOD TO OBTAIN THE LONGITUDINAL DERIVATIVES OF CHARACTERISTIC ROOT OF X-6 AIRCRAFT

In order to explore the validity and applicable range of the Kalman filtering method, that method was used to process the experimental results of longitudinal stability of the X-6 aircraft. The procedures are as shown in Figure 1.

The experimental results indicate that this method can reduce the errors of major parameters by over 70%. Figures 2 and 3 provide a comparison between results obtained using this method and the least square method. From the figures, it is clearly shown that the error band of the Kalman filtering method is significantly narrower.

## V. CONCLUSIONS

The method involving passing the original data through a low pass filter and Kalman filter then followed by using least square method to obtain the aerodynamic derivatives of helicopters has been proven to be a practical method. Because a low pass filter is added to the loop before the Kalman filter and because the original derivatives for Kalman filtering are obtained directly from experimental data using the least square method, the accuracy of the calculated results is higher than those of the least square method and the least square method using Kalman filtering of data as reported in [1]. The computation workload is also far less than that of maximum similarity method. This method

has the advantages of all the above methods.

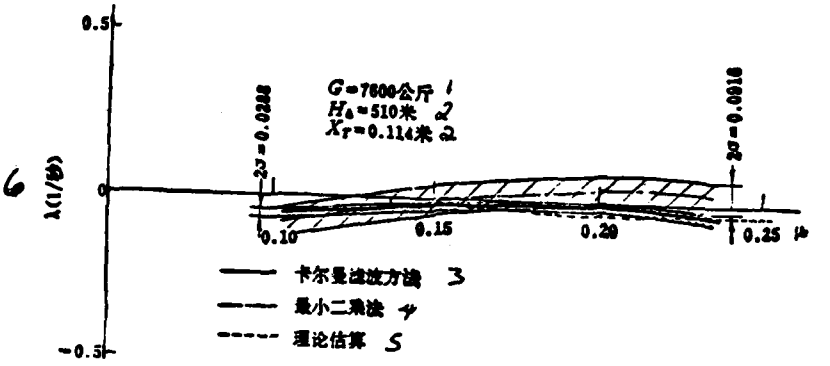


Fig.2 Phugoid Motion Daming Comparison of Least Square Estimator and Kalman Filter Esttimator

1--kilograms; 2--meters; 3--Kalman filtering; 4--least square; 5--theoretical estimation; 6--1/sec

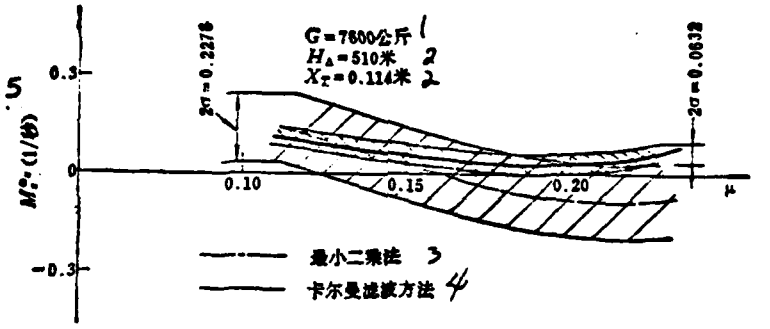


Fig.3 $M_u^{dot}$ Derivative Comparison of Least Square Estimator and Kalman Filter Estimator

1--kilograms; 2--meters; 3--least square method; 4--Kalman filtering method; 5--1/sec

REFERENCES

[1] Analytical study to define a helicopter stability derivative extraction method, vol I, Final Report, 1973-1-239 NASA Cr 132371.

[2] Optimal linear filtering lecture note, Changsa Industrial Institute, October 1973.

# APPLICATION OF KALMAN FILTERING TECHNIQUE TO AERODYNAMIC DERIVATIVES FOR A HELICOPTER

*Yang Songshan*
*(Flight Test Research Institute)*

Abstract

This paper describes a method for extracting the aerodynamic derivatives of a helicopter from flight data by means of low pass filtering, Kalman filtering and least square techniques. The method can be summaried as follows:

a) The high frequency effects from the rotor are eliminated by low pass filtering, and then measurement noise and process noise statistics are obtained.

b) By using Kalman filter, the random noise is minimized and the bias error is eliminated, but the derivatives are not identified yet.

c) The derivatives are identified from raw data by least square technique. They serve as initial values for Kalman filtering.

d) The final derivatives are extracted from Kalman filtering data by least square technique.

The method presented requires considerably less computation than the maximum likelihood method of reference [1]. It is more accurate than the least square technique and the least square technique with Kalman filtering data of reference [1]. This method cut down more than 70 percent of error *in comparison with the least square technique.*

# A FEASIBLE SIMPLIFIED METHOD FOR FINITE ELEMENT GRID OPTIMIZATION

Beijing Institute of Aeronautics and Astronautics, Gong Yaonan

## ABSTRACT

One of the major considerations in using the finite element method to carry out an analysis is how a computational result can be obtained with high accuracy and least computational effort for a specific problem. This is the optimum finite element discretization problem developed rapidly in the past 10 years. A lot of optimization criteria and corresponding procedures were proposed. The purpose of this paper is to present a new effective method for improving finite element discretization in order to avoid the difficulties and shortcomings of the presently available methods; i.e., to avoid the excessively huge computational time in the pure mathematical method and the difficulties in the batch mode method. Its program is simple to compile. It does not require special software for computation of counter lines and computer graphic display equipment. A feasible direction for the approximate optimization of discretization can be obtained from an error analysis. Furthermore, a one-dimensional search is used to obtain an approximate optimal discretization. The numerical example shows that the benefits are apparent by using the method described in this paper.

## I. INTRODUCTION

When using the finite element method, similar to any other approximation methods, we are concerned about whether it is possible to obtain accurate and convergent approximate solutions. Usually, two aspects can be used to promote the accuracy and convergence of the approximate solution [2]. p-convergence or h-convergence. Let us leave alone the fact that p-convergence is ineffective under many conditions, regardless of which of the two methods is used the net result is to increase the total number of degrees of freedom in the computational model which also means an increase in computational effort. Is it possible to maintain the number of characteristics of the elents unchanged and by

adjusting the grid to accomplish an optimal numerical solution when the above mentioned conditions? Or, in order to reach the accuracy required what is the minimum number of nodal points (number of degrees of freedom) increase necessary? Thus, a problem is laid in front of us which is the optimum finite element discretization or called grid optimization [1].

In the early stage of study an optimum finite element discretization, a mathematical planning method has been adopted. However, the computational effort of this procedure is so huge that the computational budget would not have been so high even if a uniformly dense grid was adopted to obtain the same degree of accuracy. Therefore, the researcher in this field had to look for other avenues to find a better (not optimum) finite element discretization method. In the recent 10 years, many optimization criteria and corresponding procedures have been proposed [3-18]. However, these methods, some of them have obvious characteristics of batch-mode operation and some of them require the graphic display equipment interfaced with the computer and the coordination of the special software which can compute and plot counter lines. The purpose of this paper is to present an effective method to improve the optimum finite element discretization problem. Under the condition of not increasing the total number of degrees of freedom, the accuracy of the solution can be raised.

## II. FEASIBLE METHOD SUGGESTED IN THIS PAPER

Let the nodal point coordinates of the finite element grid be a set of design variables to be determined which is represented by $\underline{x}$. The bar under x indicates that x is a vector.

---

received in April 1981

The constraints that $\underline{x}$ should satisfy are to assure the boundary shape of the continuous body and not to produce irregular elements. The optimization objective to be reached is to have the minimum (or close to minimum) total potential energy under an assigned load. If the initial value (nodal point coordinates of the initial grid) of the design variable $\underline{x}$ is $\underline{x}^{o}$. The components to change $\underline{x}^{o}$ are

$$\underline{x} = \underline{x}^0 + t\underline{d}$$

where $\underline{x}^0$ and $\underline{x}$ are two points in design space. The vector $\underline{d}$ represents the direction of motion when the nodal point coordinates moved from $\underline{x}^0$ to $\underline{x}$. t is the amplitude of the move. Our purpose is to find a procedure to locate a point $\underline{x}^*$ in the design space:

$$\underline{x}^* = \underline{x}^0 + t^*\underline{d}$$

which can make the total potential energy to reach a minimum or near minimum. For this the key step is to find a feasible direction $\underline{d}$ using a method as simple as possible. It is followed by a one-dimensional search to determine the step length $t^*$.

In order to determine the feasible direction $\underline{d}$, we have to consider the error estimation of piecewise approximation under one-dimensional conditions. Assuming f(r) is the distribution of a certain fluid function (e.g., stress energy density) and the Taylor series expansion at a point $r_i$ is

$$f(r) = f(r_i) + \sum_{p=1}^{n} \frac{(r - r_i)^p}{p!} f^{(p)}(r_i) + E(\eta)$$

where

$$E(\eta) = \frac{(r - r_{i+1})^{n+1}}{(n+1)!} f^{(n+1)}(\eta) \quad \eta \in (r_i,\ r)$$

is an extra term. Let us divide the one-dimensional region into N-1 subdivisions and each subdivision is approximated by a finite element. In order words, we are using N-1 finite elements to perform piece-wise approximation with respect to f(r) in a one-dimensional region. If the approximate polynomial of the element g(r) is of nth order, then the cutoff error of the ith element (its two nodal points coordinates are $r_i$ and $r_{i+1}$) is

$$E_i(\eta) = \frac{(r_{i+1} - r_i)^{n+1}}{(n+1)!} f^{(n+1)}(\eta_i) \qquad \eta_i \in (r_i,\ r_{i+1})$$

Therefore, different nodal point distribution will result in different local error distribution which in term causes different total error. In order to make local error distributed evenly, we should let

$$E_1(\eta) = E_2(\eta) = \cdots = E_{N-1}(\eta) = \text{constant}$$

where N is the total number of nodal points. Which means

$$(r_2 - r_1) \sqrt[n+1]{|f^{(n+1)}(\eta_1)|} = \cdots = (r_N - r_{N-1}) \sqrt[n+1]{|f^{(n+1)}(\eta_{N-1})|} = \text{constant}$$

or

$$r_{i+1} - r_i = \frac{\text{constant}}{\sqrt[k+1]{|f^{(k+1)}(\eta_i)|}} \qquad (1)$$

By adjusting the value of the constant, it is possible to make $r_1$ and $r_N$ fall on the two boundaries of the one-dimensional region. Furthermore, equation (1) can be rewritten as

$$r_{i+1} - r_i = \frac{\text{constant}}{\sqrt[l]{|f^{(l)}(\eta_i)|}} \qquad (2)$$

To determine the nodal point positions of the elements from equation (2), we will obtain a nonuniform local error distribution. Equation (1) is a special case of equation (2). By adjusting the values of k and l, it is possible to get the best error distribution.

The above discussion is for one-dimensional conditions. The same results can be applied to two-dimensional situations and the same good results can be obtained. Although the corresponding optimization criteria can be obtained from the estimation of error based on the Taylor series expansion in a two-dimensional situation, yet further simplification is needed because an ideal grid optimization method must be [8] matched with low cost computation and simple program design, otherwise the original objective of optimization is not accomplished. The extension of the conclusions for the one-dimensional case to a two-dimensional situation is a simplification procedure. The actual steps are in the following:

The displacement and stress energy nodal point values are calculated based on the original uniform grid $\underline{x}^0$. With respect to each original (both x and y directions) grid line, an extrapolated polynomial f(r) is used to approximate the stress energy distribution along the grid line:

$$f(r) = \sum_{i=1}^{N} \left[ \prod_{\substack{j=1 \\ j \neq i}}^{N} \frac{r - r_j}{r_i - r_j} \right] f(r_i)$$

where $f(r_i)$ is the value of stress energy at nodal point i on the grid-line. Then, based on the criteria given by equation (2), the new coordinates $r_i'$ of the nodal points (in the x or y direction) on the grid line are determined. After processing all the grid lines in both directions using the method described above, we obtain a new improved grid $\underline{x}$

which contains the coordinates in both x and y directions of every nodal point from

$$\underline{x}=\underline{x}^0+\underline{d}' \tag{4}$$

we get $\underline{d}'$. The feasible direction $\underline{d}$ can be obtained by unitize $\underline{d}'$.

$$\underline{d}=\frac{\underline{d}'}{\|\underline{d}'\|} \tag{5}$$

Sometimes it is necessary to make individual corrections for $\underline{d}$ thus created in order to avoid the formation of irregular elements in the new grid. When the mathematical planning method was used to optimize the grid, this correction was contained in the nonlinear constraint conditions. Since constraints are not used here, therefore, corrections may be needed. However, in general, only individual nodal points require occasional correction. In [15], a correction method was given which can serve as a good reference.

Whether the grid has been optimized can be evaluated from various angles depending upon the objective of optimization. If from the point of view of the entire system then discretization accomplishes optimization. The potential energy of the total system is a minimum. If our concern is focused on the local stress, then the calculation of stress should approach its accurate value as close as possible. In order to observe the feasibility of the method introduced in this paper, three examples involving numerical calculations are given as below.

## III. NUMERICAL EXAMPLES

As the first numerical example, let us study a square plate with loads concentrated on the four corners as shown in Figure 1. Due to symmetry, only a quarter of the plate is analyzed. Turcke [6] used triangular elements and Rosenbrock method to solve the optimum discretization problem for this plate. This paper adopted quadrilateral equal-parametric elements. The initial even grid is shown in Figure 1. Based on equation (2) and choosing k = l = 2, we obtained the optimized grid as shown in Figure 2. The results are shown in Table 1 where $\pi_p$ represents the total potential energy and $\bar{\pi}_p$ indicates the relative

value of the total potential energy using the $\pi_p$ obtained from Turcke's optimized triangular grid as the basis. SED represents the stress energy density and NDF represents the total number of effective degrees of freedom.

Turcke[6] this work ($\nu$=0.33) Carroll ($\nu$=0.0)[18] TABLE 1

| element | triangular | | quadrilateral | | quadrilateral | | |
|---|---|---|---|---|---|---|---|
| grid | optimized | even | optimized | even | optimized | even | even |
| $\bar{\pi}_p$ | 1.0 | 0.7601 | 1.3383 | 0.7339 | 1.5451 | 1.07 | 1.2919 |
| NDF | 40 | 40 | 40 | 40 | 40 | 840 | 4900 |
| SED | | 38.57 | 5377.46 | | | | |

From Table 1 we can see that after the optimization using the method presented in this paper the absolute value of the total potential energy can increase by 76%. This corresponds to an increase in the number of degrees of freedom from 40 to 4900. The benefit is significant.

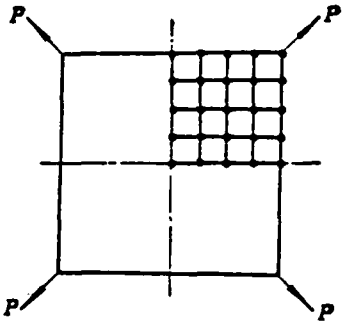


Fig.1 Square plate——initial even grid

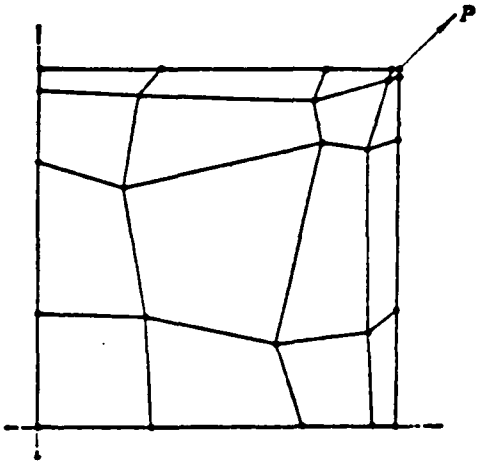


Fig.2 Square plate——optimized grid

As the second numerical example, let us study the simple supported beam as shown in Figure 3. The center of the span was concentrated with force. Turcke [17] had obtained an optimized grid based on the contour lines of the main stress. According to his report, the absolute value of the total potential energy of the optimized grid increased by 20% as compared with that before optimization. He believed that this is a significant improvement. In this paper, a four nodal point isoparametric element method was used to carry out a calculation with respect to the grids shown in Figures 3 and 4. In addition, an optimization was

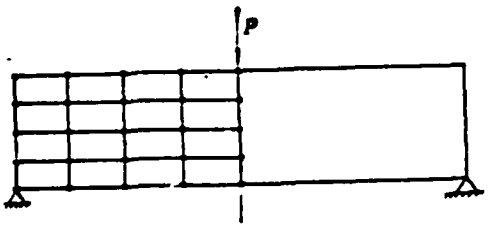


Fig.3 Simply-supported beam——initial even grid

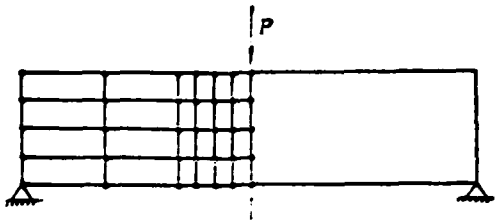


Fig.4 Simply-supported beam——refined grid

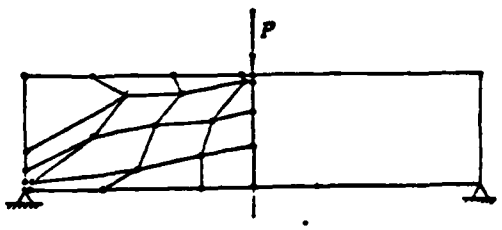


Fig. 5 Simply supported beam-optimal grid

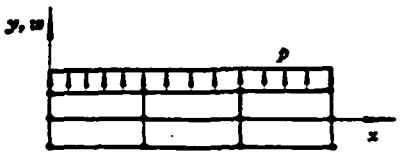


Fig.6 Cantilever beam——initial even grid

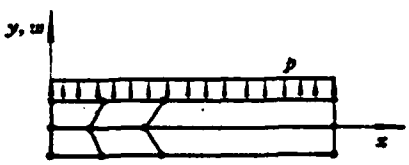


Fig.7 Cantilever beam——optimized grid

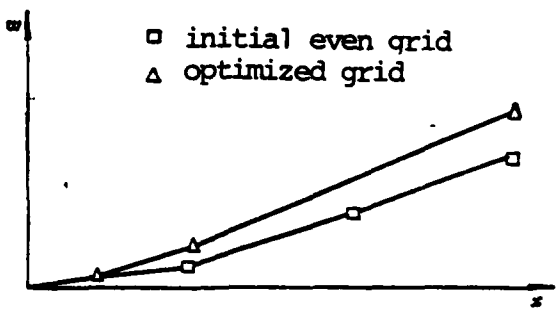


Fig.8 Cantilever beam——deflection curve

TABLE 2

| grid | even | density | optimized |
|---|---|---|---|
| $\bar{\pi}_p$ | 1.0 | 1.0478 | 1.1633 |
| SED a/b | 15.19/14.93 | 38.98/10.82 | 3649.99/20701.91 |
| NDF | 43 | 63 | 43 |

TABLE 3

| | this method | | Carroll | |
|---|---|---|---|---|
| grid | even | optimized | even | optimized |
| $\bar{\pi}_p$ | 1.0 | 1.46 | 1.0 | 1.46 |
| NDF | 12 | 12 | 12 | 12 |
| $\sigma_{max}$ | 3038.6 | 4960.9 | | |

performed based on equation (2) by choosing k = 2 and l = 0 with respect to the grid shown in Figure 3. The optimized grid is shown in Figure 5. The calculated results are shown in Table 2. In Table 2 the SED has two expressed values a/b where a represents the stress energy density at the point of concentrated load and b represents the stress energy density at the support. From Table 2, it is clear that the method presented in this paper has significant improvement with regard to either total system error or partial local error.

The two examples above are on concentrated load. The third numerical example is a cantilever beam under evenly distributed load. The initial grid is as shown in Figure 6. According to equation (2) and taking k = 2 and l = 0, an optimized grid is obtained as shown in Figure 7. The calculated results are shown in Table 3. The deflection curve is shown in Figure 8. (The numerical computation of the third example was done by comrade Ah Yejen).

## IV. CONCLUSIONS

The grid optimization method given in this paper is simpler and more economical. It does not matter whether it is a concentrated load or evenly distributed load condition, good results can always be obtained.

The computational time, including the entire optimization procedures, is merely $\frac{1}{10}\sim\frac{1}{5}$ of that of the evenly denser grid method of the same accuracy. This method was only explored with two dimensional balance problems. Whether it can be further extended to three dimensional problems is yet to be studied. Other problems such as vibration and stability are not yet dealt with.

REFERENCES


[1] Chiang Weichang "New development in finite element method", report in 1980 National Computational Mechanics Meeting, 1980.

[2] Tong, Pin and Rossettos, J. N., Finite-Element Method, The MIT Press, Massachusetts, U. S. A., 1978.

[3] McNeice, G. M. and Marcal, P. V., "Optimization of Finite Element Grids Based on Minimum Potential Energy", TR-7, Brown University, Providence, Rhode Island, 1971.

[4] Shephard, M. S., "Finite Element Grid Optimization-A Review", in Finite Element Grid Optimization, M. S. Shephard and R. H. Gallagher, eds., ASME special publication PVP-38, N. Y., 1979.

[5] Turcke, D. J. and Mc Neice, G. M., "A Variational Approach to Grid Optimization in the Finite Element Method", Conf. on Variational Methods in Engineering, Southampton University, Engiand, 1972.

[6] Turcke, D. J. and McNeice, G. M., "Guidelines for Selecting Finite Element Grids Base on Optimization Study", Int. J. of Computers and Structures, Vol. 4, 1974, pp499-519.

[7] Carroll, W. E. and Barker, R. M., "A Theorem for Optimum Finite Element Idealizations", Int. J. of Solids and Structures, Vol. 9, 1973.

[8] Turcke, D. J., "Finite Element Mesh Configurations Using Isoenergetics and Equalized Energy Levels", in Research in Computerized Structural Analysis and Synthesis, Harvey G. McComb, Jr., ed., NASA Conference Publication 2059, 1978, pp89-95.

[9] Carroll, W. E., "Ramifications of Optimum Idealization Geometry in Discrete Element Analysis", Proc. World Congress on Finite Elements in Structural Mechanics, Bournamouth, England, 1975.

[10] Melosh, R. J. and Marcal, P. V., "An Energy Basis for Mesh Refinement of Structural Continua", Int. J. num. Meth. Engng, Vol. 11, no. 7, 1977.

[11] Peano, A., Riccioni, R., Pasini, A. and Sardella, L., "Adaptive Approximation in Finite Element Structural Analysis", in Trends in Computerized Structural Analysis and Synthesis, A. K. Noor and H. G. McComb, Jr., eds., Pergamon Press, 1978, pp333-342.

[12] Oliveira, E. R. A., "Optimization of Finite Element Solutions", Proc. 3rd Conf. on Matrix Methods in Structural Mechanics, Wright-Patterson Air Force Base, Ohio, 1971.

[13] Szabo, B. A., Basu, P. K. and Rossow, M. P., "Adaptive Finite Element Analysis Based on P-Convergence", in Research in Computerized Structural Analysis and Synthesis, NASA Conference Publication 2059, 1978, pp43-50.

[14] Molinari, G. and Viviani, A., "Grid Iteration Method for Finite Element Grid Optimization", in Finite Element Grid Optimization, M. S. Shephard and R. H. Gallagher, eds., ASME special publication PVP-38, N. Y., 1979, pp51-59.

[15] Shephard, M. S., Gallagher, R. H. and Abel, J. F., "Experience with Interactive Computer Graphics for the Synthesis of Optimal Finite Element Meshes", in Finite Element Grid Optimization, M. S. Shephard and R. H. Gallagher, eds., ASME special publication PVP-38, N. Y., 1979, pp61-73.

[16] de Boor, C., "Good Approximation by Splines with Variable Knots", ISNM Vol. 21, Springer-Verlag, Berlin, 1974.

[17] Turcke, D. J., "Characteristics of Piecewise Approximations in Numerical Analysis", in Finite Element Grid Optimization, M. S. Shephard and R. H. Gallagher, eds., ASME special publication PVP-38, N. Y., 1979, pp15-21.

[18] Carroll, W. E., "On the Reformulation of the Finite Element Method", Int. J. of Computers and Structures, Vol. 8, no. 5, 1978, pp547-552.

# A FEASIBLE SIMPLIFIED METHOD FOR FINITE ELEMENT GRID OPTIMIZATION

*Gong Yaonan*

*(Beijing Institute of Aeronautics and Astronautics)*

Abstract

An important consideration encountered in the use of the finite element method is how a computational result can be obtained as accurate as possible with the least computation effort for a special problem, especially for a problem of singularity with the character of stress concentration. This is the problem of Optimum Finite Element Discretization developed during the recent decade. In this period a lot of optimization criteria and corresponding procedures were proposed. The purpose of the present paper is to suggest a new effective method for improving the finite element discretization which can avoid the difficulties and shortcomings encountered in a batch-mode operation and doesn't need the special software for computation of contour lines and computer graphic displays. After a relatively simple operation, the grid optimization can be performed by the aid of a feasible direction obtained via optimality criteria combined with the one-dimensional search techniques. The computational results of numerical examples presented show that in the best case from an even grid to an optimized grid a gain of the total potential energy was obtained, being equivalent to an increase in the number of degrees of freedom from 40 to 4900. It is obvious from tables and graphics presented that quite satisfactory results are obtainable, no matter whether the global or the local error is concerned.

# THE CRACK-FREE LIFE PREDICTION FOR STRUCTURAL JOINTS UNDER CONSTANT AMPLITUDE LOADS

Aircraft Strength Research Institute, Xue Jing Chuan and Yang Yugong

## ABSTRACT

This paper briefly describes the method to predict life for structural joints under constant amplitude loads using the stress severity factor concept and introduced the procedures to determine factors $\alpha$ and $\beta$ based on that concept. An approach dealing with the effect of scratch is derived by fitting the test data. Simultaneously, the reliability of this method has been verified through the fatigue test of over 100 riveted joints.

## INTRODUCTION

Structural joints can be seen almost in every part of the aircraft structure. How to determine the life of these structural joints is a problem of utmost concern for aircraft design personnel. This paper introduces a stress severity factor method to predict the life of jointed plate under axial loads based on the S-N curves of simple notch test samples (materials).

The fatigue characteristics of joints are mainly affected by the installation of the hole, fastener and the material and assembly method of the matching plates. In addition, the scratch between the fastener and the hole is also influencing its life. The stress severity factor is an indicator of fatigue quality which takes the above factors into consideration. The effect of scratch is considered through the correction from the S-N curve of the material. It should be pointed out that this paper is limiteded to a one-dimensional stress problem.

This paper has been reviewed by Chief Engineer Fong Chungyuch. The work was assisted by Associate Professor Yang Chingshon of Northwest Industrial University. Assistance also came from comrades of Shenyang

Aircraft Company and Hongan Aircraft Company. Sincere appreciation to those who assisted is expressed here.

## I. STRESS SEVERITY FACTOR [1]

Stress severity factor is a parameter which reflects the effect of the installation of the hole on the fastened plate as well as the materials and the assembly method of the fastener and the matching plate.

As shown in Figure 1, the maximum local stress along the edge of the hole is

$$\sigma_{max} = K_{jy}\frac{R}{dt}\theta + K_t\frac{P_p}{Wt}$$

the combined stress concentration factor is

$$K = \sigma_{max}/\sigma_{ot}$$

In order to indicate the effect of surface status and assembly type under fatigue load conditions, two coefficients α and β are introduced to the define stress severity factor as:

---

received in December 1980.

$$K_y = \frac{\alpha\beta}{\sigma_{ot}}\left(K_{jy}\frac{R}{dt}\theta + K_t\frac{P_p}{Wt}\right) \qquad (1)$$

where R--transfer load of the fastener
$P_p$--local side load
$K_t$--theoretical stress concentration coefficient
$K_{jy}$--compressive stress concentration coefficient
α--hole surface coefficient
β--hole filling coefficient
θ--compression distribution coefficient

In the elastic region, equation (1) can be rewritten as:

$$K_y = \alpha\beta[f_1(K_{jy}, \theta) + f_2(K_t)]$$

Therefore, $K_y$ is only affected by the structural form ($\alpha, \beta, \theta, K_{jy}, K_t$) and not influenced by the properties of the material and stress load. When the material and fastener enter the modern region, this is no longer true.

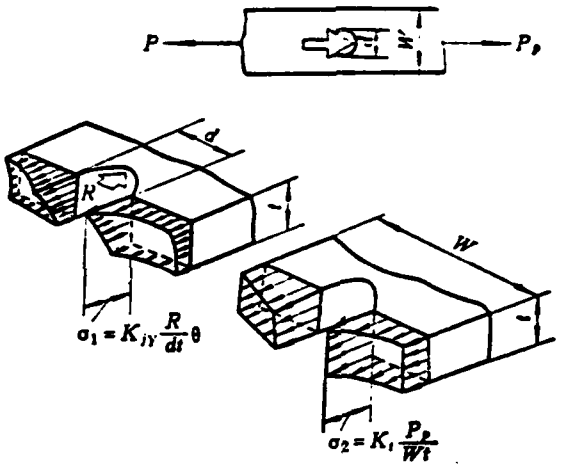


Fig.1 Stress distribution at the fastener hole

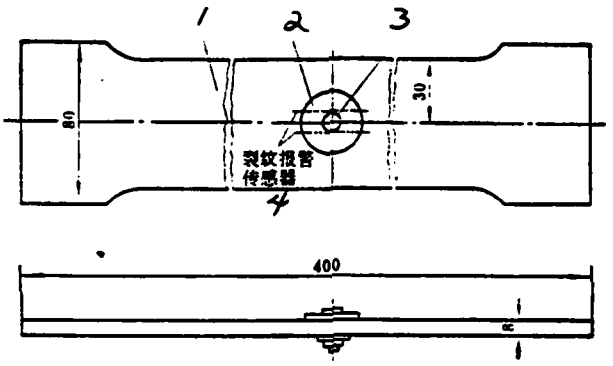


Fig.2 α and β specimens

1--plate; 2--washer; 3--screw head; 4--crack warning transducer

The $K_y\sigma_{gk}$ at stress concentration point in the structure approximately represents its life. Therefore, it is possible to obtain the desired uniform structural life by the proper design so that this value is as identical and as low as possible. In the prediction of structural life, $K_y$ corresponds to the theoretical stress concentration coefficient.

## II. α, β COEFFICIENTS

This paper does not wish to discuss the load distribution computation of joints. Therefore, the remaining major problem in the determination of stress severity factor is to determine α and β. On the basis of the stress severity factor concept, this paper proposes the following method to determine these coefficients:

1. Determination of α coefficient

Two samples with holes made of two different materials and identical geometric shape were used as the sample (see Figure 2). The theoretical stress concentration coefficient is $K_t$. One sample has a standard hinge hole, the other has a drilled hole. Let us assume for the hinge hole $\alpha = 1$. Based on equation (1), because $\beta = 1, R = 0, P_0/W = \sigma_{net}$, therefore,

$$K_{vj} = K_t$$

where $K_{yj}$ is the stress severity factor under the hinge hole condition. Similarly, the stress severity factor the drilled hole is

$$K_{vz} = \alpha K_t$$

Using a certain level of stress for the fatigue test of the drilled hole, its life is $N_a$. On the S-N curves of the standard hinge hole with various stress concentration coefficients, it is possible to find the theoretical stress concentration coefficient $K_{t1}$ which corresponds to the same level of stress and life as $N_a$:

$$K_{vz} = K_{t1} = \alpha K_t \qquad (2)$$
$$\alpha = K_{t1}/K_t$$

2. Determination of the β coefficient

The geometric shape of the specimen is identical to that with a hole. The only difference is that inside the hole there is a non-load conducting fastener. According to equation (1), the stress severity factor of a screwed specimen is

$$K_{vL} = \alpha\beta K_t$$

Using a certain stress level to conduct the fatigue test of a screwed specimen, its life is $N_\beta$. The theoretical stress concentration coefficient $K_{t2}$ under similar conditions in terms of stress level and life as $N_\beta$ can be found from the S-N curves of standard hinge hole of various stress concentration coefficients. Then

$$K_{vL} = \alpha\beta K_t = K_{t2}$$
$$\beta = K_{t2}/(\alpha K_t) \qquad (3)$$

The results are shown in Table 1.

Table 1

| | | α | | β |
|---|---|---|---|---|
| 1 铰孔 | 4 本研究 | 1 | | |
| | 5 文献[4] | 1 | | |
| 2 钻孔 | 6 本研究 | 1.074 | | |
| | 7 文献[4] | 1.1 | | |
| 3 螺接 | | | 8 本研究 | 0.86 |
| | | | 9 文献[4] | 0.75~0.9 |

1--hinge hole; 2--drilled hole; 3--screw connection; 4--this study; 5--reference [4]; 6--this study; 7--reference [4]; 8--this study; 9--reference [4]

## III. THE EFFECT OF SCRATCH [2]

Under fatigue load situation the fastener under load moves relative to the assembly hole to scratch the hole wall which reduces the fatigue life of the basic plate. Based on the experimental data of joints, we gradually obtained the relation between the S-N curves with correction for the affect of scratch and the S-N curves of materials with a notch by fitting the data:

$$\left.\begin{array}{ll} \text{high load} & \lg N_{jie} = \lg N_{qie} \\ \text{medium load} & \lg N_{jie} = 0.9446 \lg N_{qie} + 0.1109 \\ \text{low load} & \lg N_{jie} = 0.7686 \lg N_{qie} + 1.0217 \end{array}\right\} \qquad (4)$$

where $N_{jie}$ --life after correction for scratch

$N_{qie}$ --life of material with a notch

The above relation was obtained from the $S_{max}$-N curve corresponding to a stress ratio R. Based on this, it is possible to give the constant life curve of the joint with correction for the effect of scratch (see Figure 3).

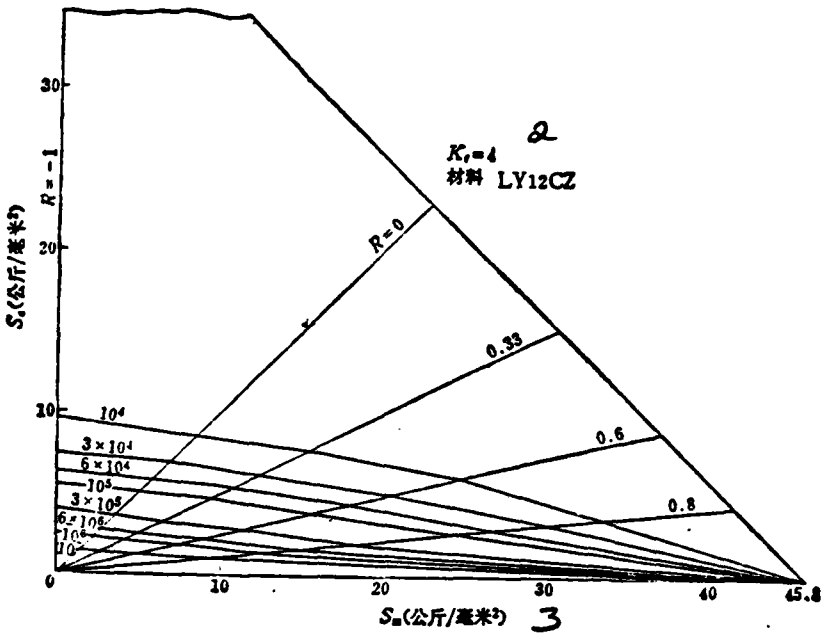


Fig.3 Constant life curve taking account of cratch

1--(kg/mm$^2$); 2--material; 3--(kg/mm$^2$)

## IV. PROCEDURES TO DETERMINE THE LIFE OF JOINTS UNDER CONSTANT AMPLITUDE LOAD USING THE STRESS SEVERITY FACTOR

1) Determine the internal force distribution of the joint under fatigue load in order to determine the transfer load of the fastener, the side load $P_p$ and the reference stress $\sigma_{ek}$, etc.

2) Base on the geometric shape and assembling form the joint to determine $\alpha$、$\beta$、$K_{tn}$、$K_t$、$\theta$, that the stress severity factor $K_y$ at all the stress concentrating points are known.

3) Determine the position of maximum product of stress severity factor and reference stress $K_y\sigma_{ek}$.

4) Base on the stress severity factor and reference stress at that point to locate the predicted life by looking into the corresponding life curves of identical material and equal stress concentrating coefficient with the affect of scratch taken into account.

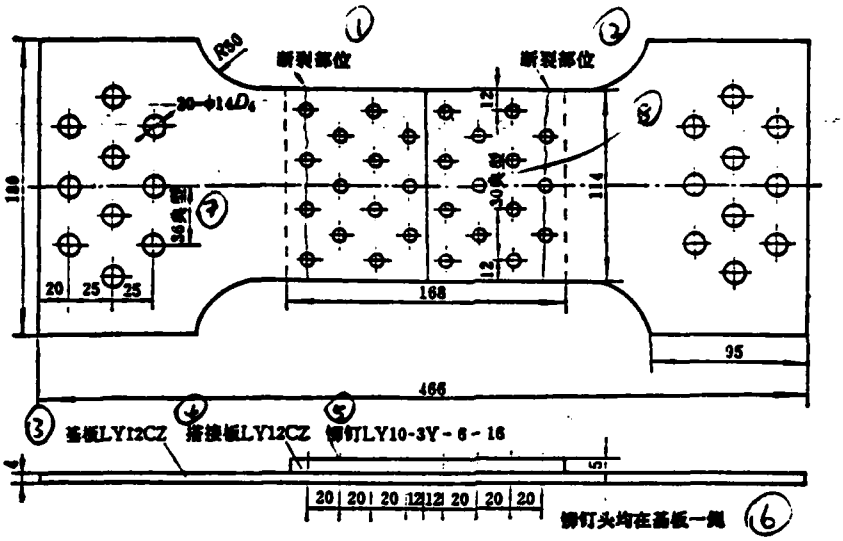


— Fig.4— Specimen 1

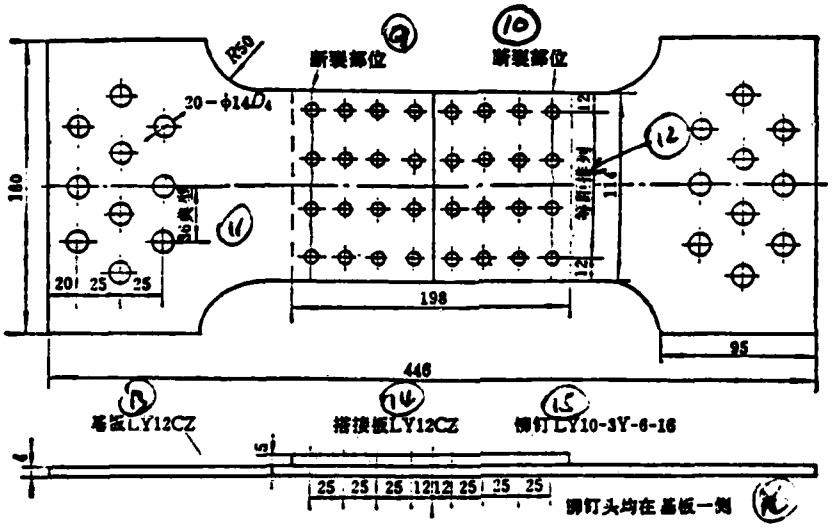


Fig.5 Specimen 2

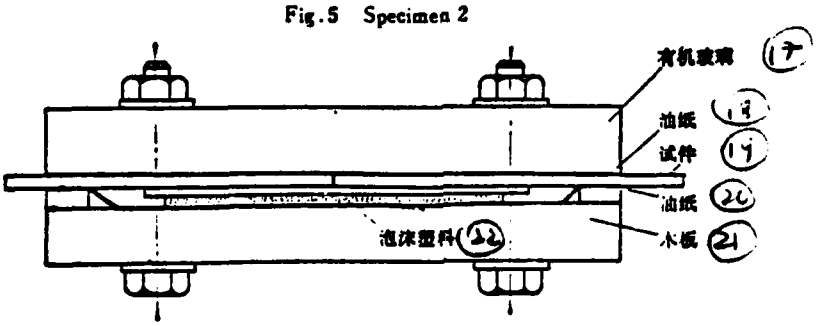


Fig.6 Set against bending

1,2—crack point; 3—base plate; 4—joint plate; 5—rivet; 6—rivet heads on same side of base plate; 7,8—typical; 9,10—crack point; 11—typical; 12—constant space array; 13—base plate; 14—joint plate; 15—rivet; 16—rivet heads all on same side of base plate; 17—organic glass; 18,20—oil paper; 19—specimen; 21—wooden plate 22—plastic foam.

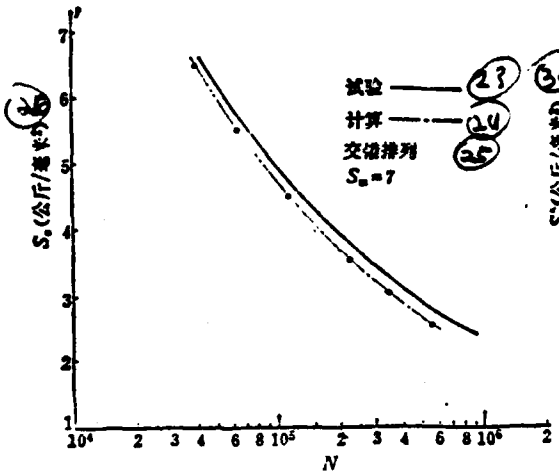


Fig.7 *S-N* curve

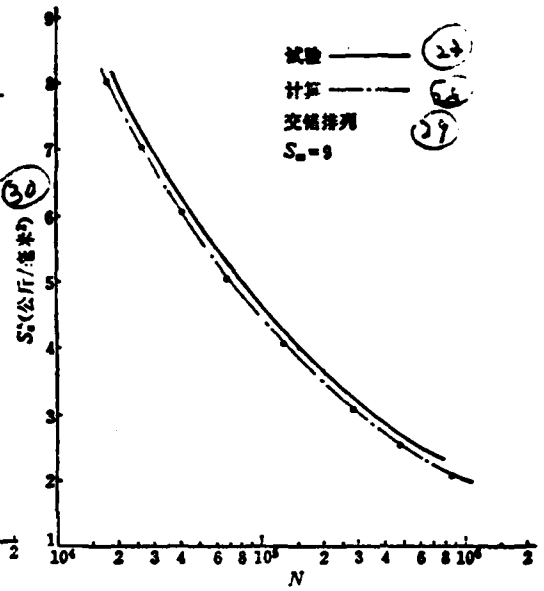


Fig.8 *S-N* curve

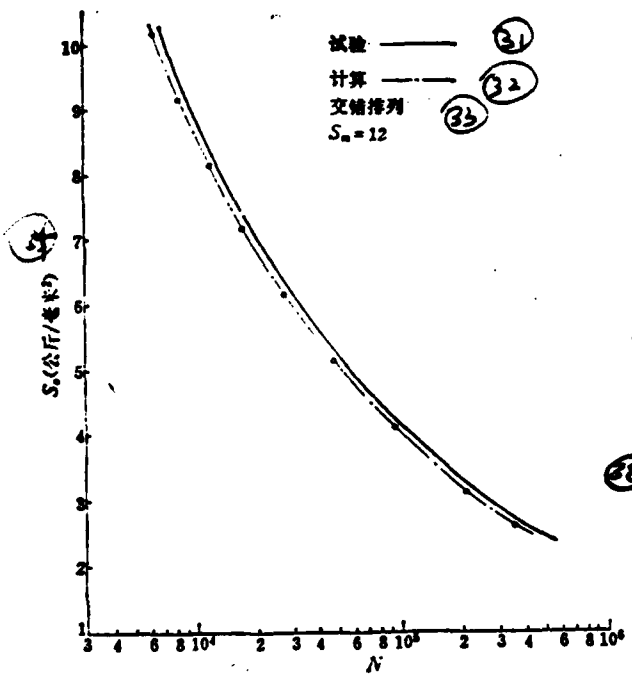


Fig.9 *S-N* curve

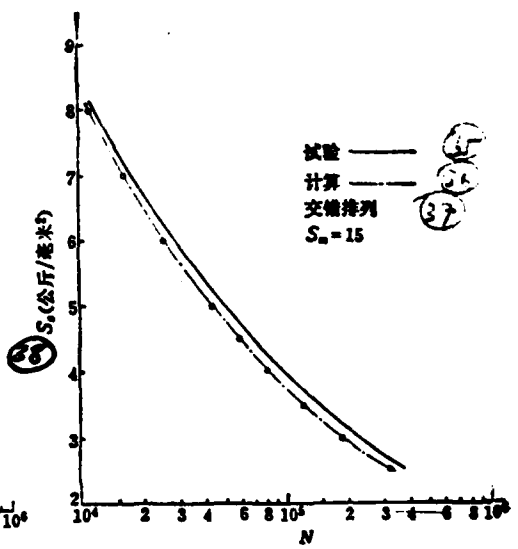


Fig.10 *S-N* curve

23,27,31,35--experimental; 24,28,32,36--calculated;
25,29,33,37--mis-matched array; 26,30,34,38--kg/mm$^2$

## V. JOINT FATIGUE TEST

1) The specimens have two forms, i.e., the rivets are aligned parallelly and mismatched. The basic plate thickness is 4 mm. The joint plate thickness is 5 mm. The plate material is LY12-CZ. The rivets have buried heads. The diameter is $\phi$ 6 and material is LY10. The fiber direction of the plate material is parallel to that of stress. The shapes of the specimen are shown in Figures 4 and 5.

2) The specimens are sandwiched. In order to effectively reduce the side vibration and bending of the specimen under load, a guidance plate was installed as shown in Figure 6.

3) The static destruction was shearing of rivets. Fatigue destruction all occurred at the first row of rivets on both sides. The experimental results are shown in the S-N curves in Figures 7-11.

## VI. PREDICTION OF JOINT LIFE [3,4]

### 1. Calculation parameters

Let us choose $\alpha = 1.1$; $\beta = 0.75$, $\theta = 1.4$ (considering the effect of rivet head).

$K_{jy}$ = 1.3 for parallel array
= 1.3 for mismatched array with four holes in a row
= 1.2 for mismatched array with three holes

$K_t$ for parallel array = 3.02 for the center hole
= 3.2 for the holes on the side
for mismatched array = 3.2 for 4 holes in a row
= 3.1 for 3 holes in a row

### 2. Conversion between $K_y$ and S

In the calculation of stress severity factor, corresponding to a fatigue load level ($P_{max}$ and $P_{min}$), the stress severity factors are $K_{ymax}$ and $K_{ymin}$ respectively. In the elastic region, $K_{ymax} = K_{ymin}$. If the fastener enters a molding stage, then the two are not equal.

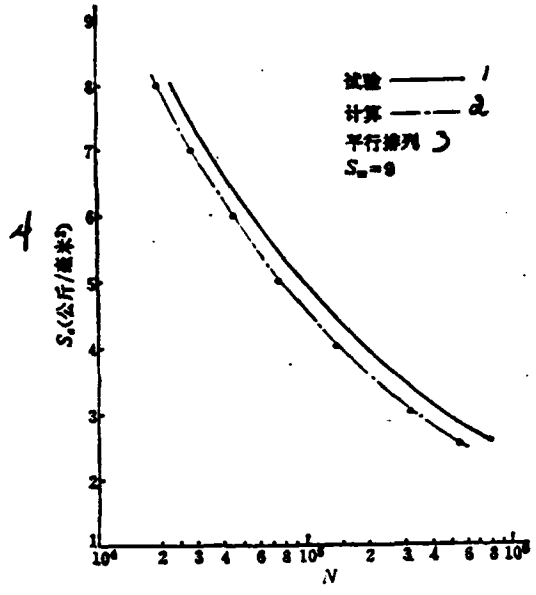


Fig.11 *S-N* curve

1--experimental; 2--calculated; 3--parallel array; 4--(kg/mm$^2$)

In order to carry out the calculation for life prediction, the stress severity factor $K_y = K_{ymax}$ corresponding to $P_{max}$ and $P_{min}$ is used. Then the equivalent stress level is:

$$\left.\begin{aligned} K_V &= K_{V_{max}} \\ S_m &= (S_{max} + S'_{min})/2 \\ S'_a &= (S_{max} - S'_{min})/2 \end{aligned}\right\} \qquad (5)$$

where $$S'_{min} = K_{V_{max}} S'_{min} / K_{V_{min}}$$

Then, life can be calculated based on the procedures described in section IV of this paper. The results are shown in Figures 7-11.

## VII. DISCUSSION OF RESULTS

1) The stress severity factor method was orignally proposed by Jarfall [1]. It was further developed and used in some countries in the fatigue design of aeronautic structures. This study considered the modeling effect of the rivet. In this paper, the stress severity factor

concept was used as the basis to obtain coefficients $\alpha$ and $\beta$ and the results were also given. This paper also proposed an empirical method to determine the effect of scratch through experiments. This paper extended the stress severity factor method to the calculation of the S-N curve of joints. It provided a base for the preliminary life prediction calculation under programmed load conditions.

2) In order to verify the reliability of this method, a batch of riveted joints were fatigue tested and the following conclusions were obtained:

The calculated destructed portion coincides with the experiment. The ratios between calculated results and experimental results are mostly between 1.0 and 0.75.

This method was further verified in the fatigue experiment and results analysis of a certain wing joint of an aircraft.

3) There must be a lot of shortcomings and errors in the problems described in this paper. Your comments are welcome.

REFERENCES

[1] Jarfall, L.E. "Optimum Design of Joints, The Stress Severity Factor Concept". The Aeronautical Research Institute of Sweden, 1967. May.

[2] Cornell, B.L. and Darby, L.G. (Lockheed-Georgiaco.), Correlation of Analysis and Test Data to the Effect of Fastener Load Transfer on Fotigue (AIAA paper No. 74-983).

[3] Handbook of Aircraft Structural Joints Analysis (fatigue), Third Mechanical Department 628 office 1975

[4] R. E. Peterson, Design Stress Concentrating Coefficient, China Industrial Publication Co. 1965.

# THE CRACK-FREE LIFE PREDICTION FOR STRUCTURAL JOINTS UNDER CONSTANT AMPLITUDE LOADS

*Xue Jingchuan and Yang Yugong*
*(Aircraft Sirength Research Instiiute)*

Abstract

This paper briefly describes a method of detailed designing and predicting the fatigue life for structural joints under constant amplitude loads by means of the Stress Severity Factor concept

$$K_v=\frac{\alpha\beta}{\sigma_{st}}\left[K_{fr}\frac{R}{dt}\theta+K_t\frac{P_e}{Wt}\right]$$

Based on the Stress Severity Factor concept, an approach for determining factors $\alpha$ and $\beta$ is developed and some of their values are derived from fatigue tests.

An approach dealing with the cratch is created by fitting test data, and the relation between the corrective $S-N$ curves of structural joints and the $S-N$ curves of materials is defined.

More than 100 specimens of revited joints were tested. The test data obtained were compared with the analytical results favorably and thereby testified the feasibility of this method.

In addition, the present method was employed to predict the full-scale $S-N$ curves of structural joints for their preliminary design and gave quite good results under the given conditions.

# AN ANALOGY METHOD FOR CRACK INITIATION LIFE PREDICTION

Zhang Fuze
Chinese People's Liberation Armed Forces, Air Force Research Institute

## ABSTRACT

This paper presented an analogy method for crack initiation life prediction of components. It employs the life (or useful life) of a known component obtained from endurance tests under spectrum load to predict the life of some type of components untested. The prediction formula of this analogy method was deduced in this paper. It could practically eliminate the scattered effect of the constant Q in the Miner equation $\left(\Sigma\frac{n}{N}=Q\right)$. Therefore, it was capable of improving the accuracy of the life prediction. This paper also gave the analogy prediction of specimens under five types of spectrum load and an example of analogy prediction of large scale structure components of an airplane. It was also verified by fatigue tests.

In the research of analogy life prediction in 1979, Professor Kao Chengtung of Beijing Aeronautics and Astronautics Institute has given his guidance. The verification work was carried out by Engineer Ho Tungen of the Air Force Research Institute. In the analogy computation of specimens, Engineers Koo Ming yuan and Zhang Shechak provided experimental data without reservation. Many thanks to these people.

## I. INTRODUCTION

As is commonly known, ever since Miner's theory was established in 1945, although it is still widely used, it still has some inadequacy and inaccuracy. The most serious problem is the scattering of the constant Q in the equation. In theory Q = 1; however, in practice it scattered quite widely (several times in several 10 times in difference), This brings significant errors in life prediction calculation.

This paper deduces an analogy crack initiation life prediction calculation equation of components based on the Miner theory and the equation $S^mN=c$. In the computation, it is not necessary to manually

select the highly scattered Q value. Therefore, it is possible to raise the accuracy and reliability of life predicti· Consequently, full scale fatigue tests can also be reduced.

In the design of airplanes and the calculation of airplane characteristics, the analogy method has been used over a long period of time and is widely applied. However, using an analogy method to calculate the fatigue life of components has not reached a mature stage with methods and complete set of equations. The author of this paper derived an earning-loss analogy equation (same principle as the one used in this paper) in 1969 and carried out some practical applications.

## II. THE ESTABLISHMENT OF ANALOGY LIFE PREDICTION EQUATION FOR CRACK INITIATION

Use the Miner equation to start with:

$$\lambda \sum_{i=1}^{K} \frac{n_i}{N_i} = Q \qquad (1)$$

where $\lambda$--cycle number of components with known life

$n_i$--the cycle number of the ith order load in one cycle of spectrum load for a component with known life

$N_i$--destruction cycle number under ith order load and then introduce the equation /52

$$S_a^m N = c \qquad (2)$$

where $S_a$--stress amplitude of the load

N--destruction cycle number of the material corresponding to a stress amplitude of $S_a$

m and c--relevant constant characteristics to the material, shape and cyclic load of the component.

From equation (2), for the same component at the same location, there is

$$S_{a_1}^m N_1 = S_{a_2}^m N_2 \qquad (3)$$

Received in May 1981.

i.e.,

$$\frac{N_i}{N_p} = \left(\frac{S_{ap}}{S_{ai}}\right)^{-i} \tag{4}$$

where $S_{ap}$--an arbitrary constant stress amplitude
$N_p$--destructive cycle number corresponding to $S_{ap}$.

Now, let us multiply equation (1) by $N_p$,

$$\lambda \sum_{i=1}^{K} n_i \frac{N_p}{N_i} = QN_p \tag{5}$$

From equations (4) and (5):

$$\lambda \sum_{i=1}^{K} n_i \left(\frac{S_{ai}}{S_{ap}}\right)^{-i} = QN_p \tag{6}$$

Similarly, the expression for the components with unknown life is

$$\lambda' \sum_{i=1}^{j} n_i' \left(\frac{S_{ai}'}{S_{ap}}\right)^{-i} = Q' N_p \tag{7}$$

Under the conditons that the structural form, load properties, loading sequence and material type are basically the same for components with known and unknown lives, we have

$$\lambda \sum_{i=1}^{K} n_i \left(\frac{S_{ai}}{S_{ap}}\right)^{-i} = \lambda' \sum_{i=1}^{j} n_i' \left(\frac{S_{ai}'}{S_{ap}}\right)^{-i} \tag{8}$$

$$\lambda' = -\frac{\sum_{i=1}^{K} n_i \left(\frac{S_{ai}}{S_{ap}}\right)^{-i}}{\sum_{i=1}^{j} n_i' \left(\frac{S_{ai}'}{S_{ap}}\right)^{-i}} \tag{9}$$

Equation (9) is the computational analogy equation for the prediction of crack initiation life of components. If the spectrum load is not a stress spectrum but an overload spettrum, then it is expressed in the following.

In the elastic region, for the same component at the same location, the stress amplitude is proportional to the overload increment. Then we have

$$\lambda' = \frac{\sum_{i=1}^{K} n_i \left(\frac{\Delta g_i}{\Delta g_p}\right)^{m_i}}{\sum_{i=1}^{j} n_i' \left(\frac{\Delta g_i'}{\Delta g_p}\right)^{m_i}} \lambda \qquad (10)$$

53

where $\Delta g_i$--the ith order overload increment of component with known life

$\Delta g_i'$--the ith order overload increment of component with unknown life

$\Delta g_p$--arbitrary overload increment

Equation (10) is the analogy calculation equation for known overload spectrum. In equations (9) and (10), because $S_{ap}$ and $\Delta g_p$ are arbitrary quantities, then let $S_{ap.} = 1$ or $\Delta g_p = 1$ to further simplify equations (9) and (10).

As for the analogy prediction for identical components, in engineering it is possible to use the average value m as an approximation and further to eliminate the effect of cyclic characterics on the value of m to make $m_i = m_i' = m$ and to convert the stress amplitude to stress increment ($\Delta S = S_{imax} - S_{imin}$). Thus, the following simplified equation can be obtained:

$$\lambda' = \frac{\sum_{i=1}^{K} n_i \Delta S_i^m}{\sum_{i=1}^{j} n_i' \Delta S_i'^m} \lambda \qquad (11)$$

or

$$\lambda' = \frac{\sum_{i=1}^{K} n_i \Delta g_i^m}{\sum_{i=1}^{j} n_i' \Delta g_i'^m} \lambda \qquad (12)$$

Based on the above equations, as long as the value of m is obtained, the unknown life $\lambda'$ can be determined.

## III. VALUE OF m AND ITS EFFECT ON LIFE

1. The value of m during the crack initiation period is usually determined experimentally in engineering where good $\varsigma$-N curves are not available. Under the conditions that no test was performed, it is usually taken as 5-10 [1]. From the analogy equation, the error of the relative life obtained from the analogy method using m is smaller than that of the absolute life obtained directly from the Miner equation by choosing Q. This is because whether the m value was too large or too small, the numerator and the denominator would increase or decrease simultaneously. The effect on the relative life ($\lambda'/\lambda$) obtained from the analogy method is very small. For example, the data and curve shown in Figure 1 were obtained based on different m values using the analogy method. They were calculated based on the identical components of two different airplanes under their own spectrum load using the analogy method.

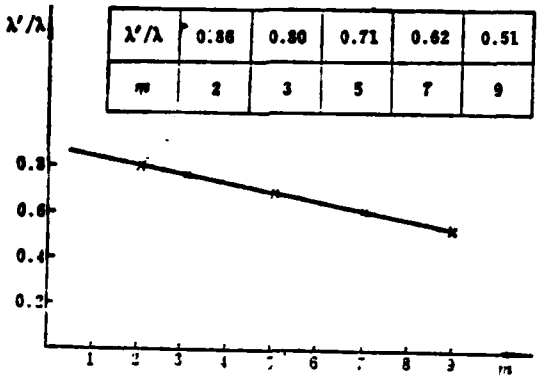


Fig. 1 Relation between $\lambda'/\lambda$ with $m$

From Figure 1 we can see that the relative life decreases with increasing m value, but the change is gradual. When the value of m is increased by 1, the relative life is decreased by 5%. In the Miner equation, when the constant Q is increased by 1, then the life is increased by 100%. Furthermore, the variation of Q in the calculation is large which causes a larger error in the calculation. Based on these results, we know that for the sample component, the analogy method will not cause large error in life prediction due to error in choosing m. Therefore, this analogy method not only eliminated the effect of Q value on the Miner equation but also demonstrated its superiority. In addition, its superiority has been demonstrated by the reduction of life prediction due to the decrease in the error caused by the m value.

2. The m value during the crack initiation stage, when perfect S-N curves are availble, can be used to obtain $m_i$ and $m_i'$ under different cycling characteristics $R_i$ to further improve the accuracy of the estimation. Under this condition, it is also possible to directly use Miner's equation and eliminate Q to perform the analogy procedures.

## IV. ACTUAL SAMPLE OF ANALOGY METHOD FOR PREDICTION OF CRACK INITIATION LIFE

### 1. Specimen analogy method example

The experimental fatigue data used in the specimen forming life prediction using the analogy method were obtained by Beijing Materials Research Institute in 1980. The loading spectra used in the tests were variable average spectrum, constant average spectrum, double wave (two-flow) spectrum, fatigue indicator spectrum and constant damage spectrum. The tester was a pc160N hydraulic servo fatique tester of the Schenck Company. The loading sequence of all the spectra is low-high-low. The specimen material is lead alloy Ly12-CZ. Its mechanical properties are shown in Table 1. The thickness of specimen plate is 2.5 mm and $K_t = 4$.

TABLE 1. Mechanical properties of the specimens

| $\sigma_{ys}$ (kg/mm$^2$) | $\sigma_b$ (kg/mm$^2$) | $\delta_{10}$(%) |
|---|---|---|
| 35.8 | 47.8 | 17.4 |

The analogy method was used for this specimen using the fatigue test results which give more accurate programmed spectra. The procedures of the analogy method involve the use of fatigue test life of a set of specimens under a particular spectrum load to predict the life of another set of specimens under another spectrum load. Then the calculated results are compared with those obtained from experiments to determine the relative error between the two conditions. Let us now use the constant average spectrum and fatigue spectrum as an example to carry out the analogy prediction with results shown in Tables 2, 3 and 4. The m value in the calculation took into consideration two conditions: one condition was to consider the effect of the cyling characteristics

$R_i$ on m which involved the computation of the values of $m_i$ at different $R_i$ and the other condition was not to consider the effect of $R_i$ on m which used the average value of m in the computation.

Similar methods were used to carry out analogy calculations to predict specimen life under variable average spectrum, double wave spectrum and constant change spectrum loads. In the meantime, the Miner equation was also used to calculate the life of the specimen and the results were compared with those of the fatigue test. They are also shown in Tables 5 and 6. In order to compare the calculated results with the experimental ones more directly and realistically, no correction was made for the calculated and tested lives. Therefore, the calculated lives in Table 5 and 6 are true reflections of the analogy method with respect to the Miner equation. The fatigue tested life is the realistic view of the specimen under spectrum load. If the tested life of the specimen has already taken scatter coefficient and other data treatment into consideration, the calculated life based on the analogy method contained the same scatter coefficient and data treatment.

The S-N curves used in the above calculation were also determined by Beijing Materials Research Institute. The properties of the material of the specimen and $K_t$ are identical to those for the specimens used in the above mentioned five fatigue tests. Therefore, the S-N curves used in this analogy calculation are relatively more accurate and relevant.

2. Analogy prediction example of fatigue initiation life of large scale structural pieces

The fatigue test data used in this analogy prediction were the results of full scale fatigue experiment of the main stress parts on the wing and fuselage of airplanes of the same type for different applications. This fatigue test of large scale structural components was performed on a special equipment. The error of load increment and load indicator is less than 2%.

Table 2 The analogy computation of the specimens

| ① | | | | | | | | | | | | | | | | Σ |
|---|---|---|---|---|---|---|---|---|---|---|---|---|---|---|---|---|
| | $g_{i\max}^{j}$ | 2.84 | 3.03 | 3.29 | 3.54 | 3.79 | 4.05 | 4.28 | 4.56 | 4.81 | 5.05 | 5.30 | 5.51 | 5.79 | 6.02 | 6.53 | |
| | $y_{i\max}^{j}$ | 1.57 | 1.37 | 1.11 | 0.86 | 0.62 | 0.35 | 0.12 | -0.15 | -0.41 | -0.65 | -0.90 | -1.10 | -1.38 | -1.61 | -2.12 | |
| | $k_i^j$ | 0.553 | 0.452 | 0.337 | 0.243 | 0.164 | 0.086 | 0.028 | -0.033 | -0.085 | -0.129 | -0.17 | -0.2 | -0.238 | -0.267 | 0.325 | |
| | $m_i^j$ | 3.19 | 3.07 | 3.19 | 3.12 | 3.09 | 3.15 | 3.26 | 3.49 | 3.53 | 3.52 | 3.62 | 3.62 | 3.57 | 3.72 | 3.67 | 平均3.38 ② |
| | $\Delta g_i^j$ | 1.27 | 1.66 | 2.18 | 2.68 | 3.17 | 3.70 | 4.16 | 4.71 | 5.22 | 5.7 | 6.20 | 6.61 | 7.17 | 7.63 | 8.65 | |
| | $n_i^j$ | 100 | 112 | 107 | 62 | 53 | 33 | 30 | 16 | 11 | 8 | 9 | 6 | 3 | 6 | 1 | |
| 第二加载谱块计算结果 | ③ 计$R_i$的影响 $\Delta g_i^{j\,m_i^j} n_i^j$ | 214 | 530.77 | 1285.07 | 1343.54 | 1873.02 | 2034.12 | 3128.7 | 3572.48 | 3756.38 | 3662.4 | 6648.12 | 6588.34 | 2265.86 | 9583.15 | 2746.93 | $\sum_{i=1}^{15} \Delta g_i^{m_i^j} n_i^j \times 2$ = 93738.85 − 2746.93 |
| | ④ 不计$R_i$的影响 $\Delta g_i^{m'} n_i^j$ | 224.85 | 624.85 | 1502.28 | 1752.84 | 2647.69 | 2784.31 | 3765.73 | 3059.57 | 2980.55 | 2920.82 | 4369.68 | 3618.38 | 1589.43 | 4986.00 | 1501.36 | $\sum_{i=1}^{15} \Delta g_i^{m'} n_i^j \times 2$ = 74986.38 − 1501.36 |

⑤ 注：(1) 表中加粗是常均值谱中的上半周期的各参数值，下半周的各参数值与上半周相同，但无6.53这一级载荷（计算中注意减掉）；⑥

(2) 不计$R_i$的影响，即取$m_i^j$ = 常值（平均$m'$值）；⑦

(3) 一个循环周期为50飞行小时。⑧

Key: 1—parameters and computation of the constant average spectrum; 2—average; 3—considering the effect of; 4—not considering the effect of; 5—note; 6—data in the table are the parameters of the upper half period in the constant average spectrum; 7—not considering the effect of $R_i$ which means $m_i$ =const (average m' value); 8—a cycle is 50 flight hrs.

Table 3 The analogy computation of the specimens

| 疲劳指示谱参数及计算 | | | | | | | | | | | | | | | |
|---|---|---|---|---|---|---|---|---|---|---|---|---|---|---|---|
| $g_{i\max}$ | | 2.50 | 3.50 | 3.50 | 4.50 | 4.50 | 4.50 | 6.00 | 6.00 | 6.00 | 7.00 | 7.00 | 8.00 | | | Σ |
| $g_{i\min}$ | | 0.50 | 0.50 | 0.25 | 0.25 | 0 | 1.00 | -0.25 | 1.00 | -0.50 | -0.50 | -0.75 | -0.75 | | | |
| $R_i$ | | 0.20 | 0.143 | 0.0714 | 0.0556 | 0 | 0.222 | -0.0417 | 0.167 | -0.0833 | -0.0714 | -0.107 | -0.0938 | | | |
| $m_i$ | | 3.05 | 3.28 | 3.22 | 3.26 | 3.29 | 3.53 | 3.41 | 3.40 | 3.47 | 3.48 | 3.47 | 3.44 | | | 平均3.36 |
| $\Delta g_i$ | | 2.00 | 3.00 | 3.25 | 4.25 | 4.50 | 3.50 | 6.25 | 5.00 | 6.50 | 7.50 | 7.75 | 8.75 | | | |
| $n_i$ | | 124 | 111 | 112 | 22 | 28 | 101 | 16 | 16 | 6.00 | 9 | 1 | 1 | | | |
| 计$R_i$的影响 | $\Delta g_i^{m_i} n_i$ | 1026.97 | 3987.90 | 4983.88 | 2660.19 | 3940.88 | 8411.68 | 8280.78 | 3987.31 | 3971.58 | 9987.46 | 1218.64 | 1739.83 | | | 53821 88 |
| 不计$R_i$的影响 | $\Delta g_i^{m} n_i$ | 1373.16 | 4458.83 | 5076.89 | 2843.21 | 4384.83 | 6788.16 | 7555.75 | 3569.82 | 3232.51 | 7842.38 | 972.87 | 1462.67 | | | 50263 28 |
| 注 | | (1) 表中数据是疲劳计谱的全周值； (2) 不计$R_i$的影响，即是计算中取$m_i$=常值（平均m值）； (3) 一个循环周期为50飞行小时。 | | | | | | | | | | | | | |

Key: 1—parameters and computation of the fatigue indicating spectrum; 2—average; 3—considering the effect of; 4—not considering the effect of; 5—data in the table are the full cycle values of the fatigue indicating spectrum; 6—not considering the effect of $R_i$, i.e., $m_i$=const (average m value) in the computation; 7—a cycle is 50 flight hrs; 8--notes.

Table 4 The analogy computation of the specimens

| | |
|---|---|
| ① 疲劳试验寿命 | (1) 在常均值谱作用下，一组试样（六个）的平均疲劳试验寿命$\lambda'=35.0$，即$T'=35.0\times50=1750$小时 ③<br>(2) 在疲劳计谱作用下，一组试样（六个）的平均疲劳试验寿命$\lambda=64.0$，即$T=64.0\times50=3200$小时 ④ |
| ② 类比计算寿命及误差 | (1) 在疲劳计谱作用下，以试件疲劳试验寿命（$\lambda=64.0$）类比估算常均谱下的试样寿命$\lambda'$，取表2、表3的计算结果，类比计算：<br>$\lambda'=\dfrac{\sum_{i=1}^{23}n_i\Delta g_i^{m_i}}{\sum_{i=1}^{29}n_i^0\Delta g_i^{0m_i^0}}\lambda=\dfrac{53821.86\times64}{93738.85}=36.75$ 即$T'=36.75\times50=1837$小时（误差5%） ⑥ ⑤<br>(2) 在常均值谱作用下，以试件疲劳试验寿命（$\lambda'=35.0$）类比估算疲劳计谱下的试样寿命$\lambda$，取表2、表3的计算结果，类比计算，<br>$\lambda=\dfrac{\sum_{i=1}^{29}n_i^0\Delta g_i^{0m_i}}{\sum_{i=1}^{23}n_i\Delta g_i^{m_i}}\lambda'=\dfrac{93738.85\times35.6}{53821.86}=62.0$ 即$T=62.0\times50=3100$小时（误差3%） ⑧ ⑦ |

Key: 1--fatigue tested life; 2--analogy computed life and error; 3--(1) under constant average spectrum, average fatigue test life $\lambda'=35.0$ for a set of specimens (six), i.e., $T'=35.0\times50=1750$ hrs; 4--(2) under fatigue indicating load, average fatigue test life $\lambda=64.0$ for a set of specimens (six), i.e., $T=64.0\times50=3200$ hrs; 5--(1) under fatigue indicating spectrum load, using the specimen fatigue test life ($\lambda=64.0$) to compute the specimen life $\lambda'$ under constant average spectrum load using analogy computation. Taking the results in Tables 2 and 3 to perform analogy computation; 6--i.e., $T'=36.75\times50=1837$ hrs (error 5%); 7--(2) under the constant average spectrum load, using the specimen fatigue life ($\lambda'=35.0$) to compute specimen life $\lambda'$ under fatigue indicating spectrum. Taking the calculated results in Tables 2 and 3 to carry out analogy computation; 8--i.e., $T=62.0\times50=3100$ hrs (error 3%)

Table 5 The comparison between the results of fatigue tests and analogy computation

| 谱型 | 结果 / 项目 | | 疲劳试验寿命(小时) | 类比计算寿命(小时) | | 计算与试验值的相对误差 | |
|---|---|---|---|---|---|---|---|
| | | | | 计$R_i$影响($m_i$是变值) | 不计$R_i$影响($m$是常值) | 计$R_i$影响 | 不计$R_i$影响 |
| | | | ① | ② | ③ | ①—②/① | ①—③/① |
| 19 | 类比 | 常均值 27 | 1750 | 1837 | 2145 | 5% | 23% |
| | 类比 | 疲劳计 28 | 3200 | 3100 | 2611 | 3% | 18% |
| 20 | 类比 | 变均值 29 | 1950 | 1897 | 1750 | 3% | 11% |
| | 类比 | 常均值 30 | 1750 | 1799 | 1930 | 3% | 10% |
| 21 | 类比 | 变均值 31 | 1950 | 1992 | 2145 | 2% | 10% |
| | 类比 | 疲劳计 32 | 3200 | 3133 | 2910 | 2% | 9% |
| 22 | 类比 | 变均值 33 | 1950 | 1635 | 1804 | 16% | 7% |
| | 类比 | 双波(两流) 34 | 2160 | 2576 | 2586 | 19% | 19% |
| 23 | 类比 | 常均值 35 | 1750 | 1509 | 1804 | 14% | 3% |
| | 类比 | 双 波 36 | 2160 | 2505 | 2095 | 16% | 3% |
| 24 | 类比 | 疲劳计 37 | 3200 | 2628 | 2692 | 18% | 16% |
| | 类比 | 双 波 38 | 2160 | 2630 | 2568 | 22% | 19% |
| 25 | 类比 | 等损伤 39 | 950 | 1138 | 1537 | 20% | 62% |
| | 类比 | 双 波 40 | 2160 | 1803 | 1335 | 16% | 38% |
| 26 | 类比 | 常均值 41 | 1750 | 1259 | 1115 | 28% | 36% |
| | 类比 | 等损伤 42 | 950 | 1343 | 1491 | 41% | 57% |

Key: 9—specimen type; 10—results; 11—item; 12—fatigue test life (hrs); 13—life by analogy computation (hrs); 14—relative error of calculated and experimental values; 15—considering the effect of $R_i$ ($m_i$ is a variable); 16—not considering the effect of $R_i$ ($m$ is a constant); 17—considering the effect of $R_i$; 18—not including the effect of $R_i$; 19,20,21,22,23,24,25, 26—analogy; 27—constant average; 28—fatigue indicating; 29—variable average; 30—constant average; 31—variable average; 32—fatigue indicating; 33—variable average; 34—double wave (two flow); 35—constant average; 36—double wave; 37—fatigue indicating; 38—double wave; 39—equal damage; 40—double wave; 41—constant average; 42—equal damage

Table 6 Specimen lifescalculated with Miner's formula

| 计算 / 谱 | 疲劳试验寿命 | 按 $\Sigma\frac{n}{N}=Q$ 计算寿命 | | | | | | 类比计算寿命(计 $R_i$ 影响) | |
|---|---|---|---|---|---|---|---|---|---|
| | | $Q=0.5$ | $Q=1$ | $Q=1.5$ | 误差 | | | 寿命 | 误差 |
| | | | | | $Q=0.5$ | $Q=1$ | $Q=1.5$ | | |
| 变均值 | 1950 | 1320 | 2641 | 3961 | 32% | 35% | 103% | 1897 | 3% |
| 常均值 | 1750 | 1590 | 3180 | 4771 | 9% | 82% | 173% | 1799 | 3% |
| 疲劳计 | 3200 | 1814 | 3628 | 5441 | 43% | 13% | 70% | 3133 | 2% |
| 双波(雨流) | 2160 | 1327 | 2654 | 3981 | 39% | 23% | 84% | 2576 | 19% |
| 等损伤 | 950 | 1243 | 2486 | 3729 | 31% | 162% | 293% | 1138 | 20% |
| 注 | 类比计算只列了精确解(计 $R_i$ 影响) | | | | | | | | |

Key: 1--computation; 2--spectrum; 3—fatigue test life; 4—life computed based on $\Sigma\frac{n}{N}=Q$; 5—life based on analogy computation (considering the effect of $R_i$); 6--error; 7--life; 8—error; 9--variable average; 10—constant average; 11—fatigue indicating; 12--double wave (2 flow); 13--equal damage; 14--note; 15--only the accurate solutions (considering the effect of $R_i$) are listed for analogy computation

Table 7 The comparison between the lives estimated by analogy and the fatigue test lives of large components

| 结果 / 项目 / 谱 | 两构件类比估算的相对寿命($\lambda/\lambda'$) | 两构件疲劳试验的相对寿命($\lambda/\lambda'$) | 相对误差 | 公式 |
|---|---|---|---|---|
| 过载谱 | 0.635 | 0.65 | 2% | (13) |
| 应力谱 | 0.615 | 0.65 | 5% | (12) |

Key: 1—specimen; 2—results; 3—item; 4—relative life ($\lambda/\lambda'$) of the two structural components based on analogy computation; 5—relative life ($\lambda/\lambda'$) of the two components in fatigue test; 6—relative error; 7—equation; 8—overloading spectrum; 9—stress spectrum

The spectrum load in the fatigue test was measured using the same instrument on two types of airplanes. The compilation method of the two spectra is identical. The load increasing sequence is also the same (low-high type). Under these two spectrum loads, the fatigue crack positions of the two structural pieces are also the same.

In order to compare the effects of overloading spectrum and stress spectrum on the prediction equation, the analogy computation of this large scale structural component was carried out using these two spectra. The stress spectrum was obtained by directly measuring at the cracked portion. The $m_i$ and $m_i'$ used in the computation are obtained from the S-N curves together with the consideration of the effect of $R_i$. However, since the variation is not too large, the average value m was used in the computation. The results are shown in Table 7.

## V. CONCLUSIONS

1. This analogy life prediction method, through the verification of analogy computation of the five sets of specimens under five different types of spectrum load and large scale structural component analogy computation and fatigue tests has demonstrated that for the prediction of life of components of similar type, as long as the determination of m is reasonable, the analogy computation presented in this paper provides results of higher accuracy. They also agree very well with fatigue test results. Under this condition, the effect of the cycling characteristics $R_i$ on m (average value m) can be neglected and equations (11) and (12) can be used directly.

2. This analogy computation method to predict life is more convenient for the life prediction in the design stage. Using the life (known life) of the component of the original airplane, the life of the newly designed similar components can be calculated using this analogy method. Thus, it is possible to figure out whether the newly designed component has a higher or lower life of the original standard airplane. It is then very meaningful in design changes. It is also possible to calculate which components have a weak life and which components have a conservative life. This serves as a reference to the evaluation of the life of the entire airplane.

3. When the spectrum load of individual airplanes in use or the spectrum load of airplanes (or spectrum load of fatigue test) varies, this analogy method can very conveniently compute the variation of life caused by these changes.

4. From the computed results in Tables 5 and 6, it is clear that the results obtained using this method have a large difference as compared to those with Miner's equation. The causes are (1) the effect of scatter of Q is reduced, (2) this analogy method is a combination of the Miner equation and expression of S-N curves. It is not necessary to repeatedly check the S-N curves or constant life lines in computations. Therefore, the errors of the checking and plotting figures can be drastically reduced; (3) the effect of m on relative life is reduced.

5. For the analogy computations of different components under the conditions that the load characteristics and working sequences are basically the same, this method is still applicable based on the Miner theory. However, due to the difference in structural type and material, a certain degree of error is created. Therefore, some correction is necessary. However, some experimental results indicate that under the same load characteristics and loading sequence, different materials in some cases do not affect Q significantly [2]. It means that in some cases different materials do not affect this analogy method significantly.

REFERENCES

[1] Kao Chentung, "Compilation of Loading Spectrum", Acta Aeronautica, vol. 2, 1980.

[2] French, H. J. (1933) Trans Amer. Soc. Steel. Trsat 21 899. "Fatigue and Hardening of Steels".

# AN ANALOGY METHOD FOR CRACK INITIATION LIFE PREDICTION

*Zhang Fuze*

*(Air Force Research Institute)*

Abstract

A method for crack initiation life prediction of components is presented. This method employs the life of a given component obtained from endurance tests under spectrum load to predict the life of another untested same type component by analogy.

The formula for analogy life prediction is deduced from Miner's theory and formula $S^m N = C$ as follows:

$$\lambda' = \frac{\sum_{i=1}^{k} n_i \left(\frac{S_{ai}}{S_{ap}}\right)^{m_i}}{\sum_{i=1}^{j} n'_i \left(\frac{S'_{ai}}{S'_{ap}}\right)^{m'_i}} \lambda$$

or

$$\lambda' = \frac{\sum_{i=1}^{k} n_i \left(\frac{\Delta g_i}{\Delta g_p}\right)^{m_i}}{\sum_{i=1}^{j} n'_i \left(\frac{\Delta g'_i}{\Delta g'_p}\right)^{m'_i}} \lambda$$

where $n_i$, $S_{ai}$, $\Delta g_i$ and $\lambda$ are load cyclic number, stress amplitude, overload increment and life cyclic number of the given component in i level; $n'_i$, $S'_{ai}$, $\Delta g'_i$ and $\lambda'$ are those of the unknown component; $S_{ap}$ and $\Delta g_p$ are any constant stress amplitude and overload increment (they may be taken as unit in calculation); $m_i$, $m'_i$ are constant (generally between 5 and 10) and may be estimated from the $S-N$ curve or by experiments. In life prediction with this formula it is unnecessary to choose the constant $Q$ in Miner's formula, therefore its accuracy may be improved.

The lives of large components of two aeroplanes and the specimens under five different loading conditions are predicted by this analogy method. The results are quite consistent with fatigue test results and the comparison is shown in tables (4) and (3). This demonstrates that the formula presented in this paper is more accurate, particularly for components analogous to given ones, and may give quite satisfactory results provided the value of the m is estimated appropriately. According to Miner's theory it is possible to apply this analogy method to components different from given ones, but it is necessary to make appropriate correction in actual use.

# FLOW MECHANISM AND EXPERIMENTAL INVESTIGATION OF ROTATING STALL IN TRANSONIC COMPRESSORS

Beijing Institute of Aeronautics and Astronautics,
Lu Yajun and Zhang Shunlin

## ABSTRACT

In this paper, a vortex system flow model has been established for rotating stall based on vortex theory. A comparison of the calculated flow field using that flow model with experimental data was performed. This comparison indicated that its results agreed with the actual flow condition better than the small linear perturbation theory and other methods.

This paper gives a detailed experimental investigation on the transonic rotor undergoing rotating stall at non-designed rotation speed (8000 revolutions/minute; 13000 revolutions/minute; 15000 revolutions/minute). Some new flow phenomena worth further studying were observed.

## FOREWORD

Due to the complexity of the physical phenomenon of compressor rotating stall which is affected by many factors including some factors on board, despite the fact that for many years people tried to determine the relations between the aerodynamic parameters and the geometric parameters of the compressor and the characteristic parameters under the working conditions of rotating stall, no satisfactory result has been obtained. Recently, along with the improvement of the characteristics of axial compressors, rotating stall and this type of nonsteady flow phenomena have a more serious influence on the compressor characteristics and destructive effect. It frequently causes the blade of the compressor to break. It even resulted in major incidents involving loss of airplanes and human lives. Therefore, the study of rotating stall type of nonsteady flow phenomena is one of the important subjects in aeronautical technology.

This paper carried out an analytical study on the flow characteristics under the working condition of rotating stall. Using the vortex theory, a vortex system flow model and the flow field computation method were established under rotating stall conditions. Based on this computation method, a detailed theoretical calculation of the flow fields of a low speed rotor and a transonic rotor were carried out and the computed flow fields agreed with the actually measured flow field. This indicated that this flow model and flow field computation method are reasonable. This paper also contained an analytical investigation of oscillograms of the stall characteristic parameters as a function of time recorded during the onset, development and disappearance period of rotating stall of a transonic rotor. The following new flow phenomena worth further investigation are: (1) the "irregular separation" (i.e., serious separation of individual blades) phenomenon prior to the onset of rotating stall and (2) periodical variation of circumferential width of the stall cell with time together along with the periodical oscillation of the width of the stall cell in the radial direction of the blade in the duration in which the stall flow state was varied..

---

Received in April 1981

62

## I. THE ESTABLISHMENT OF PHYSICAL FLOW MODEL UNDER STALL CONDITIONS AND THE COMPUTATION EQUATION

In order to further understand the flow characteristics and influencing factors under rotating stall conditions, a flow model capable of reflecting this type of flow phenomenon characteristic must be established. Based on the experimental data obtained under rotating stall conditions of the abrupt type, we know that under these stall conditions, there exists vortex motion both up and down stream of the blade array. Therefore, the flow model for this condition founded based on vortex theory apparently can better reflect the characteristics of this type of flow phenomenon than other methods. In an axial compressor, the axial symmetry of the entire flow field is destroyed once the rotating stall phenomenon is produced. If the coordinate system is fixed in the rotating separation region, then the entire flow field is divided into two completely different diffracted flow regions. In the

main flow region outside the separation region, the diffracted flow and moment of the flow are basically the same as a certain steady condition. In the low velocity flow in the separation region, the strong separation of the flow made the diffracted flow loop moment very small. Because of the relative motion between the blade array and the separation cell, therefore, each blade in the blade array must continuously enter and exit this separation cell sequentially. When each blade enters and exits the separation cell once, the flow diffraction moment on the blade must vary once. This variation is the source of the periodical oscillation force on the blade. When the blade enters the separation cell from one side boundary of the main flow region, the diffraction flow moment accompanying the blade varies from large to small. Therefore, it forms a vortex flowing from the tail of the blade toward downstream of the blade array with diffraction flow moment in opposite direction to that of a blade in the main flow region. This phenomenon is similar to that of a peeling vortex at the tail of the wing during aircraft landing. When the blade leaves from the other side boundary of the separation region, the accompanying diffraction flow moment on the blade varies from small to large, then a vortex begins to flow from the tail whose direction is opposite to that of the diffraction flow moment on the blade in the main flow region. This phenomenon is similar to the formation of an adherent vortex on the airplane wing during take-off and simultaneously a take-off vortex is left behind on the ground. Because the blades in the blade array must enter and exit from both sides of the separation regions continuously and sequentially, therefore, two stable vortex streets are formed on either side of the separation region. If the effect of viscosity must be considered, then the intensity of the two vortical streets downstream from the blade array will gradually decrease. In this paper, the flow model uses two finite length constant intensity vortical streets to consider the effect of viscosity. The relative motion between the low velocity flow (or even reverse flow) in the separation region and the incoming flow from in front of the blade array will cause the existance of vortical motion in the upstream of the blade array (in the upstream vortical street). The shape of this vortical street is related to the size of the separation region and the flow velocity in the same region. In order to simplify the flow model and the complexity of the computation, let us use a finite

extension of the downstream vortical street towards upstream to consider the effect of vortex in the upstream region. Figure 1 gives the vortex system flow model established in this work. From this vortex flow model, it is possible to deduce the following flow computation equation: 63

$$\vec{W}=\vec{W}_1+\vec{W}_2+\vec{W}_3+\vec{W}_\infty$$

when

$$W_{1a}=+\frac{\Gamma}{2t}\frac{\mathrm{sh}(2\pi y/t)}{\mathrm{ch}(2\pi y/t)-\cos(2\pi x/t)} \tag{1}$$

$$W_{1u}=-\frac{\Gamma}{2t}\frac{\sin(2\pi x/t)}{\mathrm{ch}(2\pi y/t)-\cos(2\pi x/t)}$$

in these equations, Γ--intensity of point vortex

t--cascade distance of blade array

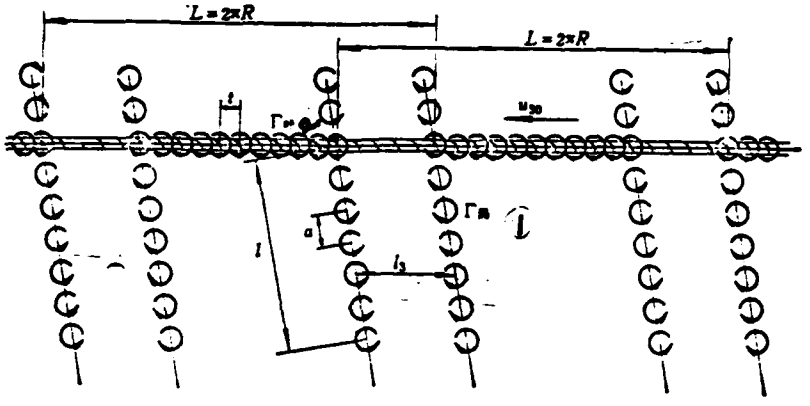


Fig.1 A flow model of vortex system in rotating stall condition

Key: 1--Γ vortex; 2--Γ blade

The subscripts u and a represent the components on the x and y-axis, respectively. Similar symbols apply to whatever follows:

$$W_{2a}=\sum_{i=1}^{l_{20}/t}W_{2af}$$

$$W_{2u}=\sum_{i=1}^{l_{20}/t}W_{2uf} \tag{2}$$

$$W_{2af}=-\frac{\Gamma}{2L}\frac{\mathrm{sh}(2\pi y/L)}{\mathrm{ch}(2\pi y/L)-\cos(2\pi\eta_i/L)}$$

$$W_{2uf}=+\frac{\Gamma}{2L}\frac{\sin(2\pi y/L)}{\mathrm{ch}(2\pi y/L)-\cos(2\pi\eta_i/L)}$$

$$\eta_i=x-$$

$c_1$--x coordinate of a blade in the separation region

L--circumference of the blade cascade loop

$L_{30}$--nominal width of the separation region

$$
\begin{aligned}
W_{3u} &= U_3\cos(\pi+\delta)+V_3\cos\delta \\
W_{3v} &= U_3\sin(\pi-\delta)+V_3\sin\delta \\
U_3 &= \frac{|\gamma|}{2\pi}\sum_{n=-\infty}^{+\infty}(\theta_{4n}-\theta_{5n}) \\
V_3 &= \frac{|\gamma|}{2\pi}\sum_{n=-\infty}^{+\infty}\left(\frac{\sin\alpha''_{4n}\sin\alpha'_{5n}}{\sin\alpha'_{4n}\sin\alpha''_{5n}}\right)
\end{aligned}
\tag{3}
$$

$\delta$--azimuth angle of the vortex street

$\gamma$--strength of the vortex street

$\theta_{4n}$, $\theta_{5n}$, $\alpha'_{4n}$, $\alpha'_{5n}$, $\alpha''_{4n}$ and $\alpha''_{5n}$ are the geometrical parameters in the vortex system model as shown in Figure 1.

$$
\begin{aligned}
W_{nu} &= v\sin\delta-\frac{\sum_{i=1}^{n_u}(W_{1i}+W_{2i}+W_{3i})_i}{n_u} \\
W_{nv} &= -\left[C_a+\frac{\sum_{i=1}^{n_a}(W_{1i}+W_{2i}+W_{3i})_i}{n_a}\right]
\end{aligned}
\tag{4}
$$

64

where v--flow velocity in the main flow region

$C_a$--average value of gas inlet axial velocity of the rotor

$n_a$--number of computational points on the cross-section of computation

$n_u$--number of computational points on the cross-section of computation outside the separation region

The detailed computational procedure regarding the two-dimensional flow field is reported in [1]. The velocity field of a transonic rotor computed based on the above method is shown in Figure 2. In order to verify the accuracy and adequacy of the model, its actual measured velocity field is given in Figure 3. Through the comparison and analysis of the velocity field, it can be concluded that this model is reasonable.

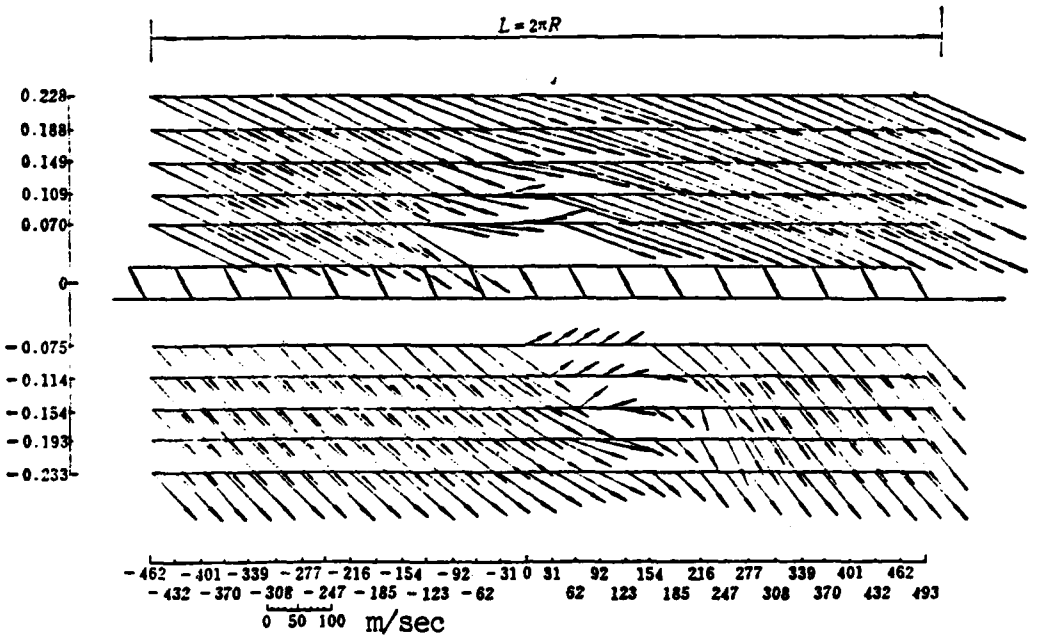


Fig.2 The calculated flow field in transonic rotor in rotating stall at $n = 13000$rpm with mass flow coefficient $\overline{C}_a = 0.263$

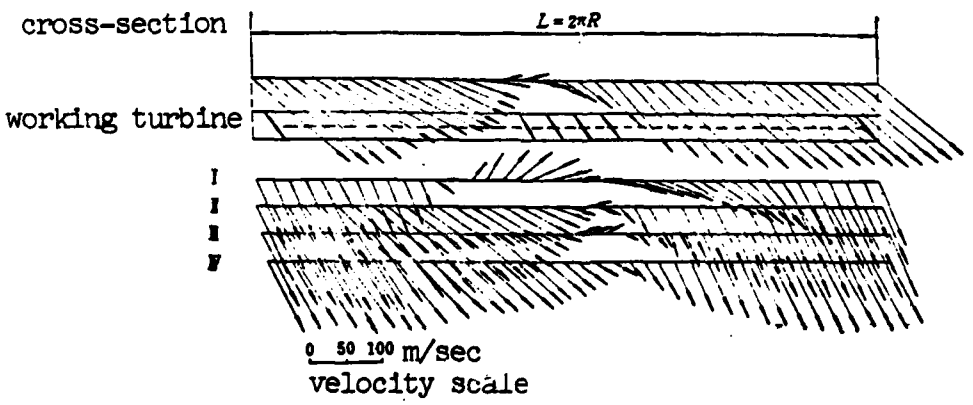


Fig.3 The measured flow field in transonic rotor in rotating stall at $n = 13000$rpm with mass flow coefficient $\overline{C}_a = 0.263$

## II. EXPERIMENTAL APPARATUS AND MEASURING EQUIPMENT

The test stand is a single or dual level compressor test equipment. The test stand has a given power of about 2000 horsepower. The given rotating speed is 22000 rpm. The experimental flow range is 0-20 kg/sec. The transonic test compressor has a designed rotating speed of 22000 rpm and flow rate at 13.6 kg/sec. The extreme pressure ratio under design condition is $\sim$1.6. The relative Mach numbers at the tip and the root of the blade are 1.4 and 0.9 respectively.

In order to measure the steady state parameters, such as the total static pressure at the inlet and outlet of the rotor and the flow direction at the outlet of the rotor, a six-point pressure probe was installed on the cross-section of the inlet and the outlet. In addition, four static pressure holes were placed on the inner and outer walls at the cross-section of the inlet and outlet. A single-point total static pressure combination probe which was capable of tracing the direction of the flow was installed on the cross-section of the outlet of the rotor. The flow of the rotor was measured through the inlet flow tube. The steady state parameters were acquired and recorded by a model XJ-100 automatic cycling measuring instrument. Some of the low pressure parameters were obtained directly from water displacement.

Dynamic parameters under stall conditions--the measurements of flow velocity and total gas pressure, were done by using model 55M hot filament wind velocity meter of the DISA/CTA series and the Chinese LDY 6-4 pressure pulser as its sensor. The dynamic parameters were acquired and recorded using the TEAC/R510 magnetic data recorder for the entire duration. During the whole experiment, a RS-1 oscilloscope was used to observe and monitor the dynamic parameters on site. The measurements of dynamic parameters and the treatment of data were reported in [2].

## III. EXPERIMENTAL RESULTS AND ANALYSIS

### 1. The actual measured flow field and its analysis of a transonic rotor under rotating stall condition

AD-A122 742 ACTA AERONAUTICA ET ASTRONAUTICA SINICA(U) FOREIGN TECHNOLOGY DIV WRIGHT-PATTERSON AFB OH S WANG ET AL. 14 OCT 82 FTD-ID(RS)T-1035-82 2/2

UNCLASSIFIED F/G 20/4 NL

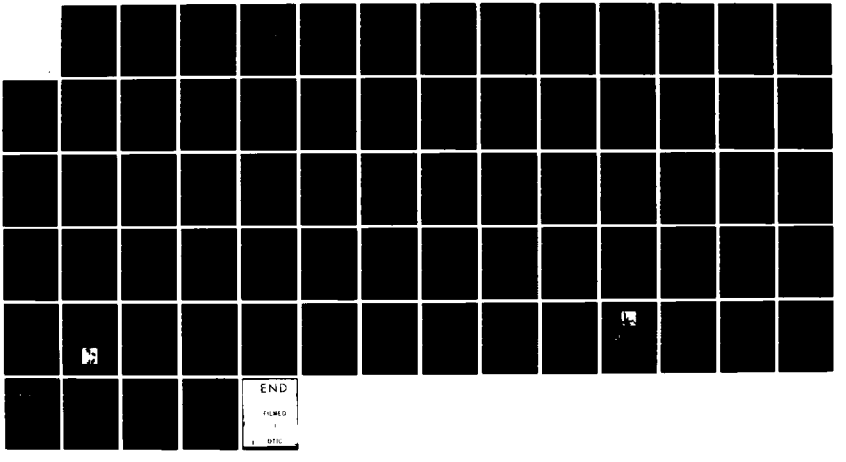

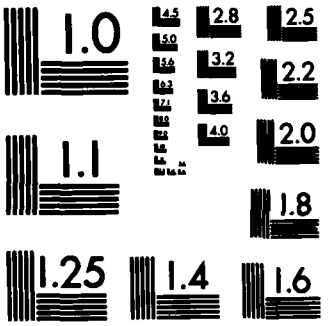


MICROCOPY RESOLUTION TEST CHART
NATIONAL BUREAU OF STANDARDS-1963-A

The actual measured basic element level flow field at the tip of the blade for a transonic rotor is shown in Figure 3 under the rotating stall condition. This flow field was measured when the transonic rotor was at 13000 rpm with a flow coefficient $\bar{C}_x=0.263$. From the flow field diagram, it is clearly shown that there are reverse flow regions both on the front and rear cross-sections of the rotor. The existence of the reverse flow areas would drive the downstream gas which had already been heated and pressured by the rotor back to the upstream region. This is the major reason for the melting of the rotor blade. The higher the pressure increase ratio is, the shorter the time required to melt the blade due to the reversed flow. It is even possible to create this type of destructive phenomenon in several tens of seconds. For a rotor with axial gas inlets, when reverse flow occurs, there exists vortex motion in the upstream region of the rotor. By comparing this flow field diagram with that reported in [3] for an actual measured flow field of a low velocity rotor, it can be concluded that the downstream reverse flow region of the transonic rotor dissipates faster than that of a low velocity rotor. In the flow field of a transonic rotor, the reverse flow region downstream from the rotor disappears very rapidly. On the N cross-section 170 mm from the rotor, reverse flow cell ceased to exist. For low velocity rotors the downstream reverse flow region shrinks slowly. It extends to the exit channel without dissipating completely. This situation indicates that the vortex intensity of the transonic rotor decreases more drastically than that of the low velocity rotor. Under rotating stall conditions of the transonic rotor, the fact such that vortical motion exists both upstream and downstream from the rotor and the vortex intensity downstream from the rotor decreases rapidly has significant meaning to the correction and improvement of the theoretical flow model.

## 2. The process and analysis of the onset, development and disappearance of rotating stall

### (1) Experimental results and analysis at 8000 rpm

The pressure signal oscillograms from steady state to the transition period of stall condition are shown in Figure 4. These probes

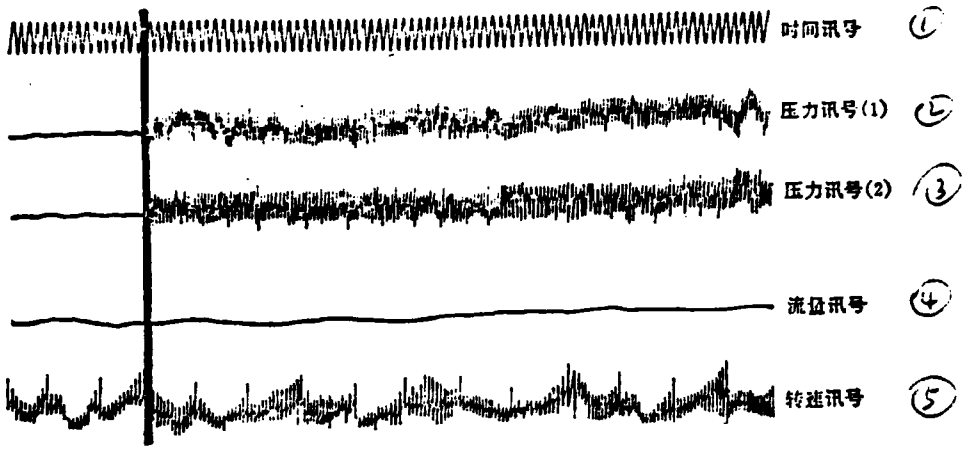


66

Fig. 4 The pressure signal oscillograms at n = 8000rpm in stall condition and in blade irregular separation condition

Key: 1--time signal; 2--pressure signal (1); 3--pressure signal (2); 4--flow signal; 5--rotating speed signal

were installed at the blade tip about 10 mm away from the outer wheel shell. From this figure, it can be observed that in the transition period from steady state to stall condition the average value of the pressure signal remained unchanged. However, in the transition period, the pulse amplitude of the pressure signal increased significantly. This flow phenomenon which showed basically the same average pressure before going into rotating stall as in steady state together with significant increase in pulse amplitude was called "irregular separation" in [2]. The enlarged "irregular separation" pressure oscillograms are shown in Figure 5. From this figure, we found that the pressure oscillogram contained 17 pulses in the period of each revolution. The 17 pulses have the same cycle period as that of the rotor. Because there were 17 blades on the rotor, therefore, it is convincing to say that 66
"irregular separation" is basically a flow phenomenon of severe separation on each blade before the rotor enters rotating stall conditions. Because the blade at the tip is thin and curved in shape for a transonic rotor, this further explained the conclusion obtained based on low velocity rotor studies that a relatively long period of "irregular separation" is frequently found for basic elements with small curvature angles. The same conclusion applies to transonic rotors.

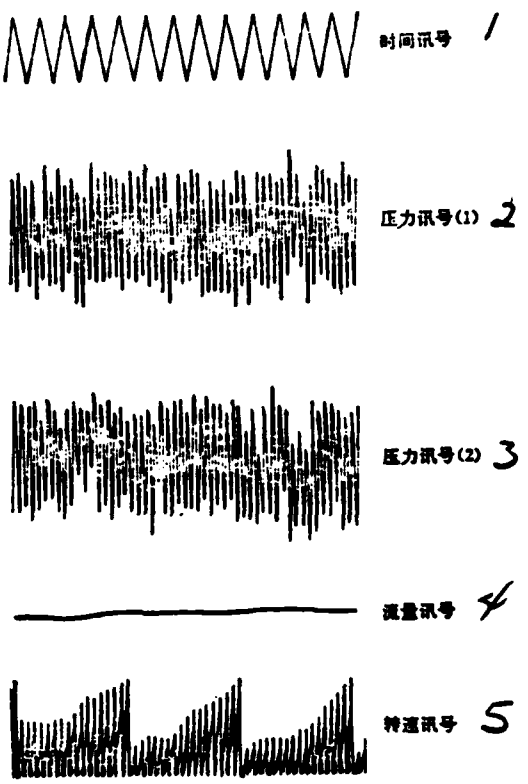


Figure 5. The pressure signal oscillograms at n = 8000 rpm in blade irregular separation conditions

Key: 1--time signal; 2--pressure signal (1); 3--pressure signal (2); 4--flow signal; 5--rotating speed signal

From the "irregular separation" condition to the rotating stall condition, the average value of the pressure signal decreased significantly and showed a two zone rotating stall phenomenon. Its rotating velocity $\bar{u}_{separation} = u_{separation}/u_{rotor}$ is 0.74. Continuing to save the flow, the separation region changes from 2 to 1; however, $\bar{u}_{separation}$ remained to be 0.74. This condition continued until the exhaust flow saving valve was completely shut. At this rotating speed, the compressor never had any coughing vibration.

(2) Experimental results and analysis at 13000 rpm

Two pressure probes were also placed at the tip of the blade in a similar manner. When the flow valve was closed to enter the stall transition period, the longitudinal pulse amplitude of the pressure oscillograms began to increase significantly to produce the "irregular separation" phenomenon of severe separation on each blade (see the first segment of the oscillograms in Figure 6). Immediately before rotating 67
stall occurred, a new flow phenomenon involving the periodical variation of the average value of the pulse amplitude existed (see the second segment of the oscillograms in Figure 6). Because its variation period

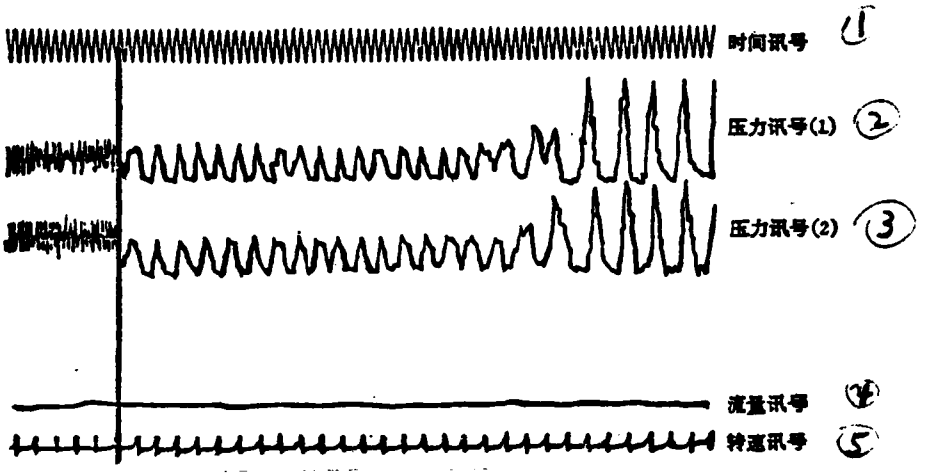


Fig.6 The pressure signal oscillograms at $n = 13000$rpm in blade irregular separation condition and in rotating stall condition

1—Pressure signal oscillogram in blade irregular separation condition with similar mean value of ampiitude;

2—Pressure signal oscillogram in blade irregular separation with amplitude mean value varying periodically;

3—Pressure signal oscillogram in rotating stall condition.

Key: 1--time signal; 2--pressure signal (1); 3--pressure signal (2); 4--flow signal; 5--rotating speed signal

coincided with that of the rotation, therefore, it was not rotating stall. It still was severe separation in the channels of each blade. Furthermore, it must be explained that the flow of gas through the channels of each blade is no longer the same. The appearance of this phenomenon is the sign that rotating stall condition will soon happen (see the transition between the second and the third segments of the oscillograms in Figure 6). This flow phenomenon which occurs immediately prior to rotating stall has never been recorded in the literature. Its pressure variation oscillogram is shown in Figure 6.

Continuing to cut the flow, since the appearance of the "irregular separation" phenomenon, it then went into a steady single zone stall condition, an alternating single and double zone variable condition and a steady double zone condition sequentially. In the process of leaving the stall condition, the transition from double zone to single zone condition and the steady single zone condition appeared in that order.

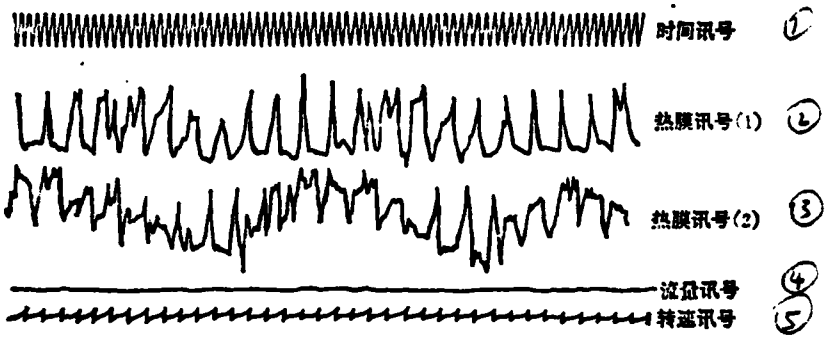


Fig.7 The oscillograms measured by two hot-wire anemometer probes in transient process of rotating stall at n=13000rpm
The upper one——the probe located at the root of the blade;
The lower one——the probe located at the tip of the blade.

Key: 1--time signal; 2--hot-wire anemometer signal (1); 3--hot-wire anemometer signal (2); 4--flow signal; 5--rotating speed signal

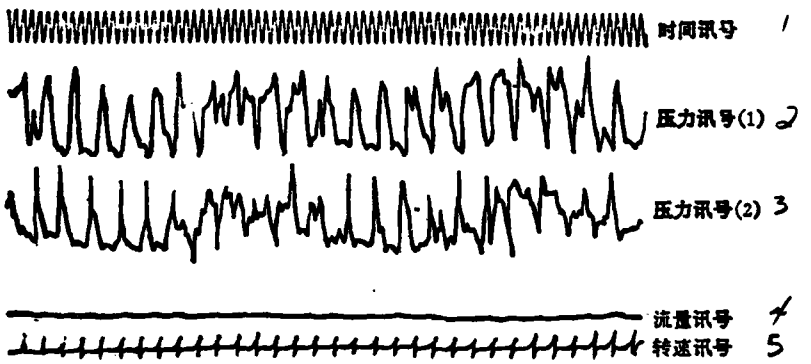


Fig.8 The oscillograms measured by two pressure transducers in transient process of rotating stall at n=13000rpm (transducers located at the tip of the blade)

Key: 1--time signal; 2--pressure signal (1); 3--pressure signal (2); 4--flow signal; 5--rotating speed signal

Finally, it excited the steady single zone stall condition to a steady state condition. In the stall condition described above, the rotating speed $u_{separation}$ in the separation region was about 0.7.

In the transition state under which the stall flow state varied, the oscillograms measured by the hot-wire anemometer probes (Figure 7) and the two pressure transducers (Figure 8) were recorded. The two hot-wire anemometer probes used to measure the two oscillograms in Figure 7 were installed at the blade tip and blade root of the rotor respectively.

The angle between them is 90°. The two pressure transducers used to measure the two oscillograms in Figure 8 were installed at the roots of the blades. Their angle was also 90°. The four probes were distributed on the same measurement cross-section. From Figure 8, it is clear that the two oscillograms are basically the same in shape. There was only a small phase difference in the transverse position of the oscillogram. It is apparent that the transverse distance was caused by the 90° angle between the two probes. Now we analyze the variation of the two anemometer probe oscillograms. The widths of the separation regions at the tip and the root of the blade were varied periodically. Their variation period is much higher than that of the rotor rotation. If the two oscillograms were moved laterally by half the period of the variation of the width of a separation region, we can see that when the width of the separation region at the root changed from narrow to wide, the width of the separation region at the tip changed from wide to narrow and the velocity average from small to large. This is true for vice versa. Thus, when the width of the separation region at the root reached the widest and narrowest values, the separation region width at the blade tip happened to be the narrowest and the widest, respectively. Combining the two oscillograms obtained using two hot-wire anemometer probes at different blade heights in Figure 7 and the two oscillograms obtained using the two pressure transducers placed at the tip in Figure 8 for analysis, it is clear that in the transition state the width of the separation region not only had periodical variation along the circumferential direction but also had periodical vibration along the radial direction of the blade. The circumferential and radial frequencies are the same at about 18 Hz. As long as the stall state begins to change, it is possible to create this effect. It appears that this phenomenon indicates that under rotating stall conditions, although the total flow across a certain cross-section of the rotor is invariant, yet the flow of elementsmay change with time. The above flow phenomenon which occurred in transonic rotors with larger blade twist along the blade height direction has not been reported in the literature both in China as well as abroad. Its discovery and further verification will provide a new and valuable stimulation in the area of blade stress analysis. It also gave a new understanding of unsteady flow structure.


Fig.9 The oscillograms measured by two hot-wire anemometer probes in transient process of rotating stall at n = 15000rpm

The upper one——the probe located at the middle of the blade;

The lower one——the probe located at the root of the blade.

Key: 1--time signal; 2--hot-wire anemometer probe signal (1); 3--hot-wire anemometer probe signal (2); 4--flow signal; 5--rotating speed signal

(3) Experimental results and analysis at 15000 rpm

In the 15000 rpm experiments, with the exception of placing a hot-wire anemometer probe at the center of the blade instead of at the top of the blade, the remaining measuring positions were unchanged. The entire experimental process and the conclusions obtained from the tests are similar to those of 13000 rpm. Due to the space limitation, they will not be described in detail. In this section, only the velocity oscillograms obtained from two hot-wire anemometer probes in the stall state variation process are given (see Figure 9).

## CONCLUSIONS

Through the study of the transonic rotor rotating stall phenomenon in this paper, the following conclusions can be obtained:

1. The vortex system flow model established on the basis of the vortex theory is reasonable for rotating stall conditions. The two dimensional flow fields obtained based on model computation agree with the measured flow field.

2. From the measured flow field obtained experimentally under rotating stall condtiions for transonic rotors, it is clear that reverse flow region exists both upstream and downstream from the rotor. This phenomenon indicates that not only is there vortical motion downstream from the rotor, but also upstream from the rotor. The downstream reverse flow region of the transonic rotor disappears faster than that of the low speed rotor. This indicates that the dissipation of the vortex intensity is much stronger for transonic rotors than that for low speed rotors.

3. In the blade tip area of a transonic rotor, because the shape of the blade is flat, straight, pointed and thin, the "irregular separation" phenomenon also occurs in these basic elements. This indicates that the conclusion obtained in the study of low speed rotors that "a relatively long period of "irregular separation" frequently will occur for some basic elements with smaller blade curvature angle before going into rotating stall condition", also applies to transonic rotors.

4. In the rotating stall effect occurred at a non-designed rotating speed for a transonic rotor, the relative rotating velocity $\bar{u}_{separation} = u_{separation}/u_{rotor}$ remains constant which is about 70% of that of the rotor rotating speed. Therefore, the transmitting velocity of the blade array relative to the separation region is 30% of that of rotor rotating speed. This value is far less than the transmitting velocity of the separation region (50-60% of rotor rotating speed) for low speed rotors. This may probably be due to the effect of compressibility on the transmitting velocity of the blade array corresponding to the separation region which is significantly increased for transonic rotors.

5. For a transonic rotor undercertain non-designed rotating speed and when the flow state of stall varies, the circumferential width will vary periodically with time. Simultaneously, it also oscillates periodically along the radial direction with the flow. Its periodical variation frequency is 15-18 cycle/sec. The newly observed flow phenomenon, after further verification, will provide a new stimulating source to the blade stress analysis and will give a new understanding on the nonsteady flow structure.

The comarades participating in the experimental work are Fong Yucheng, Tao Tehpin, Li Paochu and Hu Zuan and Comrades Zhang Sunchen, Zhang Shuchen, Lu Chiafong, and Ho Shuchen of the 606 Bureau.

REFERENCES

[1] Zhang Shenlin and Lu Yachuin. "Computation method of flow field and flow model under rotating stall condition", report BH-B670, Beijing Institute of Aeronautics and Astronautics, July 1981

[2] Lu Yachun, Zhang Chunlin and Lu Chiafong. "Experimental Investigation of Rotating Stall Phenomenon of Transonic Rotors", report no. BH-B669, Beijing Institute of Aeronautics and Astronautics.

[3] Ло Я-цзинь, Исследование вращающегося срыва (Влияние характеристик решетки колеса). Диссертация на соискание ученой степени кандидата технических наук. 1963.

[4] J. Valensi, Experimental investigation of the rotating stall in a single stage axial compressor. Journal Aeronautical science Vol. 25. No 1. 1958.

[5] I. J. Day and N. A. Cumpsty, The measurement and interpretation of flow within rotating stall cell in axial compressors. CUED/A-Turbo/TR90 1977.

# FLOW MECHANISM AND EXPERIMENTAL INVESTIGATION OF ROTATING STALL IN TRANSONIC COMPRESSORS

*Lu Yajun and Zhang Shunlin*

*(Beijing Institute of Aeronautics and Astronautics)*

Abstract

The flow characteristics of the rotating stall in compressors are studied. A flow model for rotating stall in axial compressors and its theoretical calculation method are developed on the basis of the vortex theory. By this method a detailed theoretical calculation is completed for a two-dimensional flow field in a transonic rotor at rotating stall. The flow field obtained is in good agreement with that measured from experiments. This shows that the flow model and its calculation method are reasonable.

The oscillograms of time-varying stall characteristic parameters recorded in the onset, growth and cessation processes of rotating stall in transonic ortor have been analyzed and studied. Some new flow phenomena deserving of further investigation have been discovered as follows: 1)" irregular separation", i. e. serious separation of individual blades, often preceded the onset of rotating stall in compressors with very small blade-camber angle; 2) periodical variation of the circumferential width of the stall cell with time and accompanying periodical oscillation of the width of the stall cell in the radial direction of the blade, which both occured in transient process of the rotating stall. The circumferential and radial oscillation frequencies were the same, about 15 to 18 Hz.

The discovered phenomena indicate that in stress analysis of the blade a corresponding exciting force must be considered. It seems that this discovery will be helpful to understanding of unsteady flow structure in transonic rotors.

## A BRIEF DESCRIPTION OF THE FIRST AERONAUTIC ENGINE SYSTEM, STRENGTH VIBRATION CONFERENCE 71

The Chinese Aeronautics Society held the first Engine Structure, Strength and Vibration Conference in Canton on December 10-15, 1981. There were 98 people from 35 units attending. The conference presented 57 papers with 52 papers collected into a symposium. It was published before the meeting. The meeting was divided into structure and strength/ vibrations for paper presentations and discussions. This meeting was well prepared and arranged. It paid great attention to actual practice with many materials and an academic atmosphere. It should promote future research. This meeting reflected new progress in the studies of structure, strength, and vibration of engines in recent years.

The finite element method was widely used in the study of engine structural strength and vibration analysis. In the meeting, not only the analytical procedures of the major components of the engine were proposed, but also some basic methods applicable to engine characteristics were presented: for example, a new method of structural automatic separation, the finite element analysis of the three dimensional elasticity problem, the turbine elasticity problem, the transition elements for analysis of solid-shell combination structure and tensile plate-plane beam combination structure, and the automatic formation of geometric shapes of turbine wheels, etc.

The papers in the areas of fatigue and crack of structural components indicated that research in this field is becoming increasingly important and a good foundation was laid. The papers involved the determination of aeronautical engine cyclic load, the prediction and experimental evaluation of life of major components, and the analysis of and experiments on turbine wheel cracks, etc.

The analysis of free and forced vibrations of periodic, on-board structures, discussions on the experimental methods to determine rotor critical rotating velocity, the analysis of the combined wheel-blade system model using group theory, the experimental study of

The blade-wheel system coupled vibration, the analysis of the effect of gas inlet irregularity vibration on compressor blade, etc., represented a new subject and characteristics of engine vibration research in recent years.

There were many reports on the analysis and experimental study of aerodynamic characteristics of the rotor-support system as well. Especially good results on elastic support, compressible hydraulic resistors and uncoordinated motion of the rotor were obtained.

In the meeting, many suggestions were made on future academic activities. Many people believed that schools, institutes and factories should organize to concentrate their efforts on overcoming difficulties in order to produce fruitful results quickly, which would also demonstrate the superiority of the socialist principle and save manpower, as well as materials, in order to change the poor image of engines in the areas of structure, strength and vibration. Certain key problems were discussed in detail. Finally, all attendants recommended that the next Engine Structure, Strength and Vibration Conference be held in 1983.

# A KIND OF TRANSITION FINITE ELEMENT FOR ANALYSIS OF SOLID-SHELL OR TENSILE PLATE--PLANE BEAM COMBINED STRUCTURE

Nanhua Power Plant Institute, Yin Zeyong, Yin Jing and Ren Peizheng

## ABSTRACT

A kind of transition element was established in this paper. When coordinated with standard isoparametric solid (or plane) elements and superparametric shell (or plane beam) elements of the same order, it can be used to treat the non-standard joint combined structure such as solid-shell or tensile plate-plane beam structures. The procedure to establish this kind of transition element was described. The formula of quadratic transition element was presented. The numerical results obtained showed that this kind of transition finite elent is very effective.

## I. INTRODUCTION

The engines used in aeronautical applications have many important parts and components which are composed of two parts such as solid and shell (tensile plate) or axisymmetric solid and axisymmetric shell (axisymmetric tensile plate). Some of these can be treated as a tensile plate-plane beam combined structure on the same plane after simplification. Examples are eccentric turbine, convex shoulder blade, etc. When the finite element method is used for the analysis of stress and vibration of these structures, if solid or plane elements are used for the entire combined structure, then not only the data preparation and computational load are increased but also possibly some symptoms are brought into the equations to be solved [1].

If solid element or plane elements are used for the solid portion or tensile plate portion of combined structures, and shell elements or plane beam elements are used for the shell portions as plane beam portion, then a coordinative distortion problem will appear between the two kinds of elements. In order to solve this coordinative problem, primary and accessory variable [2,3,4] combination element [5,6] penalty

element [4] and transition element [7,8] methods can be used.

The primary and accessory variable method and the penalty method are effective means to process non-standard joint combined structures. However, because of the need to distinguish the displacement vector of the primary and accessory nodes and to have the accessory node displacement vector not to appear in the equations, the program design of the primary/accessory variable method is relatively complicated. As for the penalty element method, the choice of the numerical value of the penalty matrix has a certain degree of difficulty. In this paper, a kind of transition element is established which is different from the ones described in [7,8]. This kind of transition element of any order can be used coordinatively with the standard isoparametric solid (or plane) element and superparametric shell (or plane beam) element of the same order. With respect to the program of the widely used standard isoparametric solid (or plane) element and superparametric shell (or plane beam) element, it is possible to add the kind of transition element established in this paper in order to facilitate the analysis of non-standard joint combined structures such as solid-shell and tensile plate-plane beam.

---

received in May 1981

## II. ARRANGEMENT OF NODES, GEOMETRIC SHAPE AND DISTRIBUTION OF DISPLACEMENT

73

The basic procedure to establish this kind of transition element can be described in the following: On the interface (or boundary line) of a standard isoparametric solid (or plane) element (for a three-dimensional solid element, sometimes on an edge), the original nodes of the solid (or plane) element are eliminated and replaced by the corresponding nodes of a superparametric (or plane beam) element of the same order. As for the remaining nodes of the solid (or plane) element, the shape functions are identical to the corresponding shape functions of standard isoparametric solid (or plane) element. As for the shell (or plane beam) element nodes, the shape functions are the same as the corresponding ones of the standard parametric shell (or plane beam) element.

Obviously, the shape function of this kind of transition element satisfies the requirement that its value is 1 at one node and 0 at any other node. Its distribution on the interface (or boundary line) nodes of the superparametric shell (or plane beam) element distortedly coordinates with the standard superparametric element of the same order. As for the corresponding interface (or boundary line) which contains nodes of an isoparametric solid (or plane) element alone, it coordinates distortedly with the standard isoparametric solid (or plane) element of the same order. Similarly, the two neighborning transition elements are also coordinatively distorted. From the following equation, this coordination can be verified. In addition, for this kind of transition element, besides arranging the interface (or boundary line) of the shell (or plane beam) element nodes, the displacement inside the element does not agree with the distortion assumption of the shell (or plane beam). In practice, for solid-shell or tensile plate-plane beam combined structures, with respect to the shell (or plane beam) portion near the joint the ideal shell (or plane beam) distortion assumption should also not be used. Thus, the established plane transition element should be in a plane stress or plane strain state, the axisymmetric transition element should be in axysymmetric solid stress state and the three-dimensional solid transition element should be in a three-dimensional stress state. From the actual equation, it is possible to verify that the displacement distribution of this kind of transition element can realize a constant strain state.

The following is an example using a quadratic transition element to obtain the expressions of the geometric shape and displacement distribution.

1. Quadratic axisymmetric transition ring element and quadratic plane transition element

Here only the former is discussed. The relevant expressions for the latter are identical. The matching quadratic axisymmetric solid isoparametric elements of the quadratic axisymmetric transition ring element are given in [9]. The matching quadratic axisymmetric superparametric elements can be established by initiating the method in [10].

However, we used a slightly different method directly [11]. Therefore, the total coordinates (r,z) and displacement (u,v) of the local coordinate point ($\xi$,$\eta$) in the axisymmetric transition ring element can be determined based on the following equations (see Figure 1).

$$\left.\begin{aligned}\begin{Bmatrix} r \\ z \end{Bmatrix} &= N_1 \begin{Bmatrix} r_1 \\ z_1 \end{Bmatrix} + N_1 \xi \frac{t_1}{2} \begin{Bmatrix} \cos\varphi_1 \\ \sin\varphi_1 \end{Bmatrix} + \sum_{i=2}^{6} N_i \begin{Bmatrix} r_i \\ z_i \end{Bmatrix} \\ \begin{Bmatrix} u \\ v \end{Bmatrix} &= N_1 \begin{Bmatrix} u_1 \\ v_1 \end{Bmatrix} + N_1 \xi \frac{t_1}{2} \begin{Bmatrix} -\sin\varphi_1 \\ \cos\varphi_1 \end{Bmatrix} \alpha_1 + \sum_{i=2}^{6} N_i \begin{Bmatrix} u_i \\ v_i \end{Bmatrix}\end{aligned}\right\} \quad (1)$$

where $r_1$, $z_1$, $r_i$, $z_i$, $u_1$, $v_1$, $u_i$, $v_i$ are the coordinate components and displacement components of the corresponding nodes. $\alpha_1$ is the other displacement component of node 1. The definitions of $\alpha_1$, $\phi_1$ and $t_1$ are all shown in Figure 1. The actual expressions of the shape functions are

$$\left.\begin{aligned} &N_1 = \frac{1}{2}\eta(\eta-1), \quad N_2 = \frac{1}{2}(1-\eta^2)(1+\xi), \\ &N_3 = \frac{1}{4}(1+\xi)(1+\eta)(\xi+\eta-1), \\ &N_4 = \frac{1}{2}(1-\xi^2)(1+\eta), \quad N_5 = \frac{1}{4}(1-\xi)(1+\eta)(-\xi+\eta-1), \\ &N_6 = \frac{1}{2}(1-\eta^2)(1-\xi)\end{aligned}\right\} \quad (2)$$

## 2. Quadratic three-dimensional transition element

74

The quadratic three-dimensional solid element to be matched with this kind of transition element can be obtained from [12]. The matching quadratic superparametric shell elements can be found in [10]. Therefore, the total coordinates (x,y,z) and displacement (u,v,w) of a local coordinate point ($\xi$, $\eta$, $\zeta$) in this type of transition element can be determined from the following equation (see Figure 2):

$$\left.\begin{aligned}\begin{Bmatrix} x \\ y \\ z \end{Bmatrix} &= \sum_{i=1}^{12} N_i \begin{Bmatrix} x_i \\ y_i \\ z_i \end{Bmatrix} + \sum_{j=13}^{15} N_j \begin{Bmatrix} x_j \\ y_j \\ z_j \end{Bmatrix} + \sum_{j=13}^{15} N_j \frac{\zeta}{2} \bar{V}_{3j} \\ \begin{Bmatrix} u \\ v \\ w \end{Bmatrix} &= \sum_{i=1}^{12} N_i \begin{Bmatrix} u_i \\ v_i \\ w_i \end{Bmatrix} + \sum_{j=13}^{15} N_j \begin{Bmatrix} u_j \\ v_j \\ w_j \end{Bmatrix} + \sum_{j=13}^{15} N_j \frac{\zeta}{2} t_j (\bar{v}_{1j} - \bar{v}_{2j}) \begin{Bmatrix} \alpha_j \\ \beta_j \end{Bmatrix}\end{aligned}\right\} \quad (3)$$

## III. STIFFNESS MATRIX, MASS MATRIX AND LOAD VECTOR

The general expression of the stiffness matrix [k] for transition element is still [12]

$$[k]=\int_V [B]^T[D][B]dV \tag{6}$$

where [D] is the elasticity matrix of the material which can be chosen based on the stress condition of the transition element. [B] is the strain node displacement matrix. The following is the actual expression corresponding to the quadratic transition element.

### 1. Quadratic axisymmetric transition ring element and quadratic plane transition element

For the quadratic axisymmetric transition ring element, here we use the following equations to define its strain vector {ε} and node displacement vector {δ}:

$$\{\varepsilon\}=[\varepsilon_r,\ \varepsilon_z,\ \gamma_{rz},\ \varepsilon_\theta]^T \tag{7}$$

$$\{\delta\}=[u_1,\ v_1,\ a_1,\ u_2,\ v_2,\ \cdots,\ u_6,\ v_6]^T \tag{8}$$

Under the conditions, the following system of equations exist:

$$[J]=\begin{bmatrix}\frac{\partial r}{\partial\xi} & \frac{\partial z}{\partial\xi}\\ \frac{\partial r}{\partial\eta} & \frac{\partial z}{\partial\eta}\end{bmatrix}=\begin{bmatrix}N_1\frac{t_1}{2}\cos\varphi_1+\sum_{i=2}^{6}\frac{\partial N_i}{\partial\xi}r_i & N_1\frac{t_1}{2}\sin\varphi_1+\sum_{i=2}^{6}\frac{\partial N_i}{\partial\xi}z_i\\ \frac{\partial N_1}{\partial\eta}\left(r_1+\xi\frac{t_1}{2}\cos\varphi_1\right)+\sum_{i=2}^{6}\frac{\partial N_i}{\partial\eta}r_i & \frac{\partial N_1}{\partial\eta}\left(z_1+\xi\frac{t_1}{2}\sin\varphi_1\right)+\sum_{i=2}^{6}\frac{\partial N_i}{\partial\eta}z_i\end{bmatrix}$$

$$=\begin{bmatrix}C_{11} & C_{12}\\ C_{21} & C_{22}\end{bmatrix} \tag{9}$$

$$[J]^{-1}=\frac{1}{|J|}\begin{bmatrix}C_{22} & -C_{12}\\ -C_{21} & C_{11}\end{bmatrix}=\begin{bmatrix}A_{11} & A_{12}\\ A_{21} & A_{22}\end{bmatrix} \tag{10}$$

where [J] is the "Jakobi" matrix, |J| and $[J]^{-1}$ are the determinant and inverse of [J] respectively.

(11)

where $[B]=[[B_1][B_2][B_3][B_4][B_5][B_6]]$

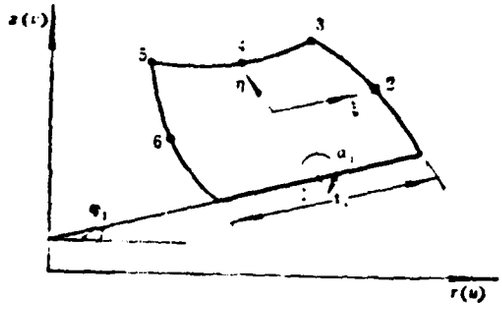

Fig. 1 A quadratic transition axisymmetric ring element

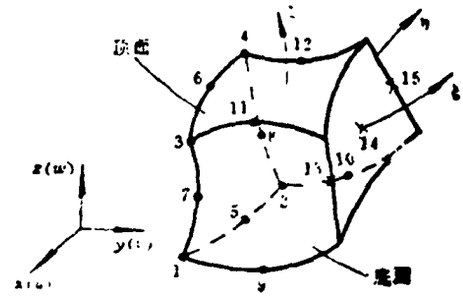

Fig. 2 A quadratic transition three-dimensional element

where $x_i$, $y_i$, $z_i$ and $u_i$, $v_i$, $w_i$ are the coordinate components and displacement components of node i, respectively; $(x_j, y_j, z_j)^T = \frac{1}{2}((x_j, y_j, z_j)^T_{top} + (x_j, y_j, z_j)^T_{bottom})$ is the coordinate component of node j; $\bar{V}_{3j} = (V_{3jx}, V_{3jy}, V_{3jz})^T = (x_j, y_j, z_j)^T_{top} - (x_j, y_j, z_j)^T_{bottom}$ is the normal vector at node j; $t_j = |\bar{V}_{3j}|$ is the thickness at node j. $\bar{v}_{1j}$ and $\bar{v}_{2j}$ are determined based on the following two equations, respectively:

$$\bar{v}_{1j} = \begin{Bmatrix} v_{1jx} \\ v_{1jy} \\ v_{1jz} \end{Bmatrix} = \frac{\bar{V}_{1j}}{|\bar{V}_{1j}|} = \frac{\bar{i} \times \bar{V}_{3j}}{|\bar{i} \times \bar{V}_{3j}|}, \quad \bar{v}_{2j} = \begin{Bmatrix} v_{2jx} \\ v_{2jy} \\ v_{2jz} \end{Bmatrix} = \frac{\bar{V}_{2j}}{|\bar{V}_{2j}|} = \frac{\bar{V}_{3j} \times \bar{V}_{1j}}{|\bar{V}_{3j} \times \bar{V}_{1j}|} \tag{4}$$

If $\bar{v}_{3j}$ and $\bar{I} = (1,0,0)^T$ are parallel, then $\bar{J} = (0,1,0)^T$ is used to replace $\bar{I}$. $u_j$, $v_j$, $w_j$, $\alpha_j$, $\beta_j$ are 5 displacement components of node j where $\alpha_j$ and $\beta_j$ are the rotating angles of $\bar{v}_{3j}$ around $\bar{v}_{2j}$ and $\bar{v}_{1j}$ respectively. The shape function expressions are:

$$\left.\begin{aligned}
N_i &= \frac{1}{8}(1+\xi_0)(1+\eta_0)(1+\zeta_0)(\xi_0+\eta_0+\zeta_0-2), && (i=1,\ 2,\ 3,\ 4) \\
N_i &= \frac{1}{4}(1-\xi^2)(1+\eta_0)(1+\zeta_0), && (i=9,\ 10,\ 11,\ 12) \\
N_i &= \frac{1}{4}(1-\eta^2)(1+\zeta_0)(1+\xi_0), && (i=5,\ 6) \\
N_i &= \frac{1}{4}(1-\zeta^2)(1+\xi_0)(1+\eta_0), && (i=7,\ 8)
\end{aligned}\right\} \tag{5}$$

$$\left.\begin{aligned}
N_j &= \frac{1}{4}(1+\xi_0)(1+\eta_0)(\xi_0+\eta_0-1), && (j=13,\ 15) \\
N_j &= \frac{1}{2}(1+\xi_0)(1-\eta^2). && (j=14)
\end{aligned}\right\}$$

$$\xi_0 = \xi_i\xi, \quad \xi_0 = \xi_j\xi, \quad \eta_0 = \eta_i\eta, \quad \eta_0 = \eta_j\eta, \quad \zeta_0 = \zeta_i\zeta.$$

$$[B_i]=\begin{bmatrix} A_{12}\frac{\partial N_i}{\partial \eta} & 0 & -\left(A_{12}\frac{\partial N_i}{\partial \eta}\xi+A_{11}N_i\right)\frac{t_i}{2}\sin\varphi_i \\ 0 & A_{22}\frac{\partial N_i}{\partial \eta} & \left(A_{22}\frac{\partial N_i}{\partial \eta}\xi+A_{21}N_i\right)\frac{t_i}{2}\cos\varphi_i \\ A_{22}\frac{\partial N_i}{\partial \eta} & A_{12}\frac{\partial N_i}{\partial \eta} & -\left(A_{22}\frac{\partial N_i}{\partial \eta}\xi+A_{21}N_i\right)\frac{t_i}{2}\sin\varphi_i \\ & & +\left(A_{12}\frac{\partial N_i}{\partial \eta}\xi+A_{11}N_i\right)\frac{t_i}{2}\cos\varphi_i \\ \frac{N_i}{r} & 0 & -\frac{N_i}{r}\xi\frac{t_i}{2}\sin\varphi_i \end{bmatrix} \tag{12}$$

$$[B_i]=\begin{bmatrix} A_{11}\frac{\partial N_i}{\partial \xi}+A_{12}\frac{\partial N_i}{\partial \eta} & 0 \\ 0 & A_{21}\frac{\partial N_i}{\partial \xi}+A_{22}\frac{\partial N_i}{\partial \eta} \\ A_{21}\frac{\partial N_i}{\partial \xi}+A_{22}\frac{\partial N_i}{\partial \eta} & A_{11}\frac{\partial N_i}{\partial \xi}+A_{12}\frac{\partial N_i}{\partial \eta} \\ \frac{N_i}{r} & 0 \end{bmatrix} \quad (i=2,\ 3,\ 4,\ 5,\ 6) \tag{13}$$

76

If one wants to obtain the relevant equations of the quadratic plane transition element, the fourth row of the matrices on the right hand of equations (7), (12) and (13) should be eliminated.

## 2. Quadratic three-dimensional transition element

Here the following equations are used to define the strain vector $\{\varepsilon\}$ and node displacement $\{\delta\}$ of the element:

$$\{\varepsilon\}=[\varepsilon_x,\ \varepsilon_y,\ \varepsilon_z,\ \gamma_{xy},\ \gamma_{yz},\ \gamma_{zx}]^T \tag{14}$$

$$\{\delta\}=[u_1, v_1, w_1, \cdots u_{12},\ v_{12}, w_{12}, u_{13}, v_{13}, w_{13}, \alpha_{13}, \beta_{13}, \cdots u_{18}, v_{18}, w_{18}, \alpha_{18}, \beta_{18}]^T \tag{15}$$

Under the above conditions, the following equation system exists:

$$[J]=\begin{bmatrix} \frac{\partial x}{\partial \xi} & \frac{\partial y}{\partial \xi} & \frac{\partial z}{\partial \xi} \\ \frac{\partial x}{\partial \eta} & \frac{\partial y}{\partial \eta} & \frac{\partial z}{\partial \eta} \\ \frac{\partial x}{\partial \zeta} & \frac{\partial y}{\partial \zeta} & \frac{\partial z}{\partial \zeta} \end{bmatrix}$$

$$= \begin{bmatrix} \sum_{i=1}^{12} \frac{\partial N_i}{\partial \xi} x_i + \sum_{j=13}^{15} \frac{\partial N_j}{\partial \xi}\left(x_j + \frac{\zeta}{2} V_{3jx}\right) & \sum_{i=1}^{12} \frac{\partial N_i}{\partial \xi} y_i + \sum_{j=13}^{15} \frac{\partial N_j}{\partial \xi}\left(y_j + \frac{\zeta}{2} V_{3jy}\right) \\ \sum_{i=1}^{12} \frac{\partial N_i}{\partial \eta} x_i + \sum_{j=13}^{15} \frac{\partial N_j}{\partial \eta}\left(x_j + \frac{\zeta}{2} V_{3jx}\right) & \sum_{i=1}^{12} \frac{\partial N_i}{\partial \eta} y_i + \sum_{j=13}^{15} \frac{\partial N_j}{\partial \eta}\left(y_j + \frac{\zeta}{2} V_{3jy}\right) \\ \sum_{i=1}^{12} \frac{\partial N_i}{\partial \zeta} x_i + \sum_{j=13}^{15} \frac{1}{2} N_j V_{3jx} & \sum_{i=1}^{12} \frac{\partial N_i}{\partial \zeta} y_i + \sum_{j=13}^{15} \frac{1}{2} N_j V_{3jy} \end{bmatrix}$$

$$\begin{bmatrix} \sum_{i=1}^{12} \frac{\partial N_i}{\partial \xi} z_i + \sum_{j=13}^{15} \frac{\partial N_j}{\partial \xi}\left(z_j + \frac{\zeta}{2} V_{3jz}\right) \\ \sum_{i=1}^{12} \frac{\partial N_i}{\partial \eta} z_i + \sum_{j=13}^{15} \frac{\partial N_j}{\partial \eta}\left(z_j + \frac{\zeta}{2} V_{3jz}\right) \\ \sum_{i=1}^{12} \frac{\partial N_i}{\partial \zeta} z_i + \sum_{j=13}^{15} \frac{1}{2} N_j V_{3jz} \end{bmatrix} \qquad (16)$$

$$= \begin{bmatrix} C_{11} & C_{12} & C_{13} \\ C_{21} & C_{22} & C_{23} \\ C_{31} & C_{32} & C_{33} \end{bmatrix}$$

$$[J]^{-1}=\frac{1}{|J|}\begin{bmatrix} J_{11} & J_{12} & J_{13} \\ J_{21} & J_{22} & J_{23} \\ J_{31} & J_{32} & J_{33} \end{bmatrix}=\begin{bmatrix} A_{11} & A_{12} & A_{13} \\ A_{21} & A_{22} & A_{23} \\ A_{31} & A_{32} & A_{33} \end{bmatrix} \tag{17}$$

where the meaning of [J], |J| and $[J]^{-1}$ are the same as before. $\bar{v}_{ij}$ is the algebraic remaining term of $c_{ji}$.

$$[B]=([B_1],\ \cdots,\ [B_{12}]) \tag{18}$$

where

$$[B_i]=\begin{Bmatrix} A_{11}\frac{\partial N_i}{\partial \xi}+A_{12}\frac{\partial N_i}{\partial \eta}+A_{13}\frac{\partial N_i}{\partial \zeta} & & 0 \\ 0 & A_{21}\frac{\partial N_i}{\partial \xi}+A_{22}\frac{\partial N_i}{\partial \eta}+A_{23}\frac{\partial N_i}{\partial \zeta} & 0 \\ 0 & 0 & A_{31}\frac{\partial N_i}{\partial \xi}+A_{32}\frac{\partial N_i}{\partial \eta}+A_{33}\frac{\partial N_i}{\partial \zeta} \\ A_{21}\frac{\partial N_i}{\partial \xi}+A_{22}\frac{\partial N_i}{\partial \eta}+A_{23}\frac{\partial N_i}{\partial \zeta} & A_{11}\frac{\partial N_i}{\partial \xi}+A_{12}\frac{\partial N_i}{\partial \eta}+A_{13}\frac{\partial N_i}{\partial \zeta} & 0 \\ 0 & A_{31}\frac{\partial N_i}{\partial \xi}+A_{32}\frac{\partial N_i}{\partial \eta}+A_{33}\frac{\partial N_i}{\partial \zeta} & A_{11}\frac{\partial N_i}{\partial \xi}+A_{12}\frac{\partial N_i}{\partial \eta}+A_{13}\frac{\partial N_i}{\partial \zeta} \\ A_{31}\frac{\partial N_i}{\partial \xi}+A_{32}\frac{\partial N_i}{\partial \eta}+A_{33}\frac{\partial N_i}{\partial \zeta} & 0 & A_{11}\frac{\partial N_i}{\partial \xi}+A_{12}\frac{\partial N_i}{\partial \eta}+A_{13}\frac{\partial N_i}{\partial \zeta} \end{Bmatrix}$$

$$(i=1,\ \cdots\cdots,\ 12) \tag{19}$$

$$[B_j] = \begin{pmatrix} A_{11}\frac{\partial N_j}{\partial \xi} + A_{12}\frac{\partial N_j}{\partial \eta} & 0 & 0 \\ 0 & A_{21}\frac{\partial N_j}{\partial \xi} + A_{22}\frac{\partial N_j}{\partial \eta} & 0 \\ 0 & 0 & A_{31}\frac{\partial N_j}{\partial \xi} + A_{32}\frac{\partial N_j}{\partial \eta} \\ A_{21}\frac{\partial N_j}{\partial \xi} + A_{22}\frac{\partial N_j}{\partial \eta} & A_{11}\frac{\partial N_j}{\partial \xi} + A_{12}\frac{\partial N_j}{\partial \eta} & 0 \\ 0 & A_{31}\frac{\partial N_j}{\partial \xi} + A_{32}\frac{\partial N_j}{\partial \eta} & A_{21}\frac{\partial N_j}{\partial \xi} + A_{22}\frac{\partial N_j}{\partial \eta} \\ A_{31}\frac{\partial N_j}{\partial \xi} + A_{32}\frac{\partial N_j}{\partial \eta} & 0 & A_{11}\frac{\partial N_j}{\partial \xi} + A_{12}\frac{\partial N_j}{\partial \eta} \end{pmatrix}$$

$(j = 13, 14, 15)$

$$
\begin{bmatrix}
\left(\frac{t_f}{2}\zeta\left(A_{11}\frac{\partial N_f}{\partial \xi}+A_{12}\frac{\partial N_f}{\partial \eta}\right)+\frac{t_f}{2}N_f A_{13}\right)v_{1f\alpha} & -\left(\frac{t_f}{2}\zeta\left(A_{11}\frac{\partial N_f}{\partial \xi}+A_{12}\frac{\partial N_f}{\partial \eta}\right)+\frac{t_f}{2}N_f A_{13}\right)v_{2f\alpha} \\
\left(\frac{t_f}{2}\zeta\left(A_{21}\frac{\partial N_f}{\partial \xi}+A_{22}\frac{\partial N_f}{\partial \eta}\right)+\frac{t_f}{2}N_f A_{23}\right)v_{1f\beta} & -\left(\frac{t_f}{2}\zeta\left(A_{21}\frac{\partial N_f}{\partial \xi}+A_{22}\frac{\partial N_f}{\partial \eta}\right)+\frac{t_f}{2}N_f A_{23}\right)v_{2f\beta} \\
\left(\frac{t_f}{2}\zeta\left(A_{31}\frac{\partial N_f}{\partial \xi}+A_{32}\frac{\partial N_f}{\partial \eta}\right)+\frac{t_f}{2}N_f A_{33}\right)v_{1f\alpha} & -\left(\frac{t_f}{2}\zeta\left(A_{31}\frac{\partial N_f}{\partial \xi}+A_{32}\frac{\partial N_f}{\partial \eta}\right)+\frac{t_f}{2}N_f A_{33}\right)v_{2f\alpha} \\
\left(\frac{t_f}{2}\zeta\left(A_{21}\frac{\partial N_f}{\partial \xi}+A_{22}\frac{\partial N_f}{\partial \eta}\right)+\frac{t_f}{2}N_f A_{23}\right)v_{1f\alpha} & -\left(\frac{t_f}{2}\zeta\left(A_{21}\frac{\partial N_f}{\partial \xi}+A_{22}\frac{\partial N_f}{\partial \eta}\right)+\frac{t_f}{2}N_f A_{23}\right)v_{2f\alpha} \\
+\left(\frac{t_f}{2}\zeta\left(A_{11}\frac{\partial N_f}{\partial \xi}+A_{12}\frac{\partial N_f}{\partial \eta}\right)+\frac{t_f}{2}N_f A_{13}\right)v_{1f\beta} & -\left(\frac{t_f}{2}\zeta\left(A_{11}\frac{\partial N_f}{\partial \xi}+A_{12}\frac{\partial N_f}{\partial \eta}\right)+\frac{t_f}{2}N_f A_{13}\right)v_{2f\beta} \\
\left(\frac{t_f}{2}\zeta\left(A_{31}\frac{\partial N_f}{\partial \xi}+A_{32}\frac{\partial N_f}{\partial \eta}\right)+\frac{t_f}{2}N_f A_{33}\right)v_{1f\beta} & -\left(\frac{t_f}{2}\zeta\left(A_{31}\frac{\partial N_f}{\partial \xi}+A_{32}\frac{\partial N_f}{\partial \eta}\right)+\frac{t_f}{2}N_f A_{33}\right)v_{2f\beta} \\
+\left(\frac{t_f}{2}\zeta\left(A_{21}\frac{\partial N_f}{\partial \xi}+A_{22}\frac{\partial N_f}{\partial \eta}\right)+\frac{t_f}{2}N_f A_{23}\right)v_{1f\alpha} & -\left(\frac{t_f}{2}\zeta\left(A_{21}\frac{\partial N_f}{\partial \xi}+A_{22}\frac{\partial N_f}{\partial \eta}\right)+\frac{t_f}{2}N_f A_{23}\right)v_{2f\alpha} \\
\left(\frac{t_f}{2}\zeta\left(A_{31}\frac{\partial N_f}{\partial \xi}+A_{32}\frac{\partial N_f}{\partial \eta}\right)+\frac{t_f}{2}N_f A_{33}\right)v_{1f\alpha} & -\left(\frac{t_f}{2}\zeta\left(A_{31}\frac{\partial N_f}{\partial \xi}+A_{32}\frac{\partial N_f}{\partial \eta}\right)+\frac{t_f}{2}N_f A_{33}\right)v_{2f\alpha} \\
+\left(\frac{t_f}{2}\zeta\left(A_{11}\frac{\partial N_f}{\partial \xi}+A_{12}\frac{\partial N_f}{\partial \eta}\right)+\frac{t_f}{2}N_f A_{13}\right)v_{1f\beta} & -\left(\frac{t_f}{2}\zeta\left(A_{11}\frac{\partial N_f}{\partial \xi}+A_{12}\frac{\partial N_f}{\partial \eta}\right)+\frac{t_f}{2}N_f A_{13}\right)v_{2f\beta}
\end{bmatrix}
\tag{20}
$$

Similarly, based on the general expression [1], the mass matrix and load vector of the transition element can be obtained. It is not discussed in detail. 80

## IV. EXAMPLES

Due to the limitation of space, here we only give two examples to show the accuracy and application of this kind of transition element. The analyzed combined structures have unit thickness and were under plane stress situation.

### 1. Transverse force exerted on the end of staircase-shaped cantilever beam

The data of this example are shown in Figure 3(a). The element subdivisions are shown in Figure 4(a) and (b) where (a) used quadratic plane element, plane transition element and plane beam element, and (b) used quadratic plane beam element only. The deflections of line AB calculated using both subdivisions and its analytical solution [13] are all shown in Figure 5.

### 2. Plane fork structures with two concentrated forces

The data of this example are shown in Figure 3(b). Using symmetry, only half of the structure is examined. In this case we can no longer use plane beam elements alone to carry out the analysis. However, the method involving the use of transition elements as shown in Figure 4(a) is still feasible. The calculated deflections of line AB are also shown in Figure 5. Figure 6 shows the horizontal displacements of some cross-sections.

fig 3

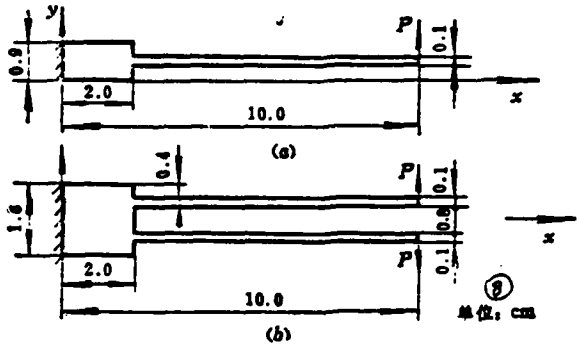


$E = 3 \times 10^7\ kg/cm^2$ $\nu = 0.3$, $P = 500\ kg$

kfig 4

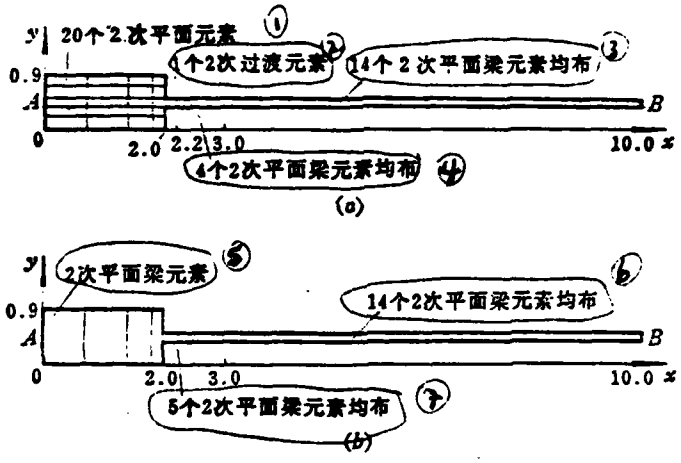


Key: 1--20 quadratic plane elements; 2--one quadratic transition element; 3--14 quadratic plane beam element distributed evenly; 4--four quadratic plane beam element distributed evenly; 5--quadratic plane beam element; 6--14 quadratic plane beam element distributed evenly; 7--5 quadratic plane beam element distributed evenly; 8--unit:cm

fig 5

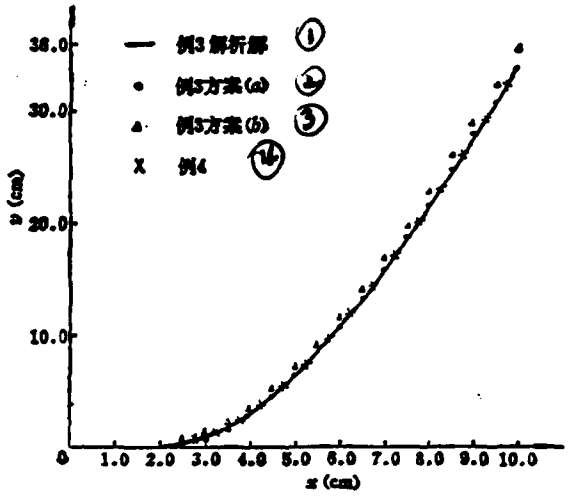


Fig. 5 Deflections of line $\overline{AB}$ in specimens 1 and 2

fig 6

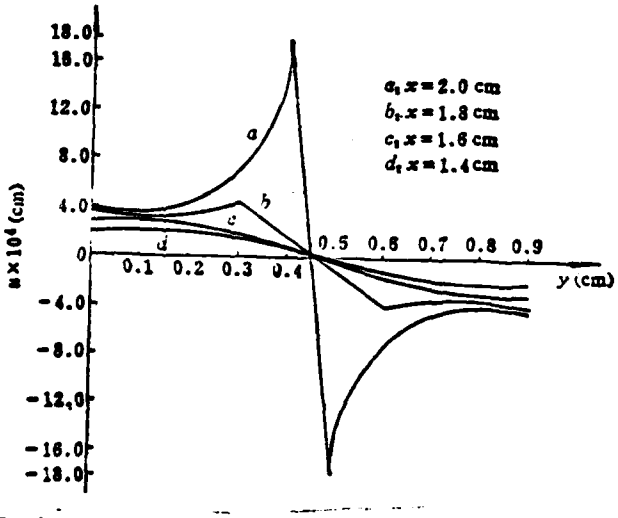


Fig. 6 Horizontal displacements of some sections in specimen 2

Key: 1--analytical solution of example 3; 2--example 3 method (a); 3--example 3 method (b); 4--example 4

REFERENCES


[1] O. C. Zienkiewicz: The Finite Element Method, McGraw-Hill, 1977.

[2] Chun Fongshi: "Design problem of the combined structure analysis program JIGFEX", Mechanics and Realization, vol. 1, no. 3-4, 1979.

[3] Fung Kong: Mathematical Theory of Elastic Structures, Science Publications, 1981.

[4]

[5] N. J. Cubbitt and S. K. Roy, Application of the finite element method to cases requiring the combination of element possessing different numbers of degrees of freedom, Int. Conference on variational methods in engineering, Vol. I. 1972.

[6] Yen Changchu and Tiao Quichiu: "Stress Analysis of the Combination of Shell and Solid", Numerical Analysis and Computer Applications, vol. 1, no. 2, 1980.

[7] K S Surana, Transition finite elements for axisymmetric stress analysis, Int. J. for Num Meth in Engng., Vol. 15, No 6, 1980.

[8] K. S. Surana, Transition finite elements for three-dimensional stress analysis. Int. J. for Num Meth in Engng., Vol. 15, No. 7, 1980.

[9] M. Bakhshandernhpour, Finite element solution for axisymmetric transient thermal stress. AD 747523, 1972.

[10] S. Ahmad, B. M. Irons, and O. C. Zienkiewicz, Analysis of thick and thin shell structures by Curved finite elements. Int. J. for Num. Meth. in Engng. Vol. 2, No. 3, 1970.

[11] S. Ahmad, B. M. Irons and O. C. Zienkiewicz, Curved thick and membrance elements with particular reference to axisymmetric problems. Proceedings of the second conference on matrix methods in structural mechanics, 1968.

[12] O. C. Zienkiewicz, B. M. Irons, J. Ergatoudis, S. Ahmad and F. C. Scott, Isoparametric and associated element families for two- and three-dimensional analysis. in Finite Element Methods in Stress Analysis, edited by I. Holand and K. Bell, Tapir, 1972.

[13] S. Timoshenko, J. Gere, Mechanics of Materials. Von Nostrand Rechhold Com., 1972.

# A KIND OF TRANSITION FINITE ELEMENT FOR ANALYSIS OF SOLID-SHELL OR TENSILE PLATE-PLANE BEAM COMBINED STRUCTURES

*Yin Zeyong, Yin Jing, Ren Peizheng*

(*Nanhua Powerplant Institute*)

Abstract

A kind of transition finite element is developed. In coordinative combination with standard iso-parametric solid (or plane) elements and super-parametric shell (or plane beam) elements of the same order, this kind of transition element can be used to deal with non-standard joint combined structures such as solid-shell or tensile plate-plane beam structures.

The procedure to develop this kind of transition element is as follows. On an interface or an edge of a standard iso-parametric solid element or on a boundary line of a standard iso-parametric plane element, the corresponding nodes of a super-parametric shell (or plane beam) element of the same order are placed instead of the nodes of the original solid (or plane) element. The shape functions for remained solid (or plane) element type nodes are the same as the corresponding ones for a standard iso-parametric solid (or plane) element. As regards shell (or plane beam) element type nodes the same shape functions are adopted as for a standard super-parametric shell(or plane beam) element.

The formulation of equations for the quadratic transition element is presented in detail.

The numerical results obtained have shown that this kind of transition finite element is very effective.

# PATTERNS OF MONOPULSE ARRAYS WITH TRIANGULAR AMPLITUDE DISTRIBUTION

Beijing Institute of Aeronautics and Astronautics, Liu Shanwei

ABSTRACT

This paper discuses the sum and difference pattern function of monopulse arrays of equally spaced discrete elements. The excitation amplitudes include uniform, triangular and V shaped distributions. The compact form of array factor expression (4), $S(z)=F(z)-G(z)$ has been obtained by other people using either exact or truncated Z-transform. With the aid of equation (8), and sometimes taking the shifting theorem into account, S(z) can be found simply by the unilateral Z-transform without considering whether the envelope function is symmetrical or asymmetrical. A numerical example was also given. A study was carried out with respect to the sum pattern. In the major region, the calculated results agreed very well with the experimental data. The difference pattern has also been verified experimentally.



## I. Z-TRANSFORM AND ARRAY FUNCTION

In the early 1960's, D. K. Cheng and M. T. Ma for the first time successfully applied the Z-transform for treating the time-space problems to the pulse-data system in the analysis of discrete array patterns and expanded the applications of Z-transform theory. Several relevant papers were published later [2,3,4]. In this section, the derivation of array function is further simplified.

As is commonly known, the linear array factor of equally spaced linearly varying excitation phase radiation elements can be written as:

$$S=\sum_{i=0}^{n-1} I_i \exp[jikd(\cos\theta-\cos\theta_0)]=\sum_{i=0}^{n-1} I_i z^{-i} \qquad (1)$$

$$z=\exp(-ju) \qquad (2)$$

$$u=kd(\cos\theta-\cos\theta_0) \qquad (3)$$

where $k=2\pi/\lambda$ ($\lambda$ is the wavelength in free space ); d is the distance between neighboring radiation elements; $j=\sqrt{-1}$, $\theta$ is the angle from the linear array axis, $\theta_0$ is the maximum radiation direction;

$I_i = f(id)$, $(i = 0, 1, \cdots, n-1)$ is the excitation amplitude; n is the total number of radiation elements; $f(\zeta)$ is the envelope function of excitation amplitude.

In equation (1) there are n terms which is also called an array polynominal. It can be rewritten as:

$$S(z) = \sum_{i=0}^{n-1} f(id) z^{-i} \tag{4a}$$

$$= F(z) - G(z) \tag{4b}$$

where

$$F(z) = \sum_{i=0}^{\infty} f(id) z^{-i} = Z[f(\zeta)] \tag{5}$$

---

received in January 1981

$$G(z) = \sum_{i=n}^{\infty} f(id) z^{-i} = Z[f(\zeta) U(\zeta - nd)] \tag{6}$$



$$U(\zeta - nd) = \begin{cases} 1, & \zeta \geqslant nd \\ 0, & \zeta < nd \end{cases} \tag{7}$$

F(z) and G(z) are the Z-transforms of two functions and $U(\zeta - nd)$ is the shifted unit-step function of displacement. Because the exponent (n-1) of $\Sigma$ in equation (4a) is a finite number, therefore, S(z) is called the finite Z transform of $f(\zeta)$

The ordinary Z transform of $f(\zeta)$ in equation (4b) is F(z) which is easy to locate in the theory and tables introduced in ordinary reference books [5,6]. Therefore, the key to finding S(z) is to obtain G(z). It can be proved that when $\zeta \geqslant 0$ G(z) has the following relation:

$$G(z) = Z[f(\zeta) U(\zeta - nd)] = z^{-n} Z[f(\zeta + nd)] \tag{8}$$

Thus, it is possible to obtain the expression G(z) from equation (8). It is equal to the Z-transform of the function $f(\zeta + nd)$ multiplied by $z^{-n}$. This physical meaning of equation (8) is obvious which is the Z-transform of the function $f(\zeta + nd)$ after a displacement of nd. Therefore, it is possible to conveniently obtain G(z) using the unilateral Z-transform and shifting theorem.

## II. SUM AND DIFFERENCE PATTERNS OF TRIANGULAR AMPLITUDE EXCITATION ARRAY

The distribution of the triangular amplitude excitation is shown in Figure 1. Figure 1(a) is sum excitation, and Figure 1(b) is difference excitation. The units are distributed evenly on the $\zeta$ axis at a distance d. We assumed the total number of element n is even, the array function is obtained using equations (4)-(8). 85

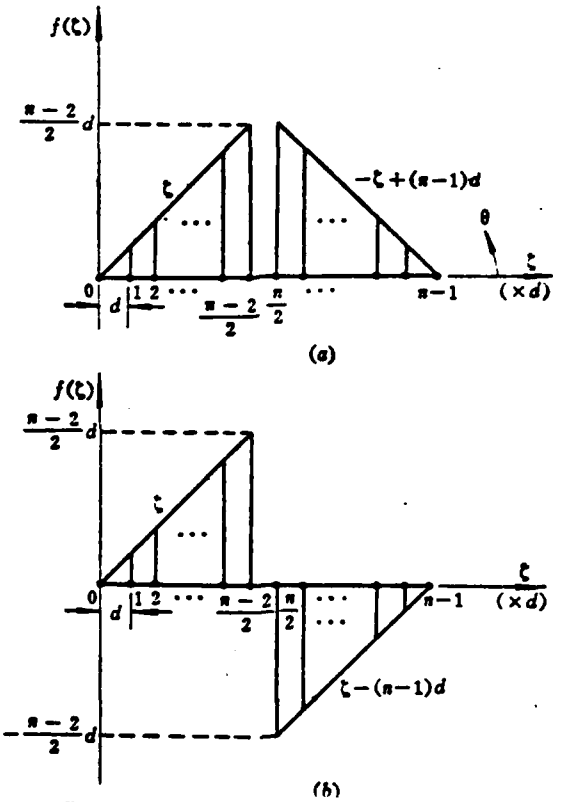


Fig.1 Triagular amplitude distribution for even n
(a) sum, (b) difference.

The truncated Z transform of the left half of the array function in Figure 1 is $S_L(z)$ and the truncated Z-transform of the right half from $\zeta+(n-1)d$ is $S_R(z)$, i.e.,

$$S_L(z)=Z[\zeta]-z^{-\frac{n}{2}}Z\left[\zeta+\frac{n}{2}d\right]$$

$$=dz\left[1-\frac{n}{2}z^{-\frac{n}{2}+1}+\left(\frac{n}{2}-1\right)z^{-\frac{n}{2}}\right]\Big/(z-1)^2 \quad (9)$$

$$S_R(z)=z^{-\frac{n}{2}}Z\left[-\zeta+\frac{n-2}{2}d\right]-z^{-(n-1)}Z[-\zeta]$$

$$=dz\left[\frac{n-2}{2}z^{-\frac{n}{2}+1}-\frac{n}{2}z^{-\frac{n}{2}}+z^{-(n-1)}\right]\Big/(z-1)^2 \quad (10)$$

$S_L(z)+S_R(z)=S_\Sigma(z)$ is the sum excitation array function;
$S_L(z)-S_R(z)=S_\Delta(z)$ is the difference array function. By substituting equations (9) and (10) into them and after rearranging, we get

$$S_\Sigma(z)=dz(1-z^{-n/2})[1-z^{-(n-2)/2}]/(z-1)^2 \quad (11)$$

$$S_\Delta(z)=dz[1+(n-1)(1-z)z^{-n/2}-z^{-(n-1)}]/(z-1)^2 \quad (12)$$

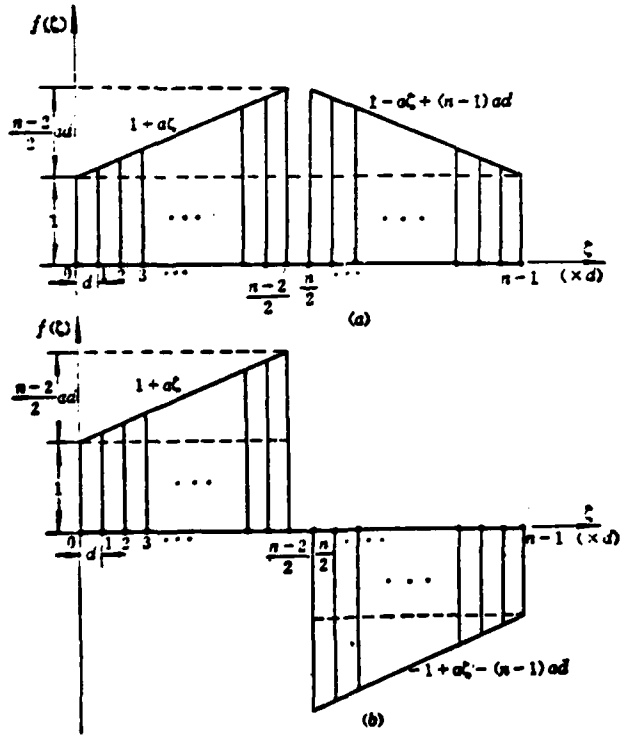


Fig. 2 Triangular amplitude distribution superimposed on uniform basis (a) sum; (b) difference.

Using a similar method, we can obtain the array function of an even number radiation element linear array spaced by d as shown in Figure 2 when the excitation amplitudes are uniform and triangular addition. 86

In the case of sum excitation (Figure 2a)

$$S_\Sigma(z)=z\left[\frac{1-z^{-n}}{z-1}+\frac{ad(1-z^{-n/2})(1-z^{-(n-2)/2})}{(z-1)^2}\right] \tag{13}$$

In the case of difference excitation (Figure 2b)

$$S_\Delta(z)=z\left[\frac{(1-z^{-n/2})^2}{z-1}-\frac{ad[(n-1)(z^{-n/2+1}-z^{-n/2})+z^{-n+1}-1]}{(z-1)^2}\right] \tag{14}$$

It is obvious that the maximum value of equation (13) occurs at $z=1$ (or $u=0$),

$$S_{\Sigma m}(z)=S(1)=\lim_{z\to 1}S_\Sigma(z)=\frac{Q_1''(1)}{Q_2''(1)}=n\left[1+\frac{ad(n-2)}{4}\right] \tag{15}$$

where $Q_1$ and $Q_2$ represent the numerator and denominator of $S_\Sigma(z)$ respectively. $Q_1''$ and $Q_2''$ are the second order derivatives of $Q_1$ and $Q_2$. When z = 1, equation (14) is equal to zero, i.e., $S_\Delta(1)=0$. .

For ease of application, it is customary to further simplify S(z) and the $z=\exp(-ju)$ in equation (2) is substituted and restored as a function of u. Through the simplification of equation (13), and omitting the common factor term $z^{-(n-1)/2}$ which represents the phase center position of the far away region of the array, the expression of sum pattern S(u) can be obtained:

$$S(u)=\frac{\sin\frac{nu}{2}}{\sin\frac{u}{2}}\left[1+\frac{ad\sin\frac{n-2}{4}u}{2\sin\frac{u}{2}\cos\frac{nu}{4}}\right] \tag{16}$$

$$=\frac{\sin\frac{nu}{4}}{\sin\frac{u}{2}}\left[2\cos\frac{nu}{4}+\frac{ad\sin\frac{n-2}{4}u}{\sin\frac{u}{2}}\right] \tag{17}$$

If the array is formed by the same radiation elements, the actual array pattern is the product of the above equation and the element pattern. For example, the array corresponding to equation (16) is formed by half wave oscillator coaxial array with a pattern:

$$F_0(u)=\frac{\cos\frac{\pi u}{2kd}}{\sqrt{1-\left(\frac{u}{kd}\right)^2}} \tag{18}$$

Let us choose n = 14, ad = $\frac{1}{6}$, then the array sum pattern becomes:

$$S_1(u)=\left(\frac{\sin 7u}{\sin\frac{u}{2}}+\frac{\sin 3u\sin\frac{7u}{2}}{6\sin^2\frac{u}{2}}\right)\frac{\cos\frac{\pi u}{2kd}}{\sqrt{1-\left(\frac{u}{kd}\right)^2}} \tag{19}$$

The maximum radiation value is

$$S_{1max}=S_{max}=S(0)=21 \tag{20}$$

In Figure 3 we obtained the calculated results from equation (19) and the experimental results. The dotted line in the figure is based on calculated results. The solid line is the pattern obtained from the x band rectangular wave width longitudinal half wave crack array. Its excitation form is as shown in Figure 2(a). The comparison of calculated and measured results showed that in the major region the two basically coincide. The half power wave band width is very close which is about $2\Delta\theta\approx 5.81^\circ$ . In the visible region of $\theta = 0\sim\pi$ ($|\pm u|\leqslant 251.82^\circ$) 87 the calculated zero point, side lobe position and relative voltage are as follows:

| | |
|---|---|
| 0 point position | $u_0\approx\pm 30.92,\ \pm 51.43,\ \pm 78.94,\ \pm 102.86,\ \pm 129.28,\ \pm 154.29.$ $\pm 180.00,\ \pm 205.71,\ \pm 230.73,\ \pm 251.82;$ |
| side lobe position | $u_1\approx\pm 40,\ \pm 64,\ \pm 90,\ \pm 115,\ \pm 141,\ \pm 167,\ \pm 192,\ \pm 217,\ \pm 241;$ |
| relation voltage of the side lobes | $\approx -0.09751,\ +0.08944,\ -0.05087,\ +0.04599,\ -0.03437,$ $+0.02992,\ -0.02485,\ +0.01871,\ -0.01172.$ |

According to equation (14), after simplification we can obtain the difference pattern of the excitation array with a shape as in Figure 2(b) using u as the independent variable:

$$D(u)=\left[2\sin^2\frac{\pi u}{4}+ad\left(\frac{n-2}{2}-\frac{\sin\frac{n-2}{4}u\cos\frac{\pi u}{4}}{\sin\frac{u}{2}}\right)\right]\Big/\sin\frac{u}{2} \tag{21}$$

Still using n = 14 and ad = $\frac{1}{6}$ to substitute into equation (24), we get

$$D_1(u)=\left[1+2\sin^2\frac{7u}{2}-\frac{\sin 3u\cos\frac{7u}{2}}{6\sin\frac{u}{2}}\right]\Big/\sin\frac{u}{2} \tag{22}$$

$$D_t(0)=\lim_{u\to 0}D_t(u)=0 \tag{23}$$

The results calculated from equation (22) are plotted in Figure 4 Only the region where $u \geqslant 0$ is drawn. The region in which $u<0$ appears to be antisymmetric. The validity of the equations have been verified.

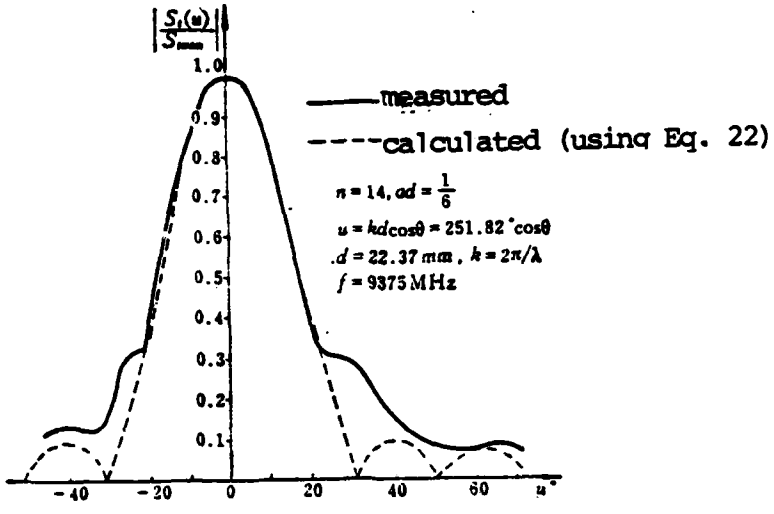


Fig.3 Comparison of measured result with calculated curve on radiation pattern at 9375MHz of 14-element linear array

## III. SUM PATTERNS OF INVERTED TRIANGLE/OR V SHAPED AMPLITUDE EXCITATION ARRAY

Based on the method introduced in the first section, we can derive the array function of the inverted triangular excitation as shown in Figure 5, i.e., the sum pattern.

When n is an odd number

$$S_s(z)=adz\left[\frac{n-1}{2}(z+z^{-n})-\frac{n+1}{2}(1+z^{-n+1})+2z^{-(n-1)/2}\right]\Big/(z-1)^2 \tag{24}$$

When n is an even number

$$S_s(z)=adz\left[\frac{n-1}{2}(z+z^{-n})-\frac{n+1}{2}(1+z^{-n+1})+(1+z)z^{-n/2}\right]\Big/(z-1)^2 \tag{25}$$

Changing the variable to u, and omitting the terms with the absolute value of the common exponent equal to 1, equations (24) and (25) then are transformed into:

$$S_s(u)=\frac{ad}{2\sin^2\frac{u}{2}}\left(n\sin\frac{nu}{2}\sin\frac{u}{2}-2\sin^2\frac{nu}{4}\cos\frac{u}{2}-2\sin^2\frac{u}{4}.\right) \tag{26}$$

$$S_s(u)=\frac{ad}{2\sin^2\frac{u}{2}}\left(n\sin\frac{nu}{2}\sin\frac{u}{2}-2\sin^2\frac{nu}{4}\cos\frac{u}{2}\right) \quad \begin{matrix} n=\text{odd} \\ n=\text{even} \end{matrix} \tag{27}$$

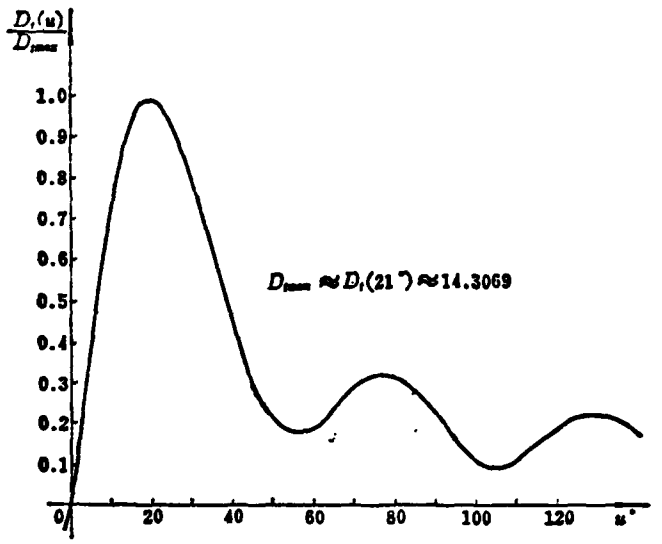


Fig. 4 Calculation of difference for $n = 14$, $ad = \frac{1}{6}$

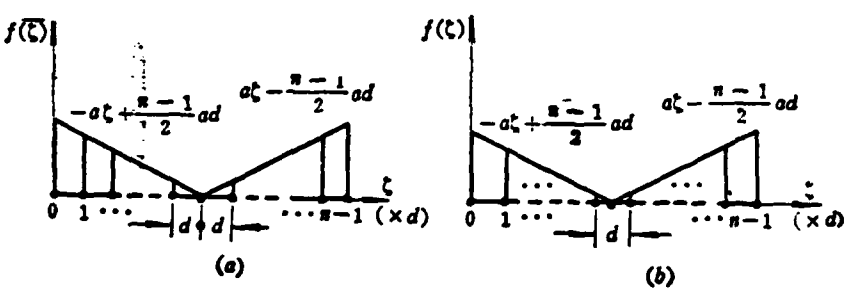


Fig.5 Linear array with V amplitude distribution
(a) n—odd, (b) n—even.

It is obvious that when u = 0, the radiation has its maximum

$$S_{e\max}=S_e(0)=\lim_{u\to 0}S_e(u)=\frac{ad}{4}(n^2-1) \tag{28}$$

$$S_{e\max}=S_e(0)=\lim_{u\to 0}S_e(u)=\frac{ad}{4}n^2 \tag{29}$$

when $n\gg 1$ , $S_{e\max}\approx S_{e\max}=adn^2/4$ . Naturally, the same results can be obtained using equations (24) and (25).

The difference excitation corresponding to the V-shaped sum excitation as shown in Figure 5 has a linear amplitude distribution. The array function (i.e. difference pattern) obtained agrees with that in [4] and will not be repeated here.

We hereby express our indebtedness to Prof. Song Lichuan and Asst. Prof. Mao Shiyi who went over the first draft of this paper.

REFERENCES

[1] D.K. Cheng and M.T. Ma, A New Mathematical Approach for Linear Array Analysis, IRE Trans. Antennas and Propagat., Vol. AP-8, No. 3, May 1960, pp. 255-259.

[2] P.L. Christiansen, On the Closed Form of the Array Factor for Linear Arrays, IEEE Trans. Antennas and Propagat., Vol. AP-11, No. 2, March 1963, pp. 198.

[3] D.K. Cheng, Z-Transform Theory for Linear Array Analysis, IEEE Trans. Antennas and Propagat., Vol. AP-11, No. 5, September 1963, pp. 593.

[4] M.T. Ma, Theory and Application of Antenna Arrays, 1974, pp. 24-37.

[5] E.I. Jury, Theory and Application of the Z-Transform Method, 1964, pp. 3-5, 254-258.

[6] Cheng Chuin, translated by Mao Pei far, Analysis of Linear Systems, 1979 Chinese translation, pp-331-341.

# PATTERNS OF MONOPULSE ARRAYS WITH TRIANGULAR AMPLITUDE DISTRIBUTION

*Lü Shanwei*

*(Beijing Institute of Aeronautics and Astronautics)*

Abstract

This paper describes the sum and difference patterns of monopulse linear arrays of equally spaced discrete inphase elements which are excited in such a way that the envelope of the excitation amplitudes is uniform, triangular, or V in shape. Analysis of the radiation patterns is carried out by using exact or truncated Z-transform, and then the compact form as $S(z)=F(z)-G(z)$, i. e. Eq. ( 4 ), is obtained. This method was first developed by D. K. Cheng and M. T. Ma in 1960. With the aid of Eq. ( 8 ) or the formula of $G(z)$ derived from the shifting theorem, $S(z)$ can be found simply by the unilateral Z-transform without considering whether the envelope function is symmetrical or unsymmetrical. Also a numerical example is given, showing that the theoretically calculated sum pattern compares quite favorably with that obtained from experiments, especially in the major region the test data and the analytical results have been found in fairly satisfactory agreement. The difference pattern also has been checked by experiments. The method proposed here is simple and easy to carry out.

# MODIFICATION OF THE WILLENBURG AND MAARSE MODELS AND APPLICATION TO THE LIFE PREDICTION FOR Ti-6Al-4V ALLOY

89

Beijing Aeronautical Materials Research Institute,
Zhang Yongkui, Gu Mingda and Yan Minggo

## ABSTRACT

The accuracy of the overload retardation effect on fatigue crack growth is closely related to the formula for the plastic zone chosen in the retardation model. Hence, this paper proposed a corrected plastic zone formula to replace those in the Willenborg and Maarse models. In addition, the material constants C* and n* processed by the $\Delta_{Keff}$ treatment using the Maarse model were replaced by the constant amplitude material constants C and n in the computation. Through the calculation of the overload retardation effect of Ti-6Al-4V titanium plate, the improved model shown in this paper demonstrated that it not only has significantly higher accuracy than the original models but also is convenient to use.

## I. INTRODUCTION

The calculation of overload retardation effect in fatigue crack growth is one of the important problems of crack growth life prediction under spectrum loads. Hence, we have carried out experimental studies on overload retardation characteristics of Ti-6Al-4V titanium plate under various overload ratios and various crack lengths. In addition, the Wheeler model, Willenborg model, Matsuoka model and Maarse model were chosen to calculate retardation effect quantitatively. Comparisons and evaluation of the above four retardation models were also carried out [1]. The study results indicate:

(1) the fatigue crack growth form of the titanium plate under test was primarily plane strain or a mixed model primarily with plane strain;

(2) the accuracy of the Maarse model and Willenborg was more inferior;

(3) the selection of the formula in the plastic zone has a very significant effect on the estimation of the retardation effect.

As is well known, the overload plastic zone is one of the important factors controlling the retardation effect. The commonly used formula for the dimension of the plastic zone is [2]:

$$R_p = \frac{1}{\alpha\pi}\left(\frac{K}{\sigma_\mu}\right)^2 \qquad (1)$$

where $\alpha$ is a constant: Under plane stress condition, $\alpha = 2$; under plane strain condition, $\alpha = 6$.

In reality, the specimens seldom were found in ideal plane stress or plane strain conditions. More of them are situated in between--mixed type stress state. Especially for specimens or structures during service, along with the growth of the crack, the stress condition varied continuously from plane strain → mixed type → plane stress. Therefore, the use of a fixed constant $\alpha$ to calculate the dimension of the plastic zone $R_p$ under varying stress conditions would definitely cause larger errors.

Received June 1981.



Hence, in order to reflect the characteristics of the fatigue growth process and the continuity of the stress state transformation process, and to further improve the prediction accuracy of the retardation model, we made attempts to improve the Willenborg and Maarse models by correcting the plastic zone dimension formula.

## II. IMPROVEMENT FOR WILLENBORG RETARDATION MODEL

In the Willenborg model [3], the effective stress intensity factor region $\Delta_{Keff}$ and effective stress ratio $\Delta_{Reff}$ were adopted. Because of ease of use, it has received wide attention. However, to further improve the accuracy of the Willenborg model for the prediction of overload retardation effect, several researchers used different angles to carry out the improvement work and obtained relatively more satisfactory results [4-6]. The improvement of the Willenborg model in this paper is limited to the corrective computation of the constant $\alpha$ in the adopted plastic zone dimension formula (1).

As is well known, for a given material the change of stress condition during crack growth is mainly dependent upon the variations of the stress intensity factor region $\Delta K$ and the stress ratio R. Hence, when $\Delta K$ is very small or approaching the threshold value $\Delta K_{th}$, it can be considered in a plane strain state and the $\alpha$ in equation (1) should be 6. When $\Delta K$ is very large or very close to $\Delta K_o$ (i.e., $K_{max}$ is very close to $K_o$), it can be considered in a plane stress state and the $\alpha$ should be 2 in equation (1). The intermediate section is in a mixed stress state and the $\alpha$ should be a fixed function of $\Delta K$. Therefore, we can assume that when the stress relaxation condition is not considered

$$\alpha = \frac{6}{1+2S} \tag{2}$$

where $K_o$ is the fracture modulus.

$$S = \frac{\Delta K - \Delta K_{th}}{\Delta K_e} = \frac{(1-R)K_{max} - \Delta K_{th}}{(1+R)K_e}$$

$$S = \frac{K_{max} - \frac{\Delta K_{th}}{(1-R)}}{K_e} \tag{3}$$

where $K_o$ is the fracture modulus.

Equations (1), (2) and (3) are the improved plastic zone calculation formula of Willenborg model. Obviously, $\alpha$ is no longer a fixed constant; it is a function of $K_{max}$ and R.

The physical meaning of S can be envisioned as the ratio of plane stress. From equations (2) and (3), we get:

under plane strain, $\Delta K$ is small or $\Delta K \to \Delta K_{th}$,

$$S \to 0, \quad \alpha \to 6$$

under plane stress, $\Delta K$ is large or $K_{max} \to K_o$,

$$S \to 1, \quad \alpha \to 2$$

In mixed stress conditions, $0 < S < 1$, $2 < \alpha < 6$.

In order to verify the validity of equation (3), an example is given here. The experimental data were taken from [7]; the material used was 3.2 mm thick 2024-T3 aluminum alloy plate. The experimental data, as well as the numerical results S obtained from equation (3) are tabulated in Table 1. From Table 1, it can be concluded that the

numerical values S calculated using equation (3) are relatively close to the average values $S_E$ of the actual measurement. 9-3

Table 1 Comparison between the calculated S and the tested $\bar{S}_E$ in a 2024-T3 aluminum-alloy

| ① 试验组编号 | $\Delta K_{OL}$ MPa$\sqrt{m}$ | ② 超载循环应力比 $R_{OL}$ | $K_c$ [8] MPa$\sqrt{m}$ | $\Delta K_{th}$ [9] MPa$\sqrt{m}$ | 疲劳断口上剪唇口(剪切型)所占比例的实测平均值$\bar{S}_E$ [7] ③ | 计算值 ④ $S=\frac{\Delta K_{OL}-\Delta K_{th}}{(1-R_{OL})K_c}$ |
|---|---|---|---|---|---|---|
| Ⅰ, Ⅴ | 24.7 | 0.03 | 88.0 | 3.4 | 0.26 | 0.25 |
| Ⅱ | 24.7 | 0.21 | 88.0 | 2.8 | 0.34 | 0.32 |
| Ⅲ | 24.7 | 0.57 | 88.0 | 1.7 | 0.67 | 0.61 |

Key: 1--experimental group number; 2--overload cyclic stress ratio; 3--average measured value $S_E$ of the ratio of slanted cracks shear type) in fractured cracks; 4--calculated value

## III. IMPROVEMENT FOR MAARSE RETARDATION MODEL

Maarse model [10] is based on the crack closure theory and its basic equation is

$$\frac{da}{dN}=C^*(\Delta K_{eff})^{n^*}=C^*(K_{max}-K_{op})^{n^*} \tag{4}$$

where $K_{op}$ is the opening stress intensity factor corresponding to the crack opening load $P_{op}$. Maarse used the "residual pressure stress crack negative opening displacement" assumption to propose an engineering method to predict $P_{op}$, i.e.,

$$P_{op}=C_e\frac{R_{YCB}}{f\left(\frac{a}{W}\right)(a_s-a)^{1/2}} \tag{5}$$

where

$$C_e=\frac{\sigma_{ys}\cdot B(2\pi W)^{1/2}}{8(1-\nu^2)} \qquad \text{(plane strain)}$$

where B and W are the thickness and width of the specimen respectively; $f\left(\frac{a}{W}\right)$ is a relevant function of the crack length and specimen geometric shape in the expression of stress intensity factor; $(a_s-a)$ is the length in the x direction in the residual plastic compression zone; $R_{YCB}$ is twice the measured distance from the crack tip to the plastic compression boundary along the Y direction (Figure 1).

The use of Maarse model to estimate the effect of overload retardation has two inconvenient points: one is that the material constants C* and n* in equation (4) must first be treated according to $\Delta_{Keff}$ and the other is that the calculation under mixed type and stress conditions was not given in the original paper.

With respect to the above two points, we attempted to make simplifications and additions for the Maarse model in this paper.

## 1. Simplification of the calculation of C* and n*

The Paris equation to calculate the rate of crack growth under constant amplitude is

$$\frac{da}{dN} = C(\Delta K)^n = C[K_{max}(1-R)]^n \qquad (6)$$

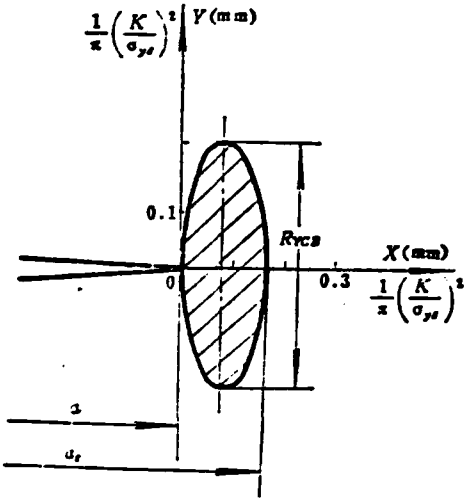


Fig. 1 Residual plastic zone geometry and location ellipse

$$\left(\frac{X-0.348}{0.088}\right)^2 + \left(\frac{Y}{0.224}\right)^2 = 1$$

If we assume that the crack closure stress and opening stress are equal, and define that the closure factor C is

$$C_f = \frac{P_{op}}{P_{max}} = \frac{K_{op}}{K_{max}} \qquad (7)$$

then the Maarse equation (4) used to calculate da/dN can be rewritten as:

$$\frac{da}{dN} = C^*[K_{max}(1-C_f)]^{n^*} \qquad (8)$$

Based on the experimental results in [11], equation (6) at different R is a series of approximately parallel lines with difference intercepts in the $\frac{da}{dN}$ $\Delta K$ log-log coordinate system. This means that the change of the exponent n is very small. Hence, it can be assumed that

$$n^* = n \qquad (9)$$

In fact, for the same condition regardless of the expression, the crack propagation speed is the same. Then equation (6) should be equal to equation (8):

$$C[K_{max}(1-R)]^n = C^*[K_{max}(1-C_f)]^n$$

$$C^* = C\left(\frac{1-R}{1-C_f}\right)^n = C\left[\frac{1-R}{1-\left(\frac{P_{op}}{P_{max}}\right)}\right]^n \qquad (10)$$

In the process of additive calculation of crack expansion, it is

possible to let the initial $P_{op} = 0$. The $P_{op}$ in other stress cycles can be computed based on equation (5).

Thus, after the simplification through equations (9) and (10), C* and n* can be calculated using the material constants C and n in equation (6). Consequently, the application of engineering predictions of crack propagation life is becoming more convenient.

## 2. The extension of residual plastic zone compressible ellipse equation

In the Maarse model, $R_{YCB}$ is an important parameter in the calculation of $P_{op}$. However, in the original paper only the ellipse equation determining $R_{YCB}$ under plane strain conditions was given which limited the application of this model.

In this paper we attempted to extend the original ellipse equation to more general conditions, including plane strain, mixed type and plane stress conditions. The adopted method is the corrected equation of the plastic zone dimension described in the previous section of this paper, i.e.,

$$(a_i - a) = R_p = \frac{1}{\alpha\pi}\left(\frac{K}{\sigma_{ys}}\right)^2 \tag{11}$$

$\alpha$ is calculated based on equations (3) and (2). Thus, the ellipse equation in the original model is replaced by the following equation:

$$\left(\frac{X - \frac{1}{2\alpha}}{\frac{1}{2\alpha}}\right)^2 + \left(\frac{Y}{0.234}\right)^2 = 1 \tag{12}$$

## IV. CALCULATED RESULTS AND DISCUSSIONS

In this paper the overload retardation effect was calculated using the additive method in combination with improved Willenborg model and Maarse model to predict the crack propagation behavior in Ti-6Al-4V titanium plate overloading equipment. The results were compared with those of original corresponding models and experimental results [1].

The relevant data for the computation are the following: The specimen is 300x100x2 mm of the center crack tensile (CCT) type, the basic cyclic stress ratio $R=P_{min}/P_{max}=$ 1.6kN/16.0kN=0.1; 94/95 the yield stress of the material $\sigma_{y.}$=917.0MPa; $K_c$=115.4MPa$\sqrt{m}$[12], $\Delta K_{th}$ =6.5MPa$\sqrt{m}$[13] ; the material constants C and n are listed in Table 2 (in Paris equation, $\Delta K > 13.5$ MPa$\sqrt{m}$); Poisson ratio $\nu$=0.33.

Table 2 Material constants in FCG for Ti-6Al-4V

| computational equation | C | n |
|---|---|---|
| $\frac{da}{dN}=C(\Delta K)^n$ | $1.341\times10^{-7}$ | 2.515 |
| $\frac{da}{dN}=\frac{C(\Delta K)^n}{(1-R)K_c-\Delta K}$ | $2.048\times10^{-6}$ | 2.311 |

Figure 2 shows the predicted retardation cycle number and measured number $N_D$ using both improved and original Willenborg and Maarse models (overload ratio $Q_{OL}=P_{OL}/P_{max}=1.8$) under a single tensile overload). Figure 2 also shows the variation of α before and after the improvement. It is obvious that the corrected α value is adjusted automatically (without the need of making a selection beforehand) based on the variation of the overload level $K_{OL}$ between the original constant values of 6∿2. This advantage may be more significant in the prediction of crack propagation life under complex spectrum loads.

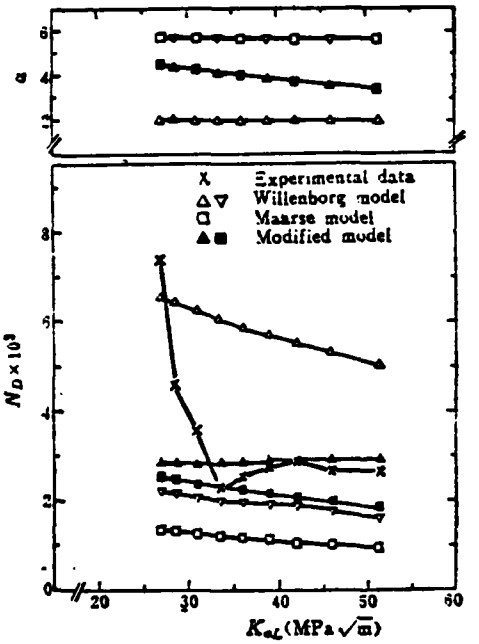


Fig. 2 Coefficient α and number of delay cycles $N_D$ versus $K_{OL}$ for Ti-6Al-4V alloy ($Q_d$=1.8)

It is also possible to see from Figure 2 that the calculated $N_{D,cal}$ values of plane stress (Δ in Figure 2) and plane strain (∇ in Figure 2) using the Willenborg model deviated highly from the actually measured value $N_{D,E}$. The former was shifted toward danger and the latter toward safety. The improved Willenborg model predication (in Figure 2)

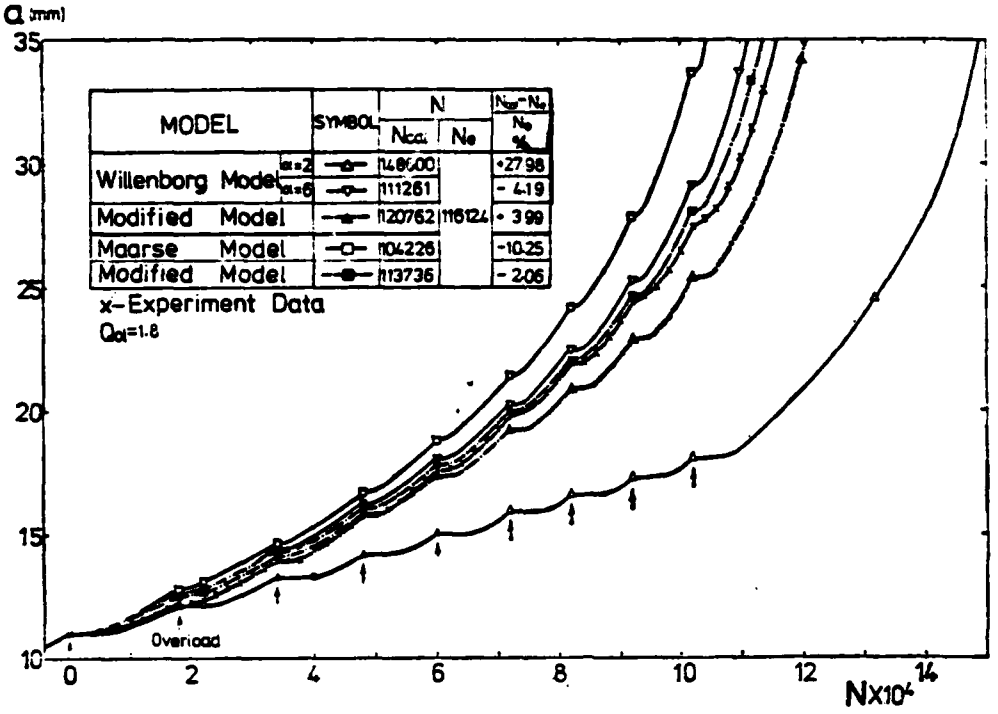


Fig. 3 The experimental curve ( $a-N$ ) and predictedcurves various models under a series of single tensile overloads at $Q_{OL}=1.8$

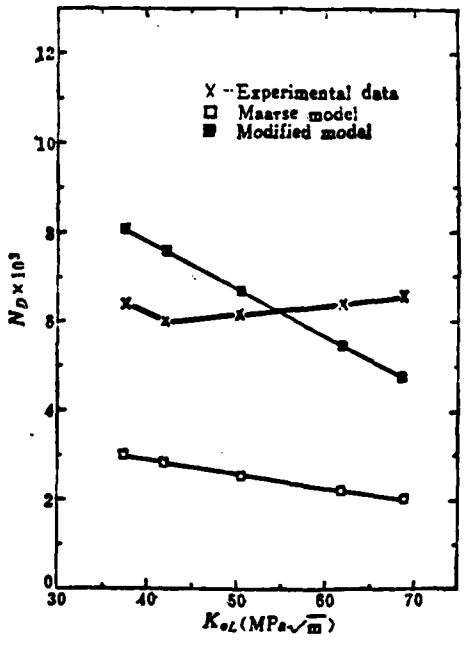


Fig. 4 Comparison between predicted results and experimental data of $N_D$ ($Q_{OL}=2.0$)

Table 3 Comparison of predicting accuracy of modified models with original models

| 误差值 ① | Willenborg模型 ② 平面应力 α = 2 ③ | Willenborg模型 ② 平面应变 α = 6 ④ | 改进后的 ⑤ Willenborg模型 | Maarse 模型 ⑥ | 改进后的Maarse模型 ⑦ |
|---|---|---|---|---|---|
| $\frac{\Sigma N_{D1} C_{al}}{\Sigma N_{D,E}}$ (估算平均值与实测平均值) ⑧ | 1.67 | 0.53 | 0.83 | 0.37 | 0.83 |
| $\frac{N_{Cal} - N_e}{N_e}$ (相对误差) ⑨ | +27.98% | -4.19% | +3.99% | -10.25% | -2.06% |

Key: 1--error; 2--Willenborg model; 3--plane stress; 4--plane strain; 5--improved Willenborg model; 6--Maarse model; 7--improved Maarse model; 8--(predicated average value and measured average value); 9--relative error

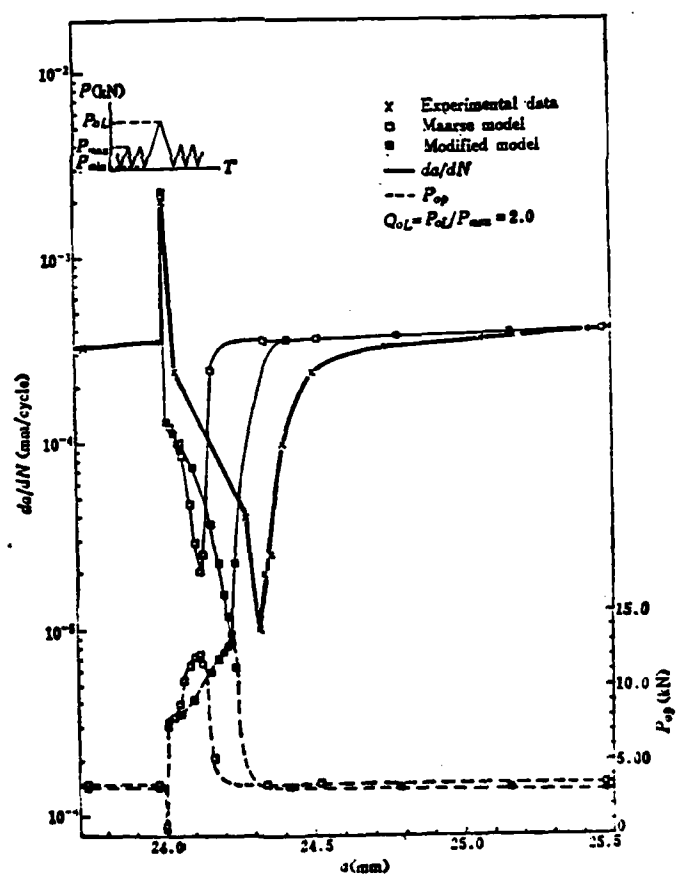


Fig. 5 $\frac{da}{dN}$ vs a and $P_{eq}$ vs a curves in a single tensile overload retardation zone for Ti-6Al-4V alloy

however, was located in between the above results.

The calculated a-N curves of crack propagation under multiple single tensile overload based on the improved and original Willenborg and Maarse models as well as the measured a-N curve were all plotted in Figure 3.

Figure 4 also shows the calculated and measured values of the improved and original Maarse model when $Q_{OL} = 2.0$.

Summarizing Figures 2, 3 and 4, the computational accuracies of the above models before and after the improvement are listed in Table 3.

The $N_e$ and $N_{cal}$ in Table 3 represent the measured and calculated number of load cycles necessary to propagate a crack with a half length a = 11 mm to 35 mm.

Apparently, from Table 3, the accuracy of the improved Willenborg model is significantly higher than that of the original model and its absolute error is minimal. Similarly, the improved Maarse model has a higher prediction accuracy than that of the original model with more satisfactory results.

For further comparison and exploration, Figure 5 plots the retardation characteristics of crack propagation under single tensile overload: $\frac{da}{dN}$ - a vs. $P_{op}$ - a curve. From Figure 5, during the variation of the external load P from low-high-low, the variation of crack opening load $P_{op}$ as described by the Maarse model which is based on the crack closure effect and the corresponding $\frac{da}{dN}$ is shown. When the peak load $P_{OL}$ just appears, $P_{op}$ immediately drops to a minimum (caused by the split tip dullness of $P_{OL}$) and then it gradually rises to a maximum (maximum value of $R_{YB}$ corresponding to $P_{OL}$) and begins to decline until it reaches the constant amplitude steady $P_{OP}$. At this time the retardation effect disappears. The corresponding variation of $\frac{da}{dN}$ is opposite to that of $P_{op}$. In the figure it also indicates that the $\frac{da}{dN}$ curve calculated based on the improved Maarse model approaches the experimental curve more than that of the original model. Similarly, the retarda-

retardation model based on the closure effect can better describe the five stages [1] of the retardation process and thus are conceptually better from a physics point of view.

The above is a comparison of the prediction of overload retardation effect for the material Ti-6Al-4V under two overload ratio and various crack lengths. As for the application of other materials and complicated spectrum loads, further verification is required.

## V. CONCLUSIONS

1. The plastic zone correction equation proposed in this paper is

$$R_p = \frac{1}{\alpha\pi}\left(\frac{K}{\sigma_{ys}}\right)^2$$

where

$$\alpha = \frac{6}{1+2S}$$

$$S = (\Delta K - \Delta K_{th})/(1-R)K_c$$

The corrected plastic zone equation can more closely reflect the characteristics of fatigue crack propagation and the continuity of stress state transformation. Hence, it is possible to be suitable for the variable stress condition under variable loads.

2. The improved Willenborg model and Maarse model have a wider range of applicability than the original ones. They are convenient to use and the accuracy is signfficantly higher.

## REFERENCES


[1] Gu Mingda, Zhang Yongkui and Yan Minggao. "Investigation of overload retardation effect and overload retardation model of Ti-6Al-4V titanium plate", Aeronautical Materials (special) vol. 2, 1981, pp 27-34.

[2] Schijve, J., "Four Lectures on Fatigue Crack Growth", Eng. Fract. Mech. Vol. 11, 1979, pp. 167~221.

[3] Willenborg, J.D., Engle, R.M. and Wood, H.A., "A Crack Growth Retardation Model Using an Effective stress Concept", AFFDL-TM-FBR-71-1, 1971.

[4] Ho Chinchi. "A new model considering the overload retardation effect", Journal of Beijing Institute of Aeronautics and Astronautics, no. 1, 1980.

[5] Huang Yushen and Liu Shihwei. "Semi-linear Willenborg retardation model", Northwest Industrial University Technical Information, SHJ 8003, 1980, 3.

[6] Chang, J.B., Engle, R.M. and Szamossi, M., "An Improved Methodology for Predicting Random Spectrum Load Interaction Effects on Fatigue Crack Growth", ICF 5, Vol. 5, 1981, pp. 2615~2623.

[7] Trebules, V.W., Jr., Roberts, R., and Hertzberg, R.W., "Effect of Multiple Overload on Fatigue Crack Propagation in 2024-T3 Aluminum Alloy", ASTM STP 536, 1973, pp. 115~146.

[8] "Damage Tolerant Design Handbook", MCIC-HB-01, 5.1-15(12/72).

[9] Schmidt, R.A. and Paris, P.C., "Threshold for Fatigue Crack Propagation and the Effects of Load Ratio and Frequency", ASTM STP536, 1973, pp. 79-94.

[10] Maarse, J., "Crack Closure Related to Fatigue Crack Propagation", Fracture, ICF4, Vol. 2, 1977, pp. 1025~1034.

[11] Bell, P.D. and Creager, M., "Crack Growth Analysis for Arbitray Spectrum Loading", AFFDL-TR-74-129, 1975.

[12] Wanhill, R.J.H., Meulman, A.E. and Van der Vet, W.J., "Fatigue Crack Propagation Data for Titanium Sheet Alloys", Interim Report No. 5, NLR318, 1974.

[13] Gray, T.D. and Gallagher, J.P. "Predicting Fatigue Crack Retardation Following a Single Overload Using a Modified Wheeler Model", ASTM STP 590, 1976, pp. 331-344.

# MODIFICATION OF THE WILLENBORG AND MAARSE MODELS AND APPLICATION TO THE LIFE PREDICTION FOR Ti-6Al-4V ALLOY

*Zhang Yongkui, Gu Mingda and Yan Minggao*

*(Institute of Aeronautical Materials)*

Abstract

The prediction accuracy of the overload retardation effect on fatigue crack growth (FCG) is closely related to the formula for the plastic zone adopted by each retardation model. Hence, in order to express more rationally the behavior of fatigue crack growth process and the continuity of the stress state transformation (from plane strain to plane stress mode), the coefficient $\alpha$ in the formula for the plastic zone used in the Willenborg and Maarse models can be expressed as the following:

$$\alpha = \frac{6}{1+2S}$$

where

$$S = \frac{\Delta K - \Delta K_{th}}{(1-R)K_c}$$

$S$ is the fraction of the stress part in a fracture surface. Meanwhile, it was found that the material constants $C^*$ and $n^*$ in the formula of the Maarse model can be substituted by $C$ and $n$ obtained from the constant amplitude loading tests.

From the above mentioned modification of the Willenborg and Maarse models, it is recognized that the modified models can be applied more successfully and conveniently to the life prediction for Ti-6Al-4V alloy under a single tensile or a series of single tensile overloads. The results calculated with the modified models were found to be fairly consistent with the experimental data.

# STUDY ON THE MEASURING TECHNIQUE OF THIN BOUNDARY LAYERS 112

Nanjing Aeronautical Institute, He Zhongwei

ABSTRACT

This paper introduced a self-designed and fabricated miniature driver with measuring probes for measurement of thin boundary layers. The driver used the Chinese made Hwei model 28BF001 stepmotor as the main design body. It transforms the angular displacement of the motor into linear displacement. The minimum linear velocity is 0.00625 mm per unit pulse. Its working travel is 5.0 mm. It has good static characteristics. The outside diameter is 28 mm and height is 50 mm. The structure is simple. In the paper two types of thin boundary layer probes were introduced.

The results of the use of it in a supersonic flow showed that the driver worked reliably. The probe did not show any vibration and was able to measure thin boundary layer velocity distribution with accuracy.

In the present conditions of the dimensions of supersonic tunnels in our country, it has very practical meaning [1] to design a miniature driver with boundary layer probe to measure thin boundary layers. This paper introduces a self-designed and developed miniature driver and probe.

## I. MINIATURE DRIVER FOR MEASUREMENT OF BOUNDARY LAYERS

The main body of the driver is a domestic model 28BF001 step motor. The electrical step angle is 3°. The maximum static rotation moment is 0.18 kg.cm. The outside diameter is 28 mm, length is 28 mm.

The design principle of the driver is simple. The structure is compact. A precisely machined M 6.5 x 0.75 fine screw-treaded rod made of durable copper material was lightly heat pressed on the electrical shaft. The treaded rod is installed with precisely machined screw-nuts.

When the treaded rod produced an angular displacement along with the electrical shaft due to an external electric pulse signal, the screw nut in the very smooth square groove together with the probe installed on its top was constrained to move up or down. When fabricating the driver, precision machining is required. The threaded rod and the screw nut must be matched so that after installation their friction force and spacing are very small.

Figure 1 represents the 204-2 driver structural schematic diagram. The main data are in the following: Minimum linear velocity is 0.00625 mm per pulse, working travel is 5.0 mm; the static characteristics of the driver are shown in Figure 2. Curves B and C (reproducibility) are static characteristic curves determined by the powerful toolmicroscope. A is the theoretical curve; B and C are very close to A.

The driver is controlled directly using the domestic BQDI-001 driving power source. It is convenient to use. It is possible to make corrections through the use of that driving power source, the movement velocity, direction and position of the probe fixed at the top of the driver can be controlled by frequency variation, fixing direction and fixing phase. 101

Received May 1981.

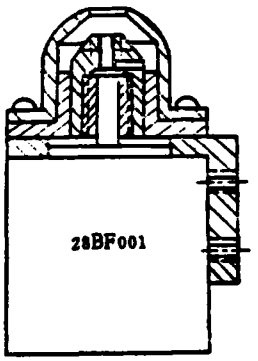


Fig. 1 Schematic of driver 204-2 for measuring the boundary layer

## II. DESIGN OF THIN BOUNDARY LAYER TOTAL PRESSURE PROBE

Through the analysis of the possible displacement of the probe in supersonic flow, we designed a special probe (Figure 3) from actual practical experience. In order to avoid the effect of the probe lever on the measured total pressure valve let us take $L/d \geqslant 10$, and $l/L = \frac{1}{2}$. Beginning with strengthening the stiffness of the probe, the tip of the probe, is made into an arc shape and the probe level is made into a loop structure. The front extending portion of the

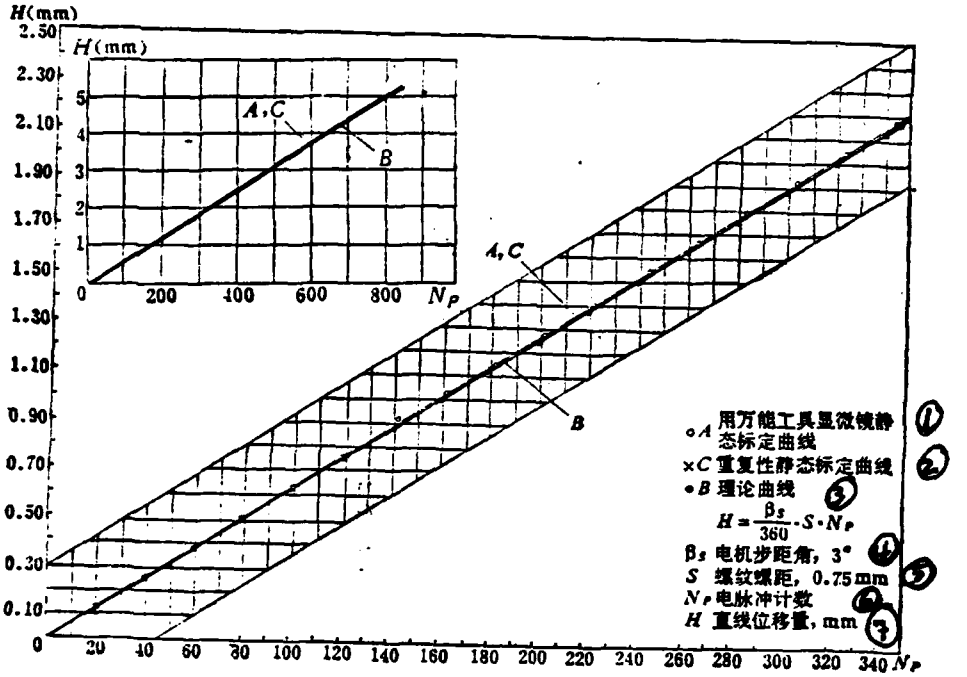


Fig. 2 The static characteristics of driver 204-2

Key: 1--static curve determined using the all purpose microscope; 2--static curve determined by reproducibility; 3--theoretical curve; 4--electrical step angle 3°; 5--spacing of screw thread; 6--electric pulse counter; 7--linear displacement

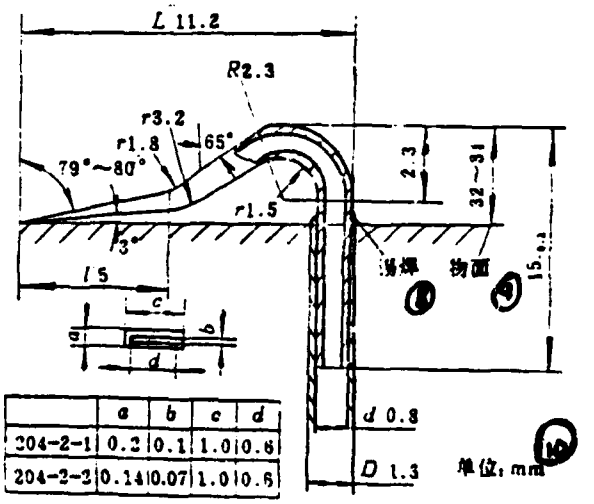


| | a | b | c | d |
|---|---|---|---|---|
| 204-2-1 | 0.2 | 0.1 | 1.0 | 0.6 |
| 204-2-2 | 0.14 | 0.07 | 1.0 | 0.6 |

图3 204-2附面层探针尺寸

Fig. 3 Sizes of the boundary layer probes 204-2

Key: 8--solder; 9--surface; 10--unit

probe is 7-8° sharply split. The inner channel of the probe is an expansion type to facilitate the pressure measurement response speed. In order to ensure that the lower surface of the probe and the surface of the object have a linear contact, the lower surface of the forward extension portion of the probe and the surface of the object maintain a 3° inclination angle. The outside heights of the two types of probes are 0.2 mm and 0.14 mm and the inside heights are 0.1 mm and 0.07 mm. The inside width and outside width at the 1.0 mm opening of the probe are 0.8 mm and 0.6 mm, respectively. The top of the probe was made into shape by directly heating 0.8 mm a stainless steel tube until red hot. The sizes of the probe opening were measured using a standard plug caliper. The external shape of the two probes is the same. The external shape and size were examined optically. The sizes of the opening of the two probes are equivalent to those of the boundary layer probes used internationally [2,3].

## III. APPLICATION EXAMPLES

In the single-support point semi-soft wall nozzle supersonic tunnel at Nanjing Aeronautical Institute, the model 204-2 driver with boundary layer probe was used to measure the boundary layer parameters on the second cone of the intake of a certain airplane. Experimental conditions were: Incoming flow Mach number $M_\infty$=1.97, 2.10 ; downward inclination angle of the nozzle $\alpha=0°$ . The pressure measuring system: SYD-1 transducer and XJ-100 circuit measuring meter equipped with model LS-5 digital recorder.

When the boundary layer of the cone was measured, the driver was installed inside the cone and the probe reached out on the cone surface (Figure 4). During the measurement of boundary, the probe moved gradually from the side out starting from the surface according to a step of 10 pulses per stop. The match between the probe level and the cone body is very important. Five pressure measuring tubes were specially installed inside the cone chamber. The measured results reflected that internal pressure variation in the cone chamber was very slight before and during the experiment. This explains that the boundary layer of

the cone surface did not have a conical inward flow (Figure 4). In addition, right underneath the probe opening, a 0.6 mm diameter static pressure tube was installed on the cone surface. It is electrically isolated from the cone. In the experiment the static pressure tube carried electricity. When the probe and the end surface of the static pressure tube come into contact, an indicator light comes on. The extinguished light was a symbol for the starting of the boundary layer.

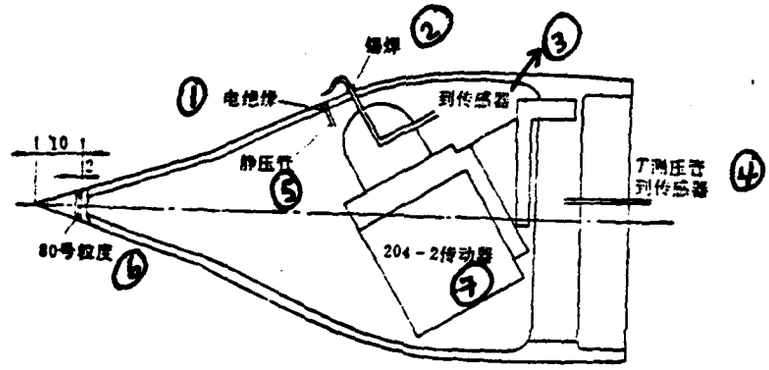


Fig. 4 Position of driver 204-2 with a probe in a bicone.

Key: 1--electric insulation; 2--solder; 3--to transducer; 4--T pressure tube to transducer; 5--static pressure tube; 6--size 80 particle size; 7--204-2 transducer

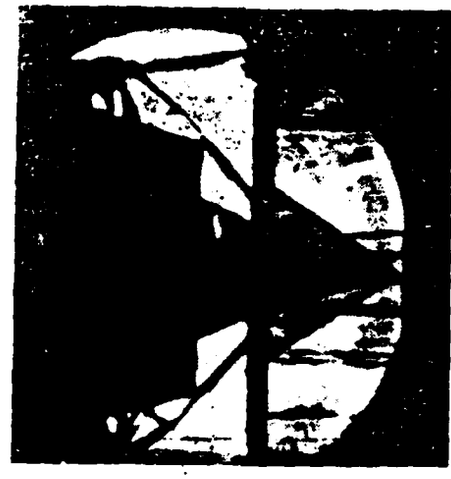

Fig. 5 Schlieren photograph of shock wave pattern on the bicone

Experimental observation showed that the driver and probe could work steadily in supersonic flow. Only during the start-up of the tunnel, because of the instability of the flow, the probe-surface contact indicator light twinkled weakly. However, after the start-up of the tunnel, the indicator light stayed on constantly. In the experiment observation was made especially with respect to the motion of the probe. On the frame of the observation window of the tunnel, a 0.25 mm diameter steel wire was fixed in the transverse direction and the probe opening was placed close to the image of the steel wire. Then, the tunnel was started and after repeated observations, the probe was not found to move relative to the steel wire in stable supersonic flows. No probe vibration was found either.

Schlieren photograph of the probe and shock wave pattern on the bicone under the super critical condition at the intake at $M_\infty=2.10$, $\alpha=0°$ is shown in Figure 5.

Figure 6 shows the boundary layer velocity distribution of the second conical surface of the center cone at the station 60 mm from the conical tip. The boundary layer velocity distribution of the same cross-section measured by 204-2-1 and 204-2-2 probes are shown in the figure. In the figure y represents the perpendicular distance from the probe center to the surface; $\delta$--thickness of the boundary layer; u--local flow speed at the boundary layer; $U_\infty$--boundary layer interface flow velocity; N--exponent. 103

In comparison of velocity distribution, the probe was placed as far away from the surface as possible not affecting the static pressure underneath. This value was used to represent the static pressure of the entire cross-section. As for speed in the boundary layer above the sonic speed, a correction must be made based on positive shock wave loss in order to obtain the actual speed of the wave front.

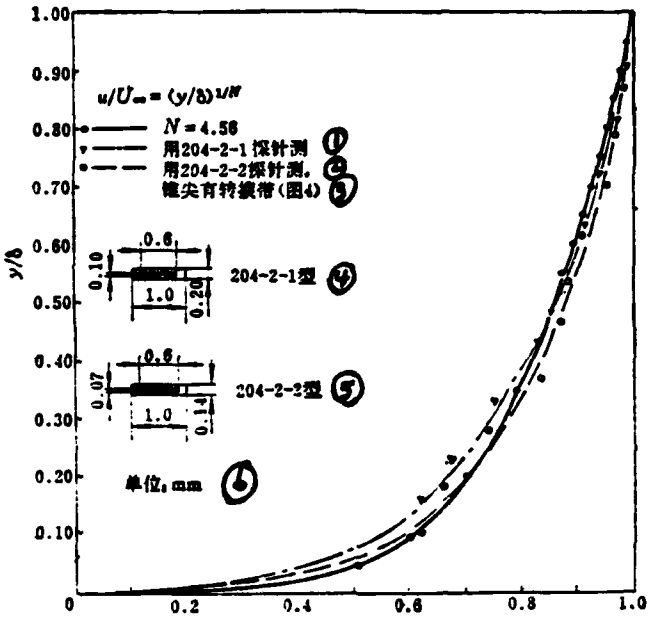


Fig. 6 Boundary layer profiles on the second conical surface at the station 60 mm from the conical tip

Key: 1--use 204-2-1 probe; 2--use 2-4-2-2 probe; 3--conical tip has turning band (Figure 4); 4--204-2-1 type; 5--204-2-2 type; 6--unit: mm

## CONCLUSIONS

Under the condition $M_\infty = 2.10, 1.97$ and $\alpha = 0^\circ$, for a 1:10 scale intake second conical surface of a certain airplane, experimental results of boundary layer verified:

1. Model 204-2 driver can completely satisfy the requirements of measuring thin boundary layer. The minimum linear velocity of the driver is 0.00625 mm per pulse; working travel is 5.0 mm. It has good static characteristics. The experimental and theoretical values are very close. It works reliably and its structure is simple. Its successful miniaturization has provided a very important means in the small scale boundary layer control study.

2. 204-2 type boundary layer probe size is equivalent to that used internally. The probe has excellent rigidity. It shows no vibration in high speed flow. The probe can work steadily.

After more than half a year of actual use, it is verified that the mentioned driver and probe for measurement of boundary layer can completely satisfy the requirements in measuring thin boundary layers.

REFERENCES

[1] He Zhongwei. "Present status of supersonic intake boundary layer control research in other countries". Nanjing Aeronautical Institute Technical Information no. 670, 1979, 12. 105

[2] Michael K. Fukuda. Warren G. Hingst, Control of Shock Wave-Boundary Layer Interaction by Bleed in supersonic Mixed Compression Inlet. NASA CR-2595 1975.

[3] Gary S. Settles, Irwin E. Vas, and Seymour M. Bogdonoff, Details of a Shock-Separated Turbulent Boundary Layer at a Compression Corner. AIAA Journal, Vol. 14, NO. 12. December 1976.

# STUDY ON THE MEASURING TECHNIQUE OF THIN BOUNDARY LAYERS

*He Zhongwei*

*(Nanjing Aeronautical Institute)*

Abstract

A type of miniature driver with measuring probe 204-2 designed by ourselves for measurement of thin boundary layers is described. In the design the homemade miniature stepmotor 28BF001 serves as a main body. The driver is simple in construction (see Fig. 1) and reliable in operation. It transforms the angular displacement of the motor into linear displacement. Its minimum linear velocity is 0.00625mm per unit pulse, and its working travel is 5.0mm. The driver with an outside diameter of 28mm and height of 50mm has good static characteristics (Fig. 2). It is found that the experimental curve A, C extremely coincides with the theoretical curve B.

Two types of measuring probes 204-2 are also presented in this paper. The outer height is 0.2mm and inner height 0.1mm for one probe tip, while for another they are 0.14mm and 0.07mm respectively. Both tips possess the same outer width of 1.0mm and the inner one of 0.6mm. The configurations of both probes are the same (see Fig. 3).

The driver and the probes presented above have already been used for measuring the boundary layer parameters on the second cone of a supersonic intake working in supercritical conditions (Figs 4 and 5). The experiments were carried out in our supersonic intake tunnel with free-stream Mach numbers 1.97 and 2.10. The boundary layer profiles were shown in Fig. 6.

By observing the movement of the probes during the experiments, it was proved that the driver and probes worked steadily in a supersonic flow without vibration, and the thin boundary layer profiles measured were quite correct.

# MICROMECHANICAL ANALYSIS OF CREEP CRACK GROWTH ON A NICKEL BASED SUPERALLOY

Beijing Iron and Steel Research Institute
Shen Huiwang, Gao Zhentao, Liu Changfu and Cai Qigung

## ABSTRACT

The stress rupture life test of smooth and precracked superalloy specimens shows that a small pre-existing crack can seriously reduce the stress rupture strength and life of superalloy components.

Scanning electron microscopy and metallographic analyses indicate that the crack propagates along grain boundaries by cavitation. Based on micromechanical analysis of the cavity growth and coalescence with the main crack tip, creep crack propagation equations were derived based on creep J integral parameter $\dot{J}$ and crack opening displacement (COD) rate $\dot{\delta}$. Experimental data of $GH_{33A}$ superalloy proved the above fracture mechanical analysis.

## I. INTRODUCTION

The crack formation and propagation analyses on the bottom of the outer wheel of the turbine or at the root of the groove, or in the blade are complicated because of hot corrosion and the interaction between strain fatigue and creep. The high temperature zone of the engine sometimes has (or through hot corrosion forms) small cracks. Under the high temperature creep conditions these small cracks interact with the grain boundary cavities which causes these pre-existing small cracks to rapidly propagate.

In the past, long crack specimens were used in creep crack growth experiments which were limited to certain creep conditions. However, in high temperature components, most of the cracks formed by welding and hot corrosion have much smaller dimensions than that of the cross-section of the components. In addition, periodic check-up and maintenance also would not allow the crack to grow too long. From the view-

point of design life and fracture control, it is necessary to carry out experimental analysis on the rupture life and crack propagation using superalloy specimens with pre-existing small cracks under total creep yield conditions. This paper is based on this consideration. A study on the creep crack propagation of superalloy was performed by understanding the mechanisms of grain boundary cavity formation, growth and coalescence due to creep strain during each flight cycle of the engine turbine.

## II. EXPERIMENTAL METHOD AND MATERIAL

The superalloy ($GH_{33A}$) used in the experiment was melted in a three-ton electric furnace and then fabricated into material. The major chemical components of the alloy are Ni–20%Cr–2.5%Ti–0.7%Al–1.5%Nb. The heat treatment schedule is 1080°Cx8 hours solid solution, 750°C x16 hours. The constant temperature mechanical characteristics are: $\sigma_B$ = 1226, $\sigma_{0.2}$ = 814, $\delta$ = 31%, $\psi$ = 35%.

Received January 1981.



The specimens used in the creep test were cylindrical and plate specimens. The dimensions of cylindrical specimens are $\phi$22x100 (mm), and $\phi$10x100 (mm) and the plate specimen sizes are 3x20x60 (mm) and 3x25x60 (mm).

For the 10 mm diameter cylindrical specimen and plate specimens, the cracks were pre-fabricated at ambient temperature and then creep fracture experiments were carried out at high temperature.

The fractured surface was examined using the British made SEM-$S_4$-10 for observation.

## III. ANALYSIS OF EXPERIMENTAL RESULTS AND DISCUSSION

From the stress rupture life experiment results obtained for smooth and pre-fabricated cracked specimens of superalloy as shown in

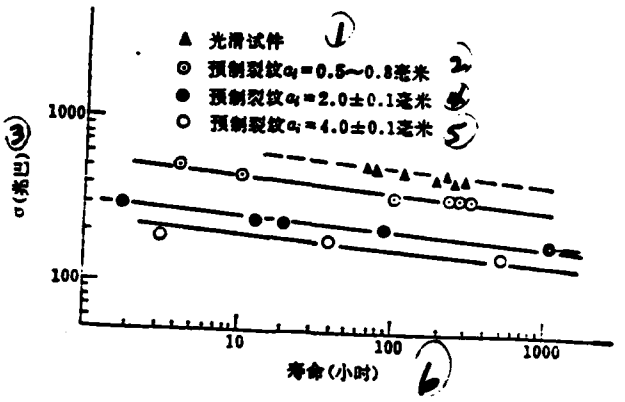


Fig. 1 Stress rupture life of smooth and precracked superalloy specimens at 700℃

Key: 1--smooth specimen; 2--prefabricated crack, (mm); 3--(MPa) 4--prefabricated crack, (mm); 5--prefabricated crack, (mm); 6--life (hrs)

Figure 1, it is seen that pre-existing cracks can seriously decrease the stress endurance life and strength.

Metallographic analyses of the fractured surface and measured surface indicated that the crack propagated along the grain boundary (Figure 2). Concentrated spots were located on the fractured surface along the grain boundary (Figure 2(a) which showed the crack propagation was realized through the growth of the grain boundary cavities and the coalescence with the main crack. Therefore, it is necessary to establish the law of creep crack propagation along the grain boundary based on the microplastic mechanical analysis of grain boundary cavitation growth and coalescence with the main crack under the strain field caused by the creep stress in front of the crack. In this paper, the crack opening displacement rate and creep J integral parameter J are used to replace stress intensity factor K. Because under high temperature and high stress conditions, in the total creep yield region of existing small cracks, the creep rate is high which quickly relaxes the elastic stress field, hence the crack tip field is controlled by power multiplication of the equation of creep regularity. For material with a power multiplication creep regularity ($\dot{\varepsilon} = \alpha\sigma^n$), the equations of mechanics and the solutions are completely similar to those of pure power solid material [2] (where $\dot{\varepsilon}$ is creep rate; n is creep exponent; $\alpha$ is a material constant related to temperature; a is stress). For a

spherical hole with an instantaneous radius R in an infinitely large creeping material, its radial displacement rate $\dot{R}$ can be expressed as

$$\frac{\dot{R}}{R}=\alpha\sigma^{n}\tilde{R}(n) \qquad (1)$$

where $\tilde{R}(n)$ is a parameter related to the rigidity of the material. For a pure rigid material, equation (1) can be obtained using the similarity analysis method according to the literature [2]. Let us assume that the rate of creep cavitation growth in the crack tip region can be approximated by the cavitation creep growth rate described above. It is worthwhile noticing that only when the cavity is very small relative to the space where the cavity exists that the above assumption is correct. Because the cavity growth life is mainly spent in the initial growth period when the cavity is still small, this approximation is reasonable. Then we get:

$$\frac{\dot{R}(x)}{R(x)}=\alpha[\sigma(x)]^{n}\tilde{R}(n)=\dot{\varepsilon}(x)f(n) \qquad (2)$$

where $\sigma(x)$ and $\dot{\varepsilon}(x)$ can be any arbitrary stress and strain rate components at the tip of the crack.

Under steady crack propagation conditions, it is possible to calculate the crack growth rate by considering that the crack tip moves toward the cavity or the cavity moves toward the crack tip. If $\lambda$ is the average ditance between cavities, under the condition that steady state propagation rate is $\dot{a}=\frac{da}{dt}$, in the process that the cavity approaches the crack tip at $x=\frac{\lambda}{2}$ from the distance $x=x_0$, the radius of the cavity grows from the critical radius $R_0$ to the final radius $R_f=\frac{\lambda}{2}$ to coalesce with the crack tip which ensures the steady state propagation of cracks. When considering the cavity growth at a fixed point, there should be a + x = constant. Therefore, $\dot{a}=\frac{da}{dt}=-\frac{dx}{dt}$, By considering $dR(x)=\dot{R}(x)dt=-\dot{R}(x)\frac{dx}{\dot{a}}$, and substituting into equation (2), we get

$$\int_{R_0}^{\frac{\lambda}{2}}\frac{dR(x)}{R(x)}=\int_{x_0}^{\frac{\lambda}{2}}f(n)\dot{\varepsilon}(x)\left(-\frac{dx}{\dot{a}}\right) \qquad (3)$$

and

$$\dot{a}=\frac{da}{dt}=\frac{f(n)}{\ln\frac{\lambda}{2R_0}}\int_{\frac{\lambda}{2}}^{x_0}\dot{\varepsilon}(x)dx$$

where $x_0$ is the dimension of the effect stress field region at the crack tip which is the inception nucleus of the cavity, and a coordinate increases at significant rates and is used as the cut-off distance and

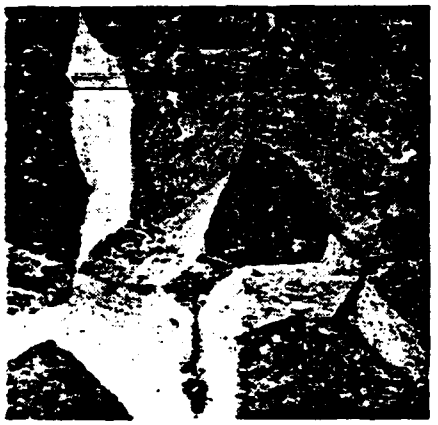

(a)

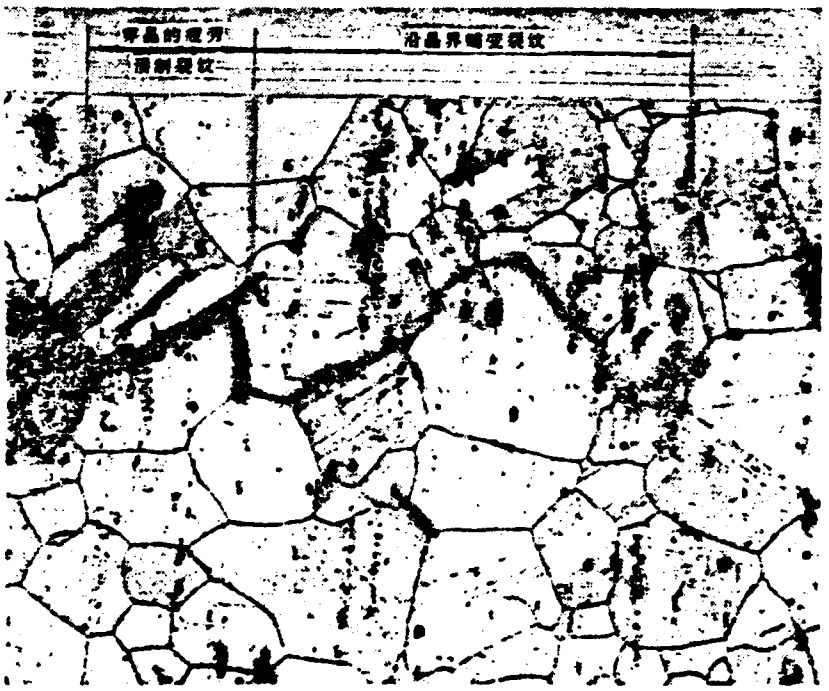

(b)

Fig. 2 Creep crack growth along grain boundaries
(a) SEM micrograph of fracture surfaces magnification ×500;
(b) Metallograph micrograph magnification ×200.

lower limit of the integrals of the right hand side of the above equation. Therefore, for materials following power product creep law, it is possible to obtain from the analytical method in [2] that:

$$\dot{\varepsilon}(x)=\left(\frac{\dot{\delta}}{a}\right)\varphi\left(\frac{x}{a},\ n\right) \tag{4}$$

where $\dot{\varepsilon}(x)$ is the arbitrary strain component at x. Substitute into equation (3) to obtian the crack propagation law described by the crack opening displacement rate parameter $\dot{\delta}$:

$$\frac{da}{dt}=B\dot{\delta} \tag{5}$$

$$B=\left(f(n)/\ln\frac{\lambda}{2R_0}\right)\int_{\frac{\lambda}{2a}}^{\frac{x_0}{a}}\varphi\left(\frac{x}{a},\ n\right)d\left(\frac{x}{a}\right),$$

can be experimentally determined by creep fracture experiments.

Using the singularity relation $\dot{\varepsilon}(x)=\alpha\left(\frac{j}{\alpha\ln x}\right)^{\frac{n}{n+1}}\tilde{\varepsilon}(0,n)^{(\theta=0)}$ (where $\tilde{\varepsilon}(0,n)$ ) is the angular factor parameter of $\tilde{\varepsilon}(\theta,n)\theta=0)$, the crack propagation law described by the creep J integral parameter $\dot{J}$ can also be obtained by substituting it into equation (3).

$$\frac{da}{dt}=Cj^{\frac{n}{n+1}} \tag{6}$$

where $C=\left(f(n)/\ln\frac{\lambda}{2R_0}\right)\int_{\frac{\lambda}{2}}^{x_0}\alpha\left(\frac{j}{\alpha\ln x}\right)^{\frac{n}{n+1}}\tilde{\varepsilon}(0,n)dx$

This relation agrees with a large amount of experimental data provided in [6].

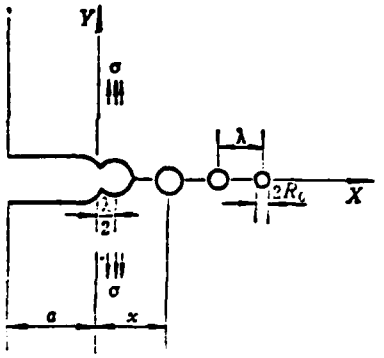


Fig. 3 Growth of cavities formed along grain boundaries under crack tip creep stress strain field and their coalescence with the main crack tip

Shih and Hutchinson [7] gave the finite element results of power product law creep material plane stress crack tensile plate $\dot{\delta}$:

$$\dot{\delta}=\alpha g_2\left(\frac{a}{b},\ n\right)a\left(\frac{b\sigma}{b-a}\right)^n \tag{7}$$

where b is the width of the plate. Substituting equation (7) into (5), we get

$$\frac{da}{dt}=Da\left(\frac{b\sigma}{b-a}\right)^n \tag{8}$$

$D=\alpha B g_2\left(\frac{a}{b},\ n\right)$, which can be treated as a constant in engineering applications. Equation (8) begins to integrate from the initial crack depth $a_j$ to the final depth $a_f$ to obtain

$$\int_{a_i}^{a_f}\frac{1}{a}\left(1-\frac{a}{b}\right)^n da=D\sigma^n t \qquad (9)$$

At 700°C, it has been determined that the creep exponent n = 10 and creep crack propagation coefficient D = $0.70\times10^{-26}$ for superalloy crack tensile plate. The corresponding experimental results are shown in Figure 1. The two solid lines on the very bottom were curves obtained from the numerical integration of equation (9) by using n = 10, D = $0.70\times10^{-26}$, $a_i$ = 2 mm, $a_i$ = 4 mm and $a_f$ = 10 mm. The points in the figure are the actual points of measurement which completely coincide with the calculated values. Although the above are experimental results obtained from thin plates under creep conditions, it is possible to extend to the crack growth law of small cracks under total creep yield thin plates. When $\frac{a}{b}\to 0$, the integral gives the result $a=a_i\exp[0.70\times10^{-26}\sigma^{10}t]$. However, for the small surface cracks frequently encountered in engine components, these cracks are not located in the plane stress and durable band creep regions but primarily in the plane strain and total creep region. Hence, a stress rupture experiment (Figure 1) was performed on a cylindrical tensile sample with prefabricated surface crack at a depth of 0.5-0.8 mm under plane strain conditions. Under tough zone creep conditions, due to the complexity of geometry involved with the cylindrical specimen under force, the analysis of life and propagation rate of the surface crack becomes relatively more difficult. Therefore, it is necessary to limit the experiment under total creep conditions. It is to say that an interrupted stress endurance test was performed using tensile rod with pre-existing cracks at 0.5-0.8 mm depth to make the final crack depth $a_f$ not exceed 2.5 mm. Therefore, under total creep conditions $\dot{\delta}=2\pi Q a(\alpha\sigma^n)$ obtained from [2] can be plugged into equation (5) and after integration we get

$$D\sigma^n t=\ln\frac{a_f}{a_i} \qquad (10)$$

where $D=2\pi Q\alpha B$ ; Q--crack shape factor

At 700°C, under plane strain conditions, the creep exponent of the superalloy was experimentally determined to be n = 10. Under total creep yield conditions, the same result as equation (10) was obtained by substituting $j=2\pi Q^2 a\int \sigma d\dot{\varepsilon}^{(2)}$ into equation (6) where $D=C\left[2\pi Q^2 a\frac{n}{n+1}\right]^{\frac{n}{n+1}}$. The photograph in Figure 2(b) is a sideview of a metallographic crack from the interrupted stress experiment. The cutting depth is 0.72 mm. The fatigue crack depth across the grain is 0.1 mm measured from the picture. The initial crack depth $a_i$ = 0.82 mm. The creep crack along the grain boundary in the photograph is 0.4 mm. Therefore, $a_f$ = 1.22 mm. The experimental stress $\sigma$ = 373 MPa and period t = 153 hours. Putting the data into the equations, the creep crack propagation coefficient under plane strain conditions was calculated to be $D=\ln\frac{1.22}{0.82}/373^{10}\times 153=0.50\times 10^{-28}$. Consequently, the crack propagation formula, $a=a_i\exp(0.50\times 10^{-28}\sigma^{10}t)$ is obtained under plane strain and total creep conditions. It is worthwhile noticing that the crack propagation rate in this paper is two orders of magnitude lower under plane strain conditions than that of plane stress conditions. SEM analysis of fractured surface showed that the cavity size and spacing in the middle region under plane strain are much smaller than those of plane stress specimens (Figure 4). This explains that the cavity propagation rate and creep rate at the crack tip are lower under plane strain conditions. Therefore, before the coalescence of cavities more cavitation nuclei were formed. Experimental results showed that under plane strain and total creep conditions small surface cracks are not the same as those penetrating cracks of thin plates under plane stress and durable band creep conditions. Hence, in order to more precisely predict the life and crack propagation rate of engine components with pre-existing surface cracks, it is necessary to carry out stress endurance life and crack propagation rate analysis and test using specimens with pre-existing small surface cracks under plane strain and total creep conditions.

## IV CONCLUSIONS

Pre-existing small cracks in superalloy components can seriously decrease stress rupture life and strength.

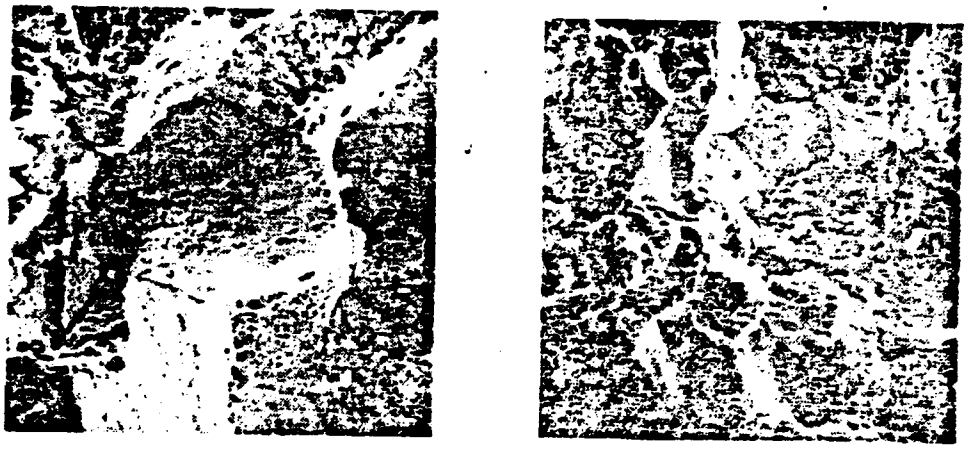

(a) (b)

Fig. 4 Cavities formed along grain boundaries at 700°C SEM micrographs of fracture surfaces ×500
(a) Plane strain; (b) Plane stress.

On the basis of micromechanical analysis, using crack opening displacement rate and creep J integral to evaluate, fracture mechanical analysis has been performed for power product creep material crack tensile specimens. It was discovered that the creep propagation rate is two orders of magnitude lower in plane strain conditions than that in plane stress conditions.

REFERENCES


[1] W.D. Nix, D.K. Matlock and R.J. Dimelfi, Acta Metallurgica Vol25, NO5 1977.P495.
[2] Cai Qigung. Metallurgical Journal vol. 13, no. 4, 1977.
[3] J.R. Rice, G.F. Rosengren《J. Mech. Phys. Sol.》16(1968)1-12.
[4] J.W. Hutchinson《J. Mech. Phys. Sol.》16(1968)13-21.
[5] J R. Rice《Fracture》Vol I. H. Liebowiz Ed. A Cademic pr (1968)191-311.
[6] K.M. Nikbin, G.A. Webster and C.E. Turner Fracture ICF4 Vol2A 1977 p627.
[7] C.F. Shih, J.W. Hutchinson, Journal of Engineering Materials and Technology Vol 98 1976. p289.

# MICROMECHANICAL ANALYSIS OF CREEP CRACK GROWTH ON A NICKEL-BASE SUPERALLOY

*Shen Huiwang, Gao Zhentao, Liu Changfu, Cai Qigung*

*(Central Iron and Steel Research Institute)*

Abstract

Experiment on stress rupture life of smooth and precracked superalloy specimens shows that small preexisting crack seriously reduces the stress rupture strength and life of superalloy components.

SEM and metallographic analysis indicate that the crack grows along grain boundaries by cavitation. Based on micromechanical analysis of the cavity growth and coalescence with the main crack tip, creep crack growth formulas were derived by using creep $J$ integral parameter $\dot{J}$ and COD rate parameter $\dot{\delta}$. Experimental data on $GH_{33A}$ superalloy have verified the above fracture mechanical analysis.

## THE "VIBRATION THEORY AND APPLIED SCIENCE CONFERENCE"

Jointly held by China Aeronautical and Astronautical Society and China Mechanics Society

The China Aeronautical and Astronautical Society and the China Mechanics Society held the "Vibration Theory and Applied Science Conference" on December 10-16, 1981 in Quinming. The formal representatives and the attending representatives were 168 in total. They came from 20 provinces and cities and 81 organizations. There were 115 papers presented. The meeting reviewed the research results of vibration theory and its application in our country.

Some of the experts attending the meeting gave technical reports. As examples, papers such as "Coupled mechanical problems of fluid and structures" by Professor Tu Ching hua, "Identification of time-space parameters and on-board reduction methods" by Professor Huang Wenhu, "Application of vibration theory in mechanical fields" by Professor Chu Weitu and "Structural mechanics of space craft" by Professor Hu Haichan, etc., benefited the audience.

The conference was divided into four topics of exchange information; viz., simulation combination and characteristics, parametric identification and measurement technique, aerodynamic elastic on-board vibration and its effect; and rotor dynamics, vibration reduction and isolation, etc. After the exchange, all the representatives believed that vibration theory has accomplished some results in the application to engineering problems in our country during recent years. By absorbing new theories, new technologies and new results, this science has been developed and experimental techniques and measuring equipment have been improved significantly. In the conference the 22nd Meeting of Structural Mechanics and Materials in the US was introduced. Furthermore, the 9th International and 1st and 2nd National Non-linear Vibration Meetings were also introduced. Hence, the status of vibrational study in and out of the country was further discussed.

After exchanging ideas, the direction of future research was explored. It was proposed that the trend of development should be carefully noticed. The studies on flow-solid interaction, active control technology and time-space method in conjunction with theoretical study, engineering applications and experimental techniques should be further strengthened concurrently.

During the conference, the China Aeronautical and Astronautical Society and the China Mechanical Society held meetings to discuss the formation of vibration special groups and the content of future academic activities, respectively.

The next national vibration theory will also be held jointly by the two societies, tentatively in 1984.

END

FILMED

2-83

DTIC